



# DEPARTMENT OF PHYSICS

UNIVERSITY OF CAPE TOWN

IYUNIVESITHI YASEKAPA • UNIVERSITEIT VAN KAAPSTAD

Search for  $tWZ$  production in the Full Run 2 ATLAS  
dataset using events with four leptons

Jake Reich

Student Number: RCHJAK001

Supervisor: Dr. James Keaveney

Co-Supervisor: Dr. Sahal Yacoob

A thesis submitted in fulfilment  
of the requirements for the degree of  
Master in Science

August 2021

# Abstract

The search for  $tWZ$  production using  $139 \text{ fb}^{-1}$  of  $pp$  collision data at a centre-of-mass energy of  $\sqrt{s} = 13 \text{ TeV}$ , recorded by the ATLAS experiment at CERN, is presented. Events containing exactly four electrons or muons (tetralepton) are selected with additional criteria based on the number of jets, the number of  $b$ -tagged jets, and the number of  $Z$  boson candidates are used to define signal and control regions. The large  $t\bar{t}Z$  and  $ZZ$  backgrounds are distinguished from signal by a BDT-based algorithm. Inputs to the BDT-based algorithm include, a kinematic reconstruction algorithm which reconstructs leptonically decaying top quarks and a BDT-based algorithm which aims to classify  $\ell b$  systems originating from top quarks. The expected signal strength is extracted via a blinded maximum-likelihood fit to multiple signal and control regions. The measured signal strength is  $\mu(tWZ) = 1.91^{+0.95}_{-0.82}$ , leading to an expected significance of  $1.44\sigma$ . An expected upper limit on the signal strength is set and is given by  $\mu_{up}^{exp} = 1.61^{+2.35}_{-1.16}$ . Furthermore, a combined blinded maximum-likelihood fit was performed across the tetralepton and trilepton (studied in an independent analysis) channels, to further increase the sensitivity of  $\sigma(tWZ)$ . The measured signal strength is  $\mu(tWZ) = 1.80^{+0.70}_{-0.65}$ , leading to an expected significance of  $1.61\sigma$ . An expected upper limit on the signal strength is set and is given by  $\mu_{up}^{exp} = 1.43^{+2.04}_{-1.03}$ .

# Declaration

*17 I certify that this assignment/report is my own work, based on my personal study and/or research and that I have  
18 acknowledged all material and sources used in its preparation, whether they be books, articles, reports, lecture notes,  
19 and any other kind of document, electronic or personal communication. I also certify that this assignment/report  
20 has not previously been submitted for assessment in any other unit, except where specific permission has been granted  
21 from all unit coordinators involved, or at any other time in this unit, and that I have not copied in part or whole  
22 or otherwise plagiarised the work of other students and/or persons.*

# Acknowledgements

24

# Contents

25	<b>1 Introduction</b>	7
26	<b>2 Theory</b>	8
27	2.1 Standard Model of Particle Physics . . . . .	8
28	2.1.1 The Top Quark . . . . .	9
29	2.2 $tWZ$ . . . . .	11
30	2.2.1 Tetralepton Channel . . . . .	11
31	2.2.2 Comparison to Trilepton Channel . . . . .	12
32	<b>3 The ATLAS Experiment and Detector</b>	14
33	3.1 The ATLAS Experiment . . . . .	14
34	3.1.1 Large Hadron Collider (LHC) . . . . .	14
35	3.2 The ATLAS Detector . . . . .	15
36	3.2.1 Coordinate System and Kinematics . . . . .	16
37	3.2.2 Inner Detector . . . . .	16
38	3.2.3 Electromagnetic and Hadronic Calorimeters . . . . .	17
39	3.2.4 Muon Spectrometer . . . . .	17
40	3.2.5 Trigger and Data Acquisition System . . . . .	17
41	3.2.6 Particle Identification and Object Reconstruction . . . . .	17
42	<b>4 Analysis Setup and Strategy</b>	20
43	4.1 Data and Monte Carlo Simulation . . . . .	20
44	4.1.1 Data Samples . . . . .	20
45	4.1.2 Monte Carlo Samples . . . . .	20
46	4.2 Objects . . . . .	21
47	4.2.1 Leptons . . . . .	22
48	4.2.2 Jets . . . . .	22
49	4.2.3 $b$ -tagging . . . . .	23
50	4.2.4 Overlap Removal Procedure . . . . .	23
51	4.3 Kinematic cuts . . . . .	23
52	4.4 Regions and Event Selection . . . . .	23
53	4.4.1 Optimization studies for event selection . . . . .	25
54	4.5 Signal and Control Regions . . . . .	26
55	4.5.1 $tWZ$ OF SR . . . . .	28
56	4.5.2 $tWZ$ SF SR . . . . .	28
57	4.5.3 $t\bar{t}Z$ CR . . . . .	29
58	4.5.4 $Z Z b$ CR . . . . .	29
59	4.5.5 $(tWZ)_{\text{fake}}$ CR . . . . .	40
60	4.6 Fake Lepton Estimation . . . . .	40
61	4.7 Machine Learning Techniques . . . . .	45
62	4.7.1 Object-level BDT . . . . .	45
63	4.7.2 Event-level BDT . . . . .	51
64	4.8 Two Neutrino Scanning Method ( $2\nu\text{SM}$ ) Algorithm . . . . .	57
65	4.8.1 The algorithm . . . . .	57
66	4.8.2 Calculating $w_{2\nu\text{SM}}$ . . . . .	58

67	4.8.3 Kinematic Veto . . . . .	59
68	4.9 Systematics . . . . .	62
69	4.9.1 Experimental uncertainties . . . . .	62
70	4.9.2 Theoretical uncertainties . . . . .	63
71	4.9.3 Generic shape systematics . . . . .	64
72	4.10 Analysis Pipeline and TRexFitter . . . . .	65
73	4.10.1 Fitting Procedure . . . . .	65
74	4.11 Results . . . . .	66
75	4.11.1 Tetralepton Channel . . . . .	66
76	4.11.2 Trilepton and Tetralepton Channels . . . . .	69
77	<b>5 Conclusion</b>	<b>75</b>

78

# Chapter 1

79

## Introduction

80 The production of a single top quark in association with a  $W^\pm$  and  $Z$  boson ( $tWZ$ ) at the CERN LHC is sensitive  
 81 to both the neutral and charged electroweak couplings of the top quark as the process involves the simultaneous  
 82 production of a  $W$  boson and a  $Z$  boson in association with the top quark. Due to the very large coupling of the top  
 83 quark to the Higgs boson, the electroweak couplings of the top quark are a theoretically well-motivated area in which  
 84 to search for the first signs of new physics [**TopQuarkCouplings-searchNewPhysics, top-a-tool-for-disc**] that  
 85 could offer a resolution to the Hierarchy Problem [**Burdman·2015**, 54]. The recent lack of signs of new physics  
 86 from LHC data tells us that new physics is either very heavy, or is very weakly coupled to Standard Model particles,  
 87 therefore signs of new physics might only be observed in anomalous rates of well-chosen processes. A prime example  
 88 of such a process is  $tWZ$ . This has an extremely low production cross section ( $\approx 160$  fb for  $\sqrt{s} = 13$  TeV [25]),  
 89 meaning that it is an extremely rare process to observe and subsequently, it has never been observed by any particle  
 90 physics experiment.

91

92 The latest datasets recorded by the ATLAS experiment at the CERN LHC are sufficiently large to allow a potential  
 93 observation of  $tWZ$  production. In this analysis, the Full Run 2 dataset recorded by ATLAS is used to search for  $tWZ$  production in the tetralepton channel ( $tWZ$  with exactly four final state leptons). A kinematic  
 94 reconstruction technique is used which aims to discriminate between  $tWZ$  and our most prominent background  
 95 process,  $t\bar{t}Z$ . In addition to this, Machine Learning techniques are implemented to further isolate our  $tWZ$  signal.  
 96 Backgrounds from Standard Model (SM) processes including those in which one or more leptons originate from the  
 97 semileptonic decay of a heavy hadron or a photon conversion are estimated by fitting predictions from simulation to  
 98 data in dedicated control regions. As this work forms the basis of an official ATLAS analysis, only blinded results  
 99 are shown. A maximum likelihood fit is performed over our two  $tWZ$  signal regions and three control regions, to  
 100 measure the cross section of  $tWZ$  in the tetralepton channel. In this thesis only the tetralepton channel is explored,  
 101 however, the results of a combined fit that includes an entirely independent analysis of the trilepton channel is  
 102 presented with no overlap of events between the regions defined for these channels.

104

# Chapter 2

105

## Theory

### 2.1 Standard Model of Particle Physics

107 The SM is a model based on Quantum Field Theory (QFT) which classifies all known elementary particles and  
 108 describes their interactions. It is a well-tested model and has shown to be hugely successful in describing experi-  
 109 mental data to great precision [**ALTARELLI 1998**, 8]. For example, in the top quark sector, the  $t\bar{t}$  cross section  
 110 predictions have been confirmed to 3.9% accuracy [**cms-ttbar**, **ATLAS-CONF-2019-041**]. It incorporates three  
 111 of the four fundamental forces of nature: the electromagnetic, the weak and the strong forces. In Figure 2.1, all  
 112 known elementary particles described by the SM, are shown.

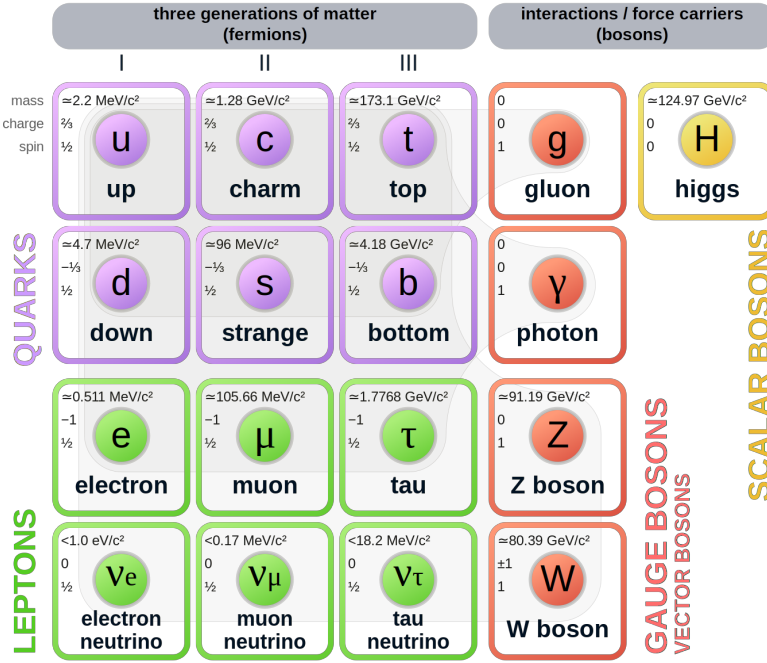


Figure 2.1: A summary of the elementary particles described by the SM [64] is shown. Fermions are shown on the left, with quarks shown in purple and leptons shown in green. Bosons are shown on the right, with gauge bosons shown in red and the Higgs boson shown in yellow. The mass, electric charge and spin of each particle is shown on the top left of each particle's block.

113 Particles in the SM are uniquely described by their quantum numbers: electric charge and spin. The SM particles  
 114 are split into main two classes, based off their spin quantum numbers. Particles which have half-integer spin are  
 115 called fermions, and those which have integer spin are called bosons. Fermions are further divided into three genera-  
 116 tions, each comprising of two quarks, one charged lepton and one neutrino. In a generation, the more massive quark  
 117 has an electric charge of  $+2/3$  (up-type) and the less massive quark has an electric charge of  $-1/3$  (down-type). All

118 charged leptons have an electric charge of  $-1$  and all neutrinos are electrically neutral. The masses of the particles  
 119 in a generation increase with increasing generation number, with generation 1 particles being the least massive and  
 120 generation 3 particles being the most massive. Quarks carry electric and colour charge, and can therefore interact  
 121 via the electromagnetic, weak and strong forces. Colour charge can take on three values: red, green and blue.  
 122 It is important to note that colour charge is completely unrelated to the everyday meaning of colour, and it just  
 123 represents the quantum state of the particle. Due to colour confinement [82], quarks cannot be isolated from one  
 124 another. They exist in colourless bound states, called hadrons, consisting of two or more quarks. Hadrons consisting  
 125 of an even number of quarks are known as mesons and those consisting of an odd number of quarks are known as  
 126 baryons. On the other hand, charged leptons (electron ( $e$ ), muon ( $\mu$ ) and tau ( $\tau$ )) only carry electric charge and  
 127 can therefore interact electromagnetically and weakly, but not through the strong interaction. The electric and  
 128 colour neutral fermions, neutrinos, can only interact via the weak force.

129  
 130 Particles are able to interact with one-another via the exchange of a gauge boson (boson with spin-1). Photons  
 131 are massless, spin-1 gauge bosons which mediate electromagnetic interactions between particles which carry electric  
 132 charge, such as quarks and charged leptons ( $e$ ,  $\mu$  and  $\tau$ ). The weak interaction is mediated by three massive gauge  
 133 bosons, the electrically charged  $W^+$  and  $W^-$  bosons and the electrically neutral  $Z$  boson. Gluons are massless,  
 134 spin-1 gauge bosons which mediate strong interactions between particles which carry colour charge, such as quarks.  
 135 Since gluons carry colour charge, they interact with themselves. The massive, spin-0, electrically neutral Higgs  
 136 boson mediates the Higgs field which gives mass to the  $W^\pm$  and  $Z$  bosons via the so-called Brout-Englert-Higgs  
 137 mechanism [42, 50, 49]. The Brout-Englert-Higgs mechanism induces spontaneous electroweak symmetry breaking  
 138 to provide mass terms for the  $W^\pm$  and  $Z$  bosons in the electroweak Lagrangian of the SM. All particles described in  
 139 the SM have their own antiparticle, with the same mass, but opposite charges. Some particles, such as the photon,  
 140 are their own antiparticle.

141  
 142 Although the SM has shown to be hugely successful, it is incomplete and fails to describe certain observed phenomena.  
 143 The most notable example being the absence of gravity from the SM. The gravitational force is  $\approx 10^{29}$  [75]  
 144 weaker than the weak force, therefore quantum gravitational effects are expected to only become significant at  
 145 energies much larger than that currently accessible by the LHC (known as the Planck scale  $\approx 10^9$  GeV) [54]. This  
 146 large difference in strength between the weak force and gravity is known as the Hierarchy Problem. Cosmological  
 147 observations infer that around 84% of the matter in the universe consists of gravitationally interacting matter known  
 148 as dark matter [53]. None of the particles described in the SM are good dark matter candidates, therefore the SM  
 149 only accounts for a small fraction of the total matter of the universe. The large discrepancy between the observed  
 150 amount of matter and antimatter in the universe, sometimes referred to as the matter-antimatter asymmetry, is not  
 151 fully explained by the SM. Neutrinos in the SM are assumed to be massless, however observations of neutrino oscillations  
 152 (neutrinos undergoing flavour change as they travel through space) imply that neutrinos do have mass [45].  
 153 Beyond the Standard Model (BSM) theories attempt to explain the phenomena which the SM cannot. For example,  
 154 a popular extension to the SM, Supersymmetry (SUSY) introduces new particles to the SM which are counterparts  
 155 to the existing SM particles with the same quantum numbers, except for their spins [56]. SUSY provides elegant  
 156 explanations to many shortcomings of the SM, however none of the supersymmetric particles described by SUSY  
 157 have been observed experimentally [30].

### 158 2.1.1 The Top Quark

159 The top quark is the heaviest particle in the SM, with a mass of  $172.76 \pm 0.30$  GeV [48]. According to the SM, since  
 160 the coupling to the Higgs boson is proportional to the the mass of the interacting particle, the top quark is strongly  
 161 coupled to the Higgs boson. Physics processes involving top quarks is therefore a theoretically well-motivated area  
 162 to search for new physics, since it is the most likely particle to couple to new physics theories at the TeV scale. Its  
 163 large mass also makes it highly unstable, with a mean lifetime of  $\approx 0.5 \times 10^{-24}$  s [48]. The top quark's lifetime  
 164 is shorter than that of the hadronisation process, and it therefore decays before hadronising. The top quark can  
 165 therefore be measured indirectly via its decay products. Top quarks almost always decay to a  $W$  boson and a  
 166  $b$ -quark ( $\frac{\Gamma(Wb)}{\Gamma(Wq(q=b,s,d))} = 0.957 \pm 0.034$  [48]). The  $b$ -quark is the second heaviest quark in the SM, however its  
 167 lifetime is still longer than the hadronisation time scale [48]. In hadron collider experiments,  $b$ -quarks travel a short  
 168 distance in the detector before hadronising to form jets. In Table 2.1, the dominant final state branching fractions  
 169 of the top quark are shown.

170 Hadronic final states are more than twice as likely than leptonic final states. Final state decays to different lepton  
 171 flavours are roughly equally probable.

Decay Mode	Branching Fraction ( $\frac{\Gamma_i}{\Gamma}$ )
$t \rightarrow Wb \rightarrow e\nu_e b$	$(11.10 \pm 0.30)\%$
$t \rightarrow Wb \rightarrow \mu\nu_\mu b$	$(11.40 \pm 0.20)\%$
$t \rightarrow Wb \rightarrow \tau\nu_\tau b$	$(10.70 \pm 0.50)\%$
$t \rightarrow Wb \rightarrow q\bar{q}b$	$(66.50 \pm 1.40)\%$

Table 2.1: The dominant final state branching fractions of the top quark [48] are shown.

172  
173 Top quark production can be placed into two main categories: pair production ( $t\bar{t}$ ) and single-top production  
174 ( $t$ ) [73]. In the LHC, top quarks are mainly produced in pairs via strong interactions in gluon-gluon fusion ( $gg \rightarrow t\bar{t}$ )  
175 or quark annihilation ( $q\bar{q} \rightarrow t\bar{t}$ ). Top quark production via gluon-gluon fusion is the dominating process [24]. The  
176 production cross section for  $t\bar{t}$  (leptonic final state) in  $pp$  collisions with  $\sqrt{s} = 13$  TeV was measured by ATLAS with  
177 a value of  $830 \pm 0.4(\text{stat}) \pm 36(\text{syst}) \pm 14(\text{lumi})$  pb [4], with good agreement between measurement and theoretical  
178 prediction.

179  
180 Single top production occurs via the weak interaction. The most abundant production mechanisms leading to  
181 single top production are the  $s$ -,  $t$ - and  $Wt$ - channels [48]. In the  $s$ -channel, an initial quark annihilates with an  
182 anti-quark of different flavour, producing a virtual  $W$  boson which decays to a top quark and anti-bottom quark.  
183 In the  $t$ -channel, an initial  $b$  quark interacts with a different flavour quark via the exchange of a  $W$  boson. This  
184 interaction produces a top quark and another quark. In the  $Wt$ -channel, an initial gluon interacts with a  $b$  quark  
185 to produce a top quark and a  $W$  boson, either via the absorption of the gluon by the  $b$  quark or via the exchange  
186 of a top quark. In Table 2.2, single top production cross sections in  $pp$  collisions at  $\sqrt{s} = 13$  TeV for the  $s$ -,  $t$ - and  
187  $Wt$ -channels, are shown.

Channel	Process	Total Cross Section [pb]
$s$	$q\bar{q}' \rightarrow W \rightarrow \bar{b}t$	$10.32^{+0.40}_{-0.36}$
$t$	$bq' \rightarrow W \rightarrow tq$	$216.99^{+9.04}_{-7.71}$
$Wt$	$bg \rightarrow b/t \rightarrow Wt$	$71.7 \pm 3.85$

Table 2.2: Single top production cross sections in  $pp$  collisions at  $\sqrt{s} = 13$  TeV for the  $s$ -,  $t$ - and  $Wt$ -channels [31]  
are shown. The prime superscript on  $q'$  indicates that the quark has a different flavour to  $q$ .

188 Single top production is suppressed compared to pair produced top production, with  $t\bar{t}$  production (leptonic final  
189 state) being around three times as likely to occur than single top production across all decay channels.

### 190 2.1.1.1 Motivation for the search for $tWZ$ production in the tetralepton channel

191 The recent lack of signs of new physics from LHC data [74] tells us that new physics is either very heavy, or is  
192 very weakly coupled to SM particles. We therefore might only observe signs of new physics in anomalous rates of  
193 well-chosen processes.  $tWZ$  is a prime example of such a process. It has an extremely low production cross section  
194 ( $0.7$  fb for  $\sqrt{s} = 13$  TeV [25]), and has subsequently never been observed by any particle physics experiment. Since  
195  $tWZ$  involves a charged  $W$  boson and neutral  $Z$  boson, its cross section is sensitive to the charged and neutral  
196 couplings to the top quark. In turn, the top quark is strongly coupled to the Higgs boson, due to its large mass. Due  
197 to the top quark's large coupling to the Higgs boson, corrections to the Higgs boson mass diverge in the SM. The  
198 top quark's couplings are modified, in order to remove this divergence, in many scenarios of new physics that aim  
199 to resolve the Hierarchy Problem. Since the  $Z$  boson may be radiated from the initial-state  $b$ -quark, the final-state  
200 top quark, or the final-state  $Z$  boson, the  $tWZ$  process embeds the  $b - Z$ ,  $t - Z$  and  $W - Z$  electroweak couplings  
201 which are often modified in BSM physics. Therefore  $tWZ$  is an important process in the search for signs of new  
202 physics and BSM physics.

203

One such BSM theory which is sensitive to  $tWZ$  production [57, 63] is the Standard Model Effective Field Theory (SMEFT) [26]. The SMEFT attempts to describe physics at large energy scales which we have not yet been able to probe experimentally. The SMEFT inherits the same QFT framework as the SM, and adds Lagrangian terms to the SM Lagrangian which describe the interactions of SM particles at higher energy scales. Analogous to the coupling constants found in the SM Lagrangian, which indicate the interaction strengths between different particles, SMEFT contains scalar coefficients which operate in the same way. These scalar coefficients are known as Wilson coefficients. It has been shown that the cross section of  $tWZ$  is sensitive to many Wilson coefficients. An experimental constraint on the cross section of  $tWZ$  is therefore expected to be impactful on a global fit on all the Wilson coefficients in SMEFT.

Prior to this analysis, only three experimental studies of  $tWZ$  in ATLAS have been performed. The first and third studies utilised the trilepton channel to search for  $tWZ$  production, whereas the second study utilised both the tri- and tetralepton channels. The first search utilised  $36 \text{ fb}^{-1}$  of ATLAS data and an upper limit on the cross section of  $tWZ$  was set at a value of  $\approx 6$  times the SM cross section [67]. The second study investigated the feasibility of a cross section measurement of  $tWZ$  production with CMS Run 3 data ( $300 \text{ fb}^{-1}$ ) [Tschida:2020ftz]. The study showed that it is possible to exclude  $\mu(tWZ)$  at the  $7\sigma$  significance level using  $300 \text{ fb}^{-1}$  of data. This study needs to be further investigated, since its findings seem improbable given the results obtained in this thesis. The third search utilised  $139 \text{ fb}^{-1}$  of ATLAS data and an expected upper limit on the cross section of  $tWZ$  was set at a value of  $\approx 2.6$  times the SM cross section [81]. In Section 4.11.2, the latter analysis will be used in combination with this analysis, in order to further increase the sensitivity of the cross section of  $tWZ$ .

## 2.2 $tWZ$

### 2.2.1 Tetralepton Channel

In Figure 2.2, the Leading Order (LO) Feynman diagram for  $tWZ$  in the tetralepton channel, is shown.

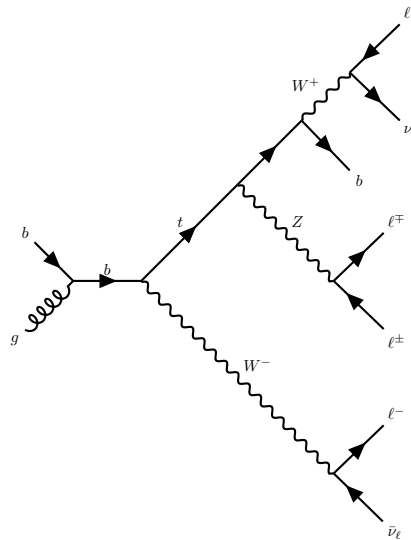


Figure 2.2: The LO Feynman diagram of  $tWZ$  production in the tetralepton channel is shown.

#### 2.2.1.1 Backgrounds

The main backgrounds for  $tWZ$  (tetralepton channel) are the production of a two tops, both in the  $\ell\nu b$  final state channel, together with a  $Z$  boson ( $t\bar{t}Z$ ) and diboson production with fully leptonic final states ( $ZZ$ ). In Figure 2.2.1.1, LO Feynman diagrams for  $t\bar{t}Z$  and  $ZZ$  in the tetralepton channel, are shown.

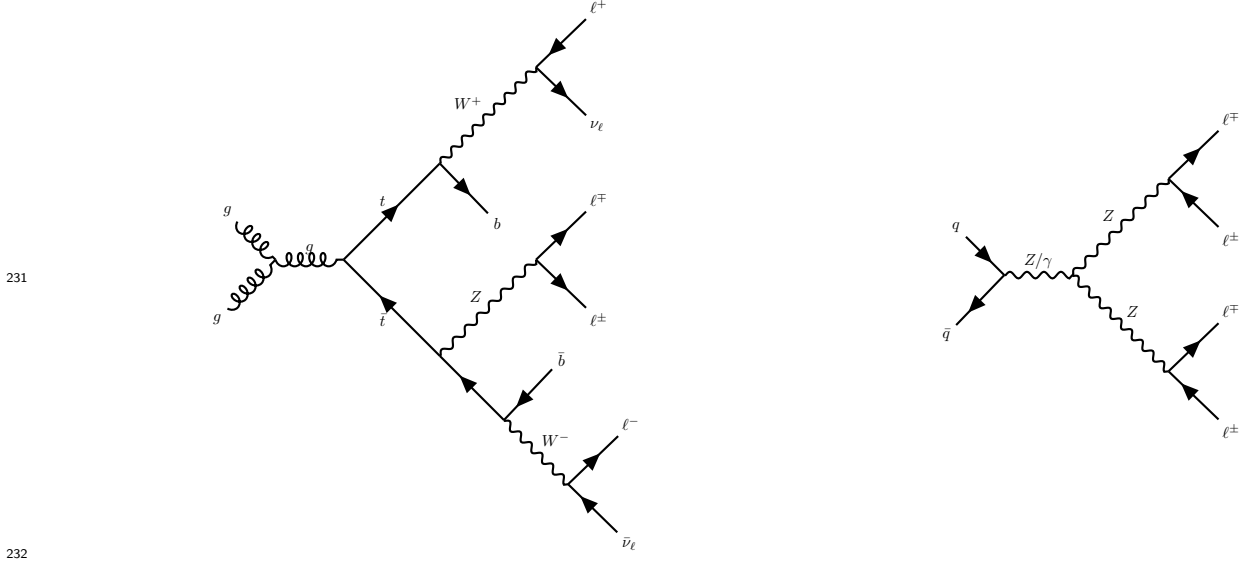


Figure 2.3: LO Feynman diagrams for  $t\bar{t}Z$  (left) and  $ZZ$  (right) in the tetralepton channel are shown.

233 The  $t\bar{t}Z$  process contains four leptons and two  $b$ -quarks in its final state (inclusive  $\sigma(t\bar{t}Z) = 0.95 \pm 0.08_{\text{stat}} \pm 0.10_{\text{syst}}$   
234 pb at  $\sqrt{s} = 13$  TeV [2]) and can easily mimic the  $tWZ$  signal process, for instance, by one of its  $b$ -jets getting  
235 missed during detection. The  $ZZ$  process contains four leptons and zero  $b$ -quarks in its final state (inclusive  
236  $\sigma(ZZ) = 14.6^{+1.9}_{-1.8}(\text{stat})^{+0.5}_{-0.3}(\text{syst}) \pm 0.2(\text{theo}) \pm 0.4(\text{lumi})$  pb at  $\sqrt{s} = 13$  TeV [55]). One way in which  $ZZ$  can mimic  
237 the  $tWZ$  signal process is by reconstruction of a non-prompt  $b$ -jet.

### 238 2.2.2 Comparison to Trilepton Channel

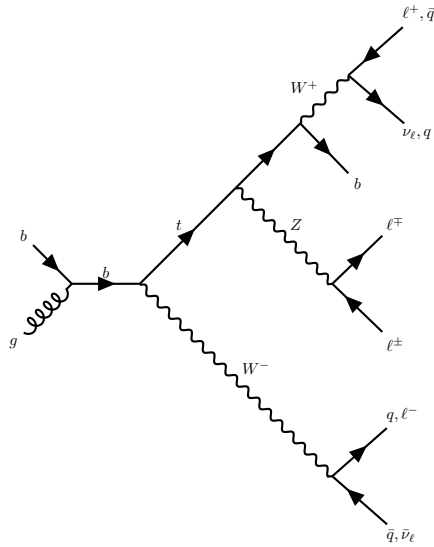


Figure 2.4: Example Feynman diagram of  $tWZ$  production in the tri-lepton channel.

239 The most apparent difference between the tri and tetralepton channels is the amount of statistics present, with the  
240 tetralepton channel having far less events in its phase space than that of the tri-lepton channel. The lack of statistics  
241 in the tetralepton channel can be attributed to its low production cross section,  $\sigma_{(tW^\pm Z).Br(4\ell)}^{\text{NLO}} = 0.7$  fb [25].  
242 The tri-lepton channel has a production cross section ( $\sigma_{(tW^\pm Z).Br(3\ell)}^{\text{NLO}} = 3.9$  fb [25]) around a factor of 4 larger  
243 than that of the tetralepton channel. This difference between the production cross section of the two decay  
244 channels can be largely attributed to the difference in branching ratios ( $\frac{\Gamma_i}{\Gamma}$ ) between a hadronically decaying  $W$

245 boson,  $\frac{\Gamma_{W \rightarrow had}}{\Gamma_W} = (67.41 \pm 0.27)\%$  [48], present in the tri-lepton channel and a leptonically decaying  $W$  boson,  
246  $\frac{\Gamma_{W \rightarrow \ell\nu}}{\Gamma_W} = (10.86 \pm 0.09)\%$  [48], present in the tetralepton channel.

247

248 Despite the tetralepton channel's low statistics, it is not subject to the large  $WZ$  background present in the trilepton  
249 channel [81]. The tetralepton channel has a substantial amount of  $ZZ$  background (not present in the trilepton  
250 channel), fortunately this can be easily suppressed due to the full reconstructability of the two leptonically decaying  
251  $Z$ -bosons.

252

# Chapter 3

## The ATLAS Experiment and Detector

253

### 3.1 The ATLAS Experiment

255 The ATLAS (A Toroidal LHC ApparatuS) detector is one of two general purpose detectors at CERN (the European  
 256 Organization for Nuclear Research) near Geneva in Switzerland. These detectors collect data from the collisions  
 257 provided by the worlds highest energy particle accelerator [27], the Large Hadron Collider (LHC) situated at CERN.

258 In this section, information about the LHC and the ATLAS detector are given. This includes technical aspects  
 259 of the ATLAS detector and the processing of data into meaningful physics objects<sup>1</sup> to be used in analyses. The  
 260 following chapter consists of information from "The LHC Design Report" [27], "LHC Machine" [44] and "The  
 261 ATLAS Experiment at the CERN Large Hadron Collider" [37] unless otherwise stated.

#### 3.1.1 Large Hadron Collider (LHC)

263 The LHC is a circular 27 km particle accelerator located in an underground tunnel on the border between France  
 264 and Switzerland. The accelerator consists of supercooled, superconducting magnets which accelerate and collide  
 265 beams of protons at centre-of-mass energies up to  $\sqrt{s} = 13$  TeV at instantaneous luminosities of  $\mathcal{L} \sim 10^{34}$  cm $^{-2}$ s $^{-1}$ .  
 266 In the LHC,  $pp$  beams consist of bunches of protons which collide every 25 ns, corresponding to a frequency of 40  
 267 MHz. Several accelerator systems are used to accelerate protons and heavy ions to such high energies. Protons are  
 268 extracted from a tank of ionised hydrogen gas and are injected into the Linear Accelerator 2 (LINAC), where they  
 269 are linearly accelerated to momenta of 50 MeV. The proton bunches are then sequentially accelerated by a chain  
 270 of circular accelerators. The chain starts with the Booster which accelerates the protons to momenta of up to 1.4  
 271 GeV. The proton bunches are then fed through to the Proton Synchrotron (PS) and the Super Proton Synchrotron  
 272 (SPS) which accelerate the protons to momenta of up to 25 GeV and 450 GeV respectively. The protons are  
 273 then transferred to two beam pipes of the LHC where they travel in opposite directions. Both proton beams are  
 274 accelerated to their final momenta of 6.5 TeV, resulting in a centre-of-mass energy of 13 TeV. These proton beams  
 275 then collide at one of the four main interaction points (positions along the beam pipe where collisions occur)  
 276 situated along the LHC.

277 The four main experiments located at the interaction points are ATLAS, the Compact Muon Solenoid (CMS),  
 278 Large Hadron Collider Beauty (LHCb) Experiment and A Large Ion Collider Experiment (ALICE). The ATLAS  
 279 and CMS detectors are general-purpose detectors which investigate a wide range of physics processes. Since both  
 280 ATLAS and CMS can measure the same processes, they are able to cross-check and validate measurements taken  
 281 by one another. The LHCb detector is specifically designed to study decays of particles containing  $b$ -quarks. The  
 282 ALICE detector is designed to study the strongly interacting quark-gluon plasma which is formed at extremely  
 283 high energy densities. At the interaction points, the two proton beams which consist of protons in closely packed  
 284 bunches, travel in opposite directions to one another and collide. Many hard  $pp$  collisions (events) can occur per  
 285 bunch crossing, however it is the most energetic collision in the bunch crossing that is interesting for discovery  
 286 potential. The most energetic collision is therefore chosen to be studied and any additional collisions are aimed  
 287 to be rejected. These additional collisions are referred to as *pile-up*. Pileup complicates the reconstruction of the  
 288 particles originating from the hard collision of interest.

<sup>1</sup>meaningful physical systems which can be reconstructed from detector information (e.g leptons and jets)

291 **3.1.1.1 Luminosity**

292 This section consists of information from "Modern Particle Physics" [75], unless otherwise stated.

293

294 The event production rate at the LHC,  $R(t)$ , for a certain process of interest is given by,

$$R(t) = \mathcal{L}(t)\sigma \quad (3.1)$$

295 where  $\mathcal{L}(t)$  is the instantaneous luminosity and  $\sigma$  and is the cross section of the process of interest. The instantaneous  
296 luminosity,  $\mathcal{L}(t)$ , is independent on the process of interest, and depends on various collider and beam parameters.  
297  $\mathcal{L}(t)$  can be written in terms of these parameters as,

$$\mathcal{L}(t) = f \frac{N n_1 n_2}{4\pi \sigma_x \sigma_y} \quad (3.2)$$

298 where  $f$  is the beam revolution frequency,  $N$  is the number of proton bunches colliding per second,  $n_1$  and  $n_2$  are the  
299 number of protons in the colliding bunches,  $\sigma_x$  and  $\sigma_y$  are the beam spread in the  $x$  and  $y$  directions respectively.  
300 The total integrated luminosity,  $L$ , across some time interval, is given by,

$$L = \int \mathcal{L} dt. \quad (3.3)$$

301 The units of  $L$  are inverse area, and are given by  $\text{fb}^{-1}$  at the LHC and the ATLAS detector. In Figure 3.1, the  
302 total integrated luminosity delivered to ATLAS, recorded by ATLAS, and certified to be good enough for physics  
303 analyses (the data passes certain quality control criteria) for  $\sqrt{s} = 13$  TeV  $pp$  collisions at the LHC is shown [77].

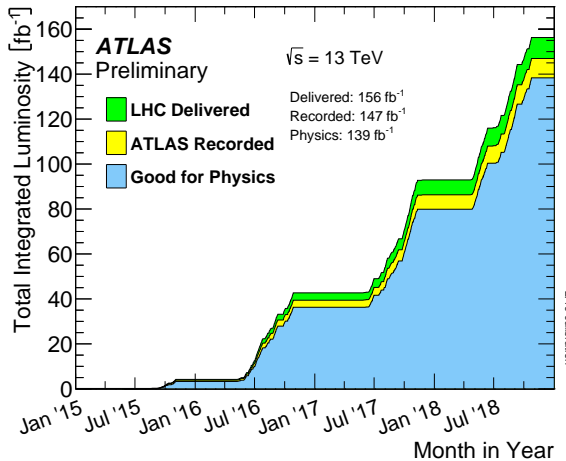


Figure 3.1: The total integrated luminosity delivered to ATLAS, recorded by ATLAS, and certified to be good enough for physics analyses (the data passes certain quality control criteria) for  $\sqrt{s} = 13$  TeV  $pp$  collisions at the LHC is shown [77]. The total integrated luminosity delivered by the LHC, recorded by ATLAS and certified to be good quality data are shown by the green, yellow and blue histograms respectively. The month and year of data taking is shown on the x-axis and the total integrated luminosity (in  $\text{fb}^{-1}$ ) is shown on the y-axis.

304 A total integrated luminosity of  $139 \text{ fb}^{-1}$  of data certified as good for physics was recorded by ATLAS between  
305 2015 and 2018. This data taking period is referred to as Run 2, since it proceeds the Run 1 data taking period  
306 (2011 and 2012) and the Long Shutdown 1 LHC upgrade period (2013 and 2014). In this analysis, we use the Full  
307 Run 2 dataset.

308 **3.2 The ATLAS Detector**

309 In Figure 3.2, the schematic of the ATLAS detector, is shown.

310 The detector is cylindrically shaped which covers close to  $4\pi$  in solid angle. It has a length of 44 m, a diameter  
311 of 25 m and a mass of 7000 tons. The ATLAS detector consists of four main sub-detectors arranged in concentric  
312 cylindrical layers around the beam pipe. These include the inner detector, the electromagnetic calorimeter, the

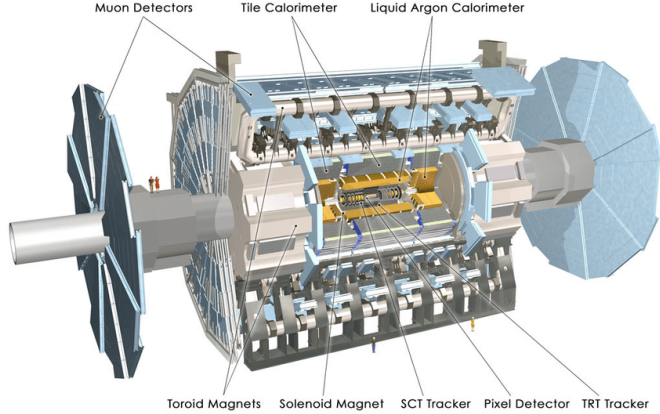


Figure 3.2: Schematic of the ATLAS detector [37]

hadronic calorimeters and the muon spectrometer. The sub-detectors record the momenta, energies and trajectories of different particles produced in the collider, allowing for the reconstruction and identification of these particles to be used in physics analyses.

### 3.2.1 Coordinate System and Kinematics

The ATLAS detector adopts a right-handed coordinate system. The origin is at the nominal interaction point with the  $z$ -axis defined to be counter-clockwise along the beam line. The  $x - y$  plane (or transverse plane) is perpendicular to the beam line, with the  $x$ -axis pointing towards the centre of the LHC ring and the  $y$ -axis pointing upwards towards the Earth's surface. The azimuthal angle,  $\phi \in [-\pi, \pi]$ , is measured in the transverse plane with respect to the positive  $x$ -axis. The polar angle,  $\theta \in [0, \pi]$ , is measured in the  $z - y$  plane with respect to the positive  $y$ -axis. A quantity called the pseudorapidity,  $\eta \in [0, \infty]$  is defined as,

$$\eta = -\ln \tan\left(\frac{\theta}{2}\right) \quad (3.4)$$

$\eta$  is often used as a measure of the polar angle, instead of  $\theta$ , since the difference in  $\eta$  between two particles,  $\Delta\eta$ , is invariant under a Lorentz boost in the  $z$ -direction [78]. The angular distance between two physics objects,  $\Delta R$ , can be written as,

$$\Delta R = \sqrt{(\Delta\phi)^2 + (\Delta\eta)^2} \quad (3.5)$$

where  $\Delta\phi$  is the difference in  $\phi$  between the two physics objects of interest. Quantities defined in the transverse plane are often used to describe the kinematics of physics objects in hadron collider experiments. The transverse momentum,  $p_T$ , is defined as,

$$p_T = \sqrt{(p_x)^2 + (p_y)^2} \quad (3.6)$$

where  $p_x$  and  $p_y$  are the  $x$  and  $y$  components of the physics object's momenta, respectively. The transverse energy,  $E_T$ , is defined as,

$$E_T = \sqrt{m^2 + p_T^2} \quad (3.7)$$

where  $m$  is the invariant mass of the physics object.

### 3.2.2 Inner Detector

The inner detector is the first layer of concentric cylindrical sub-detector layers in the ATLAS detector. It is used to identify charged particles and reconstruct the trajectories of charged particles produced in the collisions via energy deposition in semiconductor material (hits) and the ionisation of gas. It consists of three complementary sub-detectors (in order from nearest to farthest from the beam pipe): the Pixel Detector, the Semiconductor Tracker (SCT) and the Transition Radiation Detector (TRT). The Pixel Detector and SCT are based on semiconductor technology and have the highest granularity of any sub-detector in ATLAS, in order to cope with the high frequency

339 of collisions near the interaction point. The TRT consists of drift tubes (straws) containing a gas mixture, which  
 340 allows measurement of the energy deposited by charged particles through the ionisation of the gas. Solenoid magnets  
 341 surround the inner detector and bend the trajectories of charged particles. The charges and momenta of particles  
 342 can be inferred from their bent trajectories, which are reconstructed by the hits produced via energy deposition in  
 343 the Inner Detector.

### 344 3.2.3 Electromagnetic and Hadronic Calorimeters

345 The Electromagnetic Calorimeter (ECAL) and Hadronic Calorimeter (HCAL) surround the Inner Detector, with  
 346 the ECAL nearer to the beam line. The ECAL and HCAL provide accurate measurements of the energy of  
 347 particles which interact electromagnetically (e.g. photons and electrons) and hadronically (e.g. jets), respectively.  
 348 Particles entering the calorimeters interact with the detector material and create either a electromagnetic shower  
 349 (in the ECAL) or a hadronic shower (in the HCAL), depositing all their energy in the calorimeter cells. The  
 350 primary mechanism of energy deposition in the ECAL is through bremsstrahlung (for electrons) and pair production  
 351 (photons). Hadrons usually deposit a small amount of their energy in the ECAL, and interact via inelastic scattering  
 352 with the nuclei of the detector material. The hadronic showers (jets) produced in these nuclear interactions travel  
 353 much further than an electromagnetic shower, and for that reason, the volume of the HCAL is designed to occupy  
 354 a much larger space than that of the ECAL.

### 355 3.2.4 Muon Spectrometer

356 The Muon Spectrometer (MS) is the outermost sub-detector of ATLAS and surrounds the HCAL. Muons traverse  
 357 through the inner detector and calorimeters, with minimal energy loss, before reaching the MS. The MS consists  
 358 of trigger and high-precision tracking systems. Large superconducting toroid shaped magnets deflect the incoming  
 359 muons to measure their trajectories and subsequently their momenta via the curvature of the trajectories. The MS  
 360 measures muon trajectories as they ionize gas (filled with Ar and CO<sub>2</sub> gas) in the MS drift chambers.

### 361 3.2.5 Trigger and Data Acquisition System

362 The Trigger and Data Acquisition System (TDAQ) manages and handles the large amount of data produced within  
 363 the ATLAS detector. In Run 2,  $pp$  bunch crossings occur every 25 ns, corresponding to an event rate of 40 MHz.  
 364 The TDAQ system performs a fast preliminary reconstruction to select events with signatures which are interesting  
 365 for physics analyses. The information collected from these events are permanently stored for offline reconstruction  
 366 and analysis, and the rest (the vast majority of events) are discarded. The trigger system reduces the 40 MHz data  
 367 rate to around 1 kHz.

### 368 3.2.6 Particle Identification and Object Reconstruction

369 Particles originating from  $pp$  collisions, or from their subsequent decays, traverse through the ATLAS detector and  
 370 interact with its different sub-detectors, producing characteristic electronic signals. These signals are then processed  
 371 by various algorithms to reconstruct and identify the physics objects (e.g. electrons, muons, jets) in the event. This  
 372 section outlines the procedures used to define these physics objects.

#### 373 3.2.6.1 Tracks and primary vertices

374 The trajectories of charged particles, or tracks, are reconstructed in the ID. First, energy is deposited by charged  
 375 particles (hits) in pixels or strips, in the Pixel and SCT detectors respectively. Adjacent pixels or strips are grouped  
 376 together in *energy clusters*. Energy clusters define 3D space-points indicating the location where the charged  
 377 particle traversed. Track seeds are then defined as sets of three space-points, in either the Pixel or SCT detectors.  
 378 A Kalman filter [10] is then used to build track candidates from the track seeds. Often, multiple track candidates  
 379 are built per track seed, therefore an ambiguity solver [35] is needed for finding the track which best represents the  
 380 traversal of the charged particle. The ambiguity solver ranks each track from a given seed based on, the number of  
 381 associated hits, the number of holes (expected hits which are absent), track momenta and the  $\chi^2$  of the track fit.  
 382 Low ranked tracks are then discarded. High ranked tracks are refitted, introducing information from the TRT.

383 The primary vertex is the location of the  $pp$  collision of interest (i.e. from the hard scatter). The primary vertex  
 384 from the hard scatter needs to be identified, to isolate the event of interest from unwanted pile-up events. In the

386 event reconstruction procedure [62], the primary vertex is defined as the vertex of the event with the largest sum  
 387 of  $(p_T)^2$  (corresponding to the measured  $(p_T)^2$  of the particle from its reconstructed track) of its associated tracks.  
 388 Furthermore, the primary vertex is required to have at least two associated tracks. To reduce contamination from  
 389 fake tracks used in primary vertex reconstruction, only tracks which pass certain tight selection criteria are used  
 390 in the reconstruction procedure. An iterative fitting procedure is then used to reconstruct the primary vertex by  
 391 finding a set of reconstructed tracks which have a common vertex.

### 392 3.2.6.2 Electrons

393 Since electrons are charged particles, they give rise to tracks in the Inner Detector and deposit energy in the  
 394 ECAL via electromagnetic showering. Electrons are therefore reconstructed and identified from signals in the Inner  
 395 Detector and ECAL. Electrons are reconstructed using a dynamic clustering algorithm [1] which matches electron  
 396 candidate tracks in the Inner Detector to energy clusters in the ECAL. The dynamic clustering algorithm matches  
 397 tracks to energy clusters which have local maxima, to form electron candidates.

398 A likelihood discriminant is used to identify electrons. Quantities measured in the Inner Detector and ECAL  
 399 are used as input, such that they discriminate well between prompt isolated electrons and other physics objects  
 400 (e.g. jets, electron from a photon conversion, electron from a semi-leptonically decaying hadron). Important input  
 401 variables include the shape of the electromagnetic shower, track quality in the Inner Detector and information from  
 402 the TRT.

### 403 3.2.6.3 Muons

404 Muons leave tracks in the Inner Detector and the MS. They traverse the ECAL and HCAL with no significant  
 405 energy loss. Muons are therefore reconstructed and identified from information in the Inner Detector and MS.  
 406 Tracks are reconstructed [5] in the Inner Detector and MS independently. Both tracks are combined, using a global  
 407  $\chi^2$  fit, resulting in reconstructed muon candidates.

408 Similar to electron identification, muons use a likelihood discriminant to identify prompt muons and suppress  
 409 background contamination (mainly from pion and kaon decays).

### 411 3.2.6.4 Jets and $b$ -tagging

412 Coloured particles emerging from the interaction point result in collimated streams of colourless particles, known  
 413 as jets. Jets deposit energy in the Inner Detector and in the HCAL. Jets in ATLAS are reconstructed from  
 414 topological clusters using the anti- $k_t$  algorithm [28]. Topological clusters are groups of adjacent calorimeter cells  
 415 which contain energy deposition above the average amount of noise expected in the cell. Adjacent cells are grouped  
 416 together under certain criteria to form topological clusters which form jets.

417 Different tagging algorithms are used to identify the quark flavour which initiated a jet.  $b$ -quark tagging is used  
 418 extensively in top physics, due to the  $b$ -quark present in the top quark's dominant decay channel (See Table 2.1).  
 419 Hadrons arising from  $b$ -quark hadronisation have mean lifetimes  $\sim 1.5$  ps and travel (on average) a few mil-  
 420 limetres before decaying. This creates a secondary vertex within the jet (See Figure 3.3). This characteristic decay  
 421 signature, along with several other unique features of  $b$ -jets, are exploited in  $b$ -tagging algorithms to distinguish  
 422  $b$ -jets from  $c$ - or light flavour jets. In Figure 3.3, an illustration of the production of a  $b$ -jet, is shown.  
 423 In this analysis, we use the recommended DL1r (Deep-Learning Flavour Tagger) tagging algorithm [18]. The DL1r  
 424 algorithm combines outputs from several low-level tagging algorithms using a Deep Neural Network and outputs  
 425 the probability that a given input jet is identified as a  $b$ ,  $c$  or light flavoured jet.

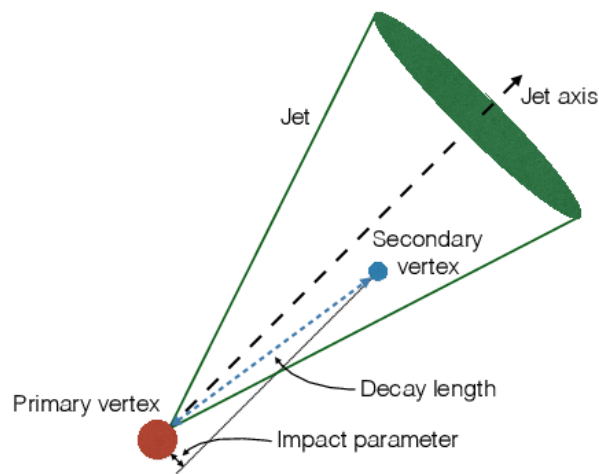


Figure 3.3: An illustration [38] of the production of a  $b$ -jet is shown. This illustrates the presence of a secondary vertex within a  $b$ -jet.

427

# Chapter 4

428

# Analysis Setup and Strategy

429 In this chapter, the setup of the analysis and the analysis strategy is presented for  $tWZ$  production in the tetralepton  
 430 channel based on an integrated luminosity of  $139 \text{ fb}^{-1}$  of data recorded by ATLAS. This includes a description of the  
 431 data and simulated Monte Carlo (MC) samples, definitions of physics objects, event selection and the subsequent  
 432 definition of signal and control regions used in this analysis. Furthermore, estimation of the fake lepton component  
 433 using the MC template method is described. Various Machine Learning techniques and a kinematic reconstruction  
 434 algorithm, used to discriminate between signal and background events, are described. An outline of the systematic  
 435 uncertainties affecting the measurement are presented. Finally, the results of the analysis are presented.

436 **4.1 Data and Monte Carlo Simulation**

437 **4.1.1 Data Samples**

438 The  $pp$  collision data used in this analysis was collected with the ATLAS detector at the LHC from 2015 to 2018. This  
 439 data period of data taking is referred to as Run 2. During this period,  $pp$  collisions at  $\sqrt{s} = 13 \text{ TeV}$ , corresponding  
 440 to an integrated luminosity ( $\mathcal{L}$ ) of  $156 \text{ fb}^{-1}$ , were delivered by the LHC. The ATLAS detector managed to record  
 441  $147 \text{ fb}^{-1}$  of this total delivered data.  $139 \text{ fb}^{-1}$  of the data recorded by ATLAS is considered to be good enough  
 442 for physics analyses (the data passes certain quality control criteria) and placed into the *Good Runs List* [47].  
 443 Specific time-intervals where the luminosity is assumed to be constant are known as *lumi-blocks*. Only events from  
 444 lumi-blocks in which LHC beams were stable and all ATLAS detectors were operational are selected. The list of  
 445 suitable run and lumi-blocks is summarised in the official Good Runs Lists for 2015-2018 data, as specified in  
 446 Ref. [goodrunlist]. The integrated luminosities corresponding to the individual datasets for years 2015, 2016,  
 447 2017 and 2018 are  $3.2 \text{ fb}^{-1}$ ,  $33.0 \text{ fb}^{-1}$ ,  $44.3 \text{ fb}^{-1}$  and  $58.5 \text{ fb}^{-1}$  respectively.

448 **4.1.2 Monte Carlo Samples**

449 Simulated MC samples were generated and used to model the SM  $tWZ$  signal and its backgrounds.

450 The following background processes are considered:

- 452 •  **$t\bar{t}Z$ :**  $t\bar{t}$  with an associated  $Z$ -boson, in the tetralepton final state. Therefore, both top-quarks decay leptonically  
 453 (e.g.  $t \rightarrow W^+ b \rightarrow \ell^+ \nu b$ ) and of these top-quarks emits a  $Z$ -boson which decays leptonically ( $Z \rightarrow \ell^\pm \ell^\mp$   
 454 (OSSF lepton pair)). This results in a final state with 4 leptons and 2 b-quarks.
- 455 •  **$ZZ$ :** Diboson production with a tetralepton final state, therefore both  $Z$ -bosons decay leptonically ( $Z \rightarrow \ell^\pm \ell^\mp$   
 456 (OSSF lepton pair)).
- 457 • **other:** Processes with a relatively minimal, but non-negligible background contribution
  - $VVV (V = W/Z)$
  - $t\bar{t}$
  - $t\bar{t}W$
  - $t\bar{t}WW$

- 462      -  $t\bar{t}H$   
 463      -  $WZ$   
 464      -  $t\bar{t}t$   
 465      -  $t\bar{t}t\bar{t}$   
 466      -  $tZq$

467 The MC simulations are achieved via the use of event generators and parton shower generators. Event generators  
 468 simulate the  $pp$  collisions (hard events) by sampling the proton's Parton Distribution Functions (PDFs) at the  
 469 desired energy scale. The parton shower generators simulate any incoming or outgoing particles from the hard  
 470 process, which carry QCD color charge and can therefore lead to parton showers.

471 The production of  $tWZ$  events is simulated with the **MADGRAPH5\_AMC@NLO 2.3.3** generator providing matrix element  
 472 (ME) calculations at NLO in QCD. The events are interfaced with **PYTHIA 8.235** for the parton shower. The  
 473 production of  $t\bar{t}Z$  and  $t\bar{t}W$  events are simulated with the **MADGRAPH5\_AMC@NLO 2.3.3** generator providing ME  
 474 calculations at NLO in QCD. The events are interfaced with **PYTHIA 8.210** for the parton shower. Event generation  
 475 of  $tWZ$  and  $t\bar{t}Z$  results in diagrams which overlap with one another, that is, these diagrams contain the same initial  
 476 and final state particles. Several methods exist in order to separate between the two processes, by removing the  
 477 overlap, therefore avoiding double counting. There are two different diagram removal procedures, diagram removal  
 478 procedure 1 (DR1) [40] and diagram removal procedure 2 (DR2). The DR1 scheme is used to remove the overlap  
 479 (interference) between  $tWZ$  and  $t\bar{t}Z$ . A comparison to the DR2 scheme is used to estimate part of the theoretical  
 480 systematic on the modelling of the  $tWZ$  signal (See Section 4.9.2). Diboson processes which feature the three  
 481 charged leptons and one neutrino or four charged lepton in their final states, such as  $WZ$  and  $ZZ$ , are simulated  
 482 using **SHERPA 2.2.2** at NLO in QCD precision. The events are interfaced with **SHERPA** for the parton shower.  
 483 Triboson processes such as  $WWW$ ,  $WWZ$ ,  $WZZ$ , and  $ZZZ$  containing up to six leptons in their final states are  
 484 simulated using **SHERPA 2.2.2** at NLO in QCD precision. The events are interfaced with **SHERPA** for the parton  
 485 shower. The production of  $t\bar{t}$  events are simulated with the **POWHEG** generator providing ME calculations at NLO  
 486 in QCD. The events are interfaced with **PYTHIA 8.210** for the parton shower. The production of  $t\bar{t}t$ ,  $t\bar{t}\bar{t}$  and  
 487  $t\bar{t}WW$  are simulated using the **MADGRAPH5\_AMC@NLO 2.2.2** generator at LO precision. The events are interfaced  
 488 with **PYTHIA 8.186** for the parton shower. The production of  $t\bar{t}$  with an associated Higgs boson,  $t\bar{t}H$ , are generated  
 489 using the **MADGRAPH5\_AMC@NLO 2.6.0** generator at NLO in QCD precision. The events are showered using **PYTHIA**  
 490 8.230. The production of  $t\bar{t}$  events are simulated with the **POWHEG** generator providing ME calculations at NLO  
 491 in QCD. The events are showered using **PYTHIA 8.230**. The production of a single top quark in association with  
 492 a  $Z$ -boson and an extra parton,  $tZq$ , is simulated using **MADGRAPH5\_AMC@NLO 2.3.3** at NLO in QCD precision.  
 493 The events are interfaced with **PYTHIA 8.230** for the parton shower. In Table 4.1, the event generator and parton  
 494 shower used for each process's sample are shown.

Process	Event Generator	Cross section calculation	Parton Shower
$tWZ$	<b>MADGRAPH5_AMC@NLO 2.3.3</b>	NLO	<b>PYTHIA 8.235</b>
$t\bar{t}Z$	<b>MADGRAPH5_AMC@NLO 2.3.3</b>	NLO	<b>PYTHIA 8.210</b>
$ZZ, WZ$	<b>SHERPA 2.2.2</b>	NLO	<b>SHERPA</b>
$VVV (V = W/Z)$	<b>SHERPA 2.2.2</b>	NLO	<b>SHERPA</b>
$t\bar{t}$	<b>POWHEG</b>	NLO	<b>PYTHIA 8.230</b>
$t\bar{t}W$	<b>MADGRAPH5_AMC@NLO 2.3.3</b>	NLO	<b>PYTHIA 8.210</b>
$t\bar{t}WW$	<b>MADGRAPH5_AMC@NLO 2.2.2</b>	LO	<b>PYTHIA 8.186</b>
$t\bar{t}H$	<b>MADGRAPH5_AMC@NLO 2.6.0</b>	NLO	<b>PYTHIA 8.230</b>
$t\bar{t}t, t\bar{t}\bar{t}$	<b>MADGRAPH5_AMC@NLO 2.2.2</b>	LO	<b>PYTHIA 8.186</b>
$tZq$	<b>MADGRAPH5_AMC@NLO 2.3.3</b>	NLO	<b>PYTHIA 8.230</b>

Table 4.1: The event generator and parton shower used for the signal and background process's MC samples is shown.

## 496 4.2 Objects

497 In this section the physics objects (leptons, jets and  $b$ -tagged jets) used in this analysis are outlined.

### 4.2.1 Leptons

In this analysis only  $e$  and  $\mu$  leptons are considered, since  $\tau$  leptons are difficult to detect in the ATLAS detector.  $\tau$  leptons are challenging to detect since they have an extremely short lifetime ( $290.3 \pm 0.5$  fs [48]) which causes them to decay before reaching any detector components and therefore can only be reconstructed via their decay products. In addition to our selection criteria of exactly four leptons, it is required that the Leading (L), Next-to-Leading (NL), Next-to-Next-to-Leading (NNL) and Next-to-Next-to-Next-to-Leading (NNNL) leptons have  $p_T$  greater than 28, 18, 10 and 10 GeV respectively. Relatively loose object-level cuts are chosen in an attempt to maximize our signal statistics, since the analysis is heavily statistically limited. Reconstructed electrons are required to be within  $|\eta| < 2.47$  and excluding the transition region between the barrel and end-cap calorimeters at  $1.37 < |\eta| < 1.52$ . Reconstructed muons are required to be within  $|\eta| < 2.5$ . The transverse impact parameter,  $d_0$ , is defined as the minimal spatial distance between the object's (referring to leptons) trajectory and the primary vertex (the vertex associated with the  $p$ - $p$  hard scatter). The longitudinal impact parameter,  $z_0$ , is defined as the value of  $z$  of the point on the object's trajectory which determines  $d_0$ . To ensure consistency between the lepton and the primary vertex, it is required that  $|\frac{d_0}{\sigma(d_0)}| < 5$ ,  $|z_0 \sin \theta| < 0.5$  mm for electrons and  $|\frac{d_0}{\sigma(d_0)}| < 3$ ,  $|z_0 \sin \theta| < 0.5$  mm for muons, following the current recommendations [76]. To avoid instances where one detector signal can result in multiple different reconstructed objects, an overlap removal is applied which ignores all but one of these objects (See Section 4.2.4). Electrons are selected using a likelihood based discriminant [1] which takes measurements from the tracking system, calorimeter system and quantities derived from both the tracking and calorimeter system as input. Muons are selected using the Muon Selection Tool [66]. Loose electrons are defined with the criteria above, using the `LooseAndBLayerLH` ( $\sim 91\%$  selection efficiency for electrons with  $E_T > 30$  GeV [41]) identification algorithm (which has a certain cut applied). Similarly, tight electrons are defined with the criteria above, using the `TightLH` ( $\sim 80\%$  selection efficiency for electrons with  $E_T > 30$  GeV [41]) algorithm (which has a certain cut applied). Both loose and tight muons use the `Medium` ( $\sim 95\%$  selection efficiency [5]) algorithm (which has a certain cut applied). Tight leptons additionally require that they are sufficiently isolated from other particles produced in the collision. This is done by defining a cone of radius  $\Delta R = \sqrt{\Delta\eta^2 + \Delta\phi^2}$  around the particle of interest and summing the  $p_T$  of all the reconstructed particles surrounding the particle of interest, situated within the cone. A quantity,  $I_{rel}$ , is then defined as  $I_{rel} = \frac{\sum p_T(\text{surrounding candidate})}{p_T(\text{candidate})}$ , the ratio of this sum to the  $p_T$  of the lepton candidate. If this value is large, it is likely that the particle of interest originated from a jet (together with many other particles), whereas a prompt decay product resulting from the hard scatter will have little to no energy surrounding it ( $I_{rel} \ll 1$ ). The `IsolationSelectionTool` with the `PLVTight` ( $\sim 70\%$  efficiency [7]) and `PLVTight` ( $\sim 70\%$  efficiency at  $p_T = 30$  GeV [34]) algorithm are used for tight electrons and tight muons respectively (following the current recommendations [70]). In Table 4.2, a summary of the selection criteria for leptons is shown.

	Electrons		Muons	
	Tight	Loose	Tight	Loose
$p_T$ cuts		$p_T(\ell_1, \ell_2, \ell_3, \ell_4) > (28, 18, 10, 10)$ GeV		
Overlap Removal		Described in Section 4.2.4		
$\eta$ cuts	$ \eta(\ell_e)  < 2.47$ excluding $1.37 <  \eta(\ell_e)  < 1.52$		$ \eta(\ell_\mu)  < 2.5$	
Impact Parameters	$ \frac{d_0}{\sigma(d_0)}  < 5$ , $ z_0 \sin \theta  < 0.5$ mm		$ \frac{d_0}{\sigma(d_0)}  < 3$ , $ z_0 \sin \theta  < 0.5$ mm	
Identification WP	TightLH	LooseAndBLayerLH	Medium	Medium
Isolation WP	PLVTight	Not Used	PLVTight	Not Used

Table 4.2: A summary of the requirements applied for selecting tight and loose leptons ( $e, \mu$ ) is shown.

### 4.2.2 Jets

Jets are reconstructed using the anti- $k_t$  algorithm (See Section 3.2.6.4). The `AntiKt4EMPFflowjets` ( $\sim 97\%$  average efficiency with JVT (outlined in the subsequent paragraph)  $> 0.2$  [76]) algorithm (which has a certain cut applied) is used, following the current recommendations [76]. The jet-vertex-tagger (JVT) and the forward jet-vertex-tagger (fJVT) are likelihood discriminant which aim to suppress pile-up jets. The `Medium` algorithm (which has a certain cut applied) is used for the JVT and the fJVT (following the current recommendations [69]). Additionally, a requirement that jets have a JVT value greater than 0.5 is applied. In the same way as with leptons, ambiguities are removed where one detector signal can result in multiple different reconstructed objects, via overlap removal

(See Section 4.2.4). Jets are required to be within  $p_T(\text{jet}) > 20 \text{ GeV}$ . Looser  $p_T$  cuts are applied in an attempt to increase our limited signal statistics. A forward jet is a signature of single top production, jets are therefore required to have  $|\eta| < 4.5$  in order to include these forward jets.

### 4.2.3 $b$ -tagging

The DL1r  $b$ -tagger [65] was used to identify jets as  $b$ -jets (See Section 3.2.6.4). Different DL1r working points are used to identify  $b$ -jets in our event selection (See Section 4.4). The working points are defined based off a cut on the DL1r score corresponding to a  $b$ -jet tagging efficiency of 60%, 70%, 77% and 85%.

Since this analysis is heavily statistically limited, the amount of statistics in our regions are aimed to be maximized. In an attempt to achieve this goal in the  $t\bar{t}Z$  CR,  $b$ -tagged jets were placed under *tight* and *loose* definitions. A tight  $b$ -tagged jet is defined as a jet which passes the 77%, 70%, 65% or 60% DL1r  $b$ -tagger working point. A loose  $b$ -tagged jet is defined as a jet which passes 85% DL1r  $b$ -tagger working point, but not the 77%, 70%, 65% or 60% DL1r  $b$ -tagger working points. Different numbers (and definitions) of tight and loose  $b$ -tagged jets were tried in each region, with the final selection criteria being chosen which maximised the expected significance of  $\sigma(tWZ)$  (See Section 4.4.1).

### 4.2.4 Overlap Removal Procedure

The overlap removal procedure is used on pre-selected leptons and jets. It is performed sequentially, in the following steps:

1. If the separation between a pre-selected electron and pre-selected muon is within  $\Delta R < 0.01$ , or they share a track, the pre-selected electron is discarded.
2. If the separation between a jet and a pre-selected electron is within  $\Delta R < 0.2$ , the jet is discarded.
3. Any remaining electron or muon closer than  $\Delta R = 0.4$  to a jet, is discarded.
4. If the distance between a jet and a pre-selected muon is  $\Delta R < 0.4$  and the jet has more than two associated tracks, then the muon is discarded, otherwise the jet is discarded.

## 4.3 Kinematic cuts

In order to suppress potential fakes and quarkonia (low mass resonances such as  $J/\psi$  and upsilon) a requirement that all OSSF lepton pairs have an invariant mass,  $m_{\text{OSSF}}$ , greater than 10 GeV is applied. The final state lepton charges must sum to zero. Therefore a requirement of  $\sum_{i=1}^4 \text{charge}(\ell_i) = 0$  is applied. The invariant mass of the OSSF lepton pair coming from the  $Z$  boson must equal the invariant mass of the  $Z$  boson, and noting that  $e,\mu$  reconstruction and identification in the ATLAS detector has a high efficiency [58], these OSSF leptons are used to reconstruct  $Z$  bosons with relatively high confidence. A  $Z$  candidate is defined in this analysis as an OSSF lepton pair with an invariant mass,  $m_{\text{OSSF}}$ , satisfying the condition,  $|m_{\text{OSSF}} - m_Z| < 30 \text{ GeV}$ , where  $m(Z)$  is the nominal  $Z$  boson mass (91.1876 GeV [48]). This wider mass window is used in order to cover the full range of the  $m(Z)$  distribution, in an attempt to increase the number of events which pass our baseline selections. Multiple  $Z$  candidates can be present in certain decay channels (e.g.  $eeee$ ,  $\mu\mu ee$ ,  $\mu\mu\mu\mu$ ). In these cases, the  $Z$  candidate which has an invariant mass closest to the nominal  $Z$  boson mass is chosen.

## 4.4 Regions and Event Selection

Two  $tWZ$  SRs are defined in an attempt to suppress and constrain the  $ZZ$  background. Both  $tWZ$  SRs are required to have exactly four tight leptons, exactly one  $Z$ -boson candidate, exactly one tight  $b$ -tagged jet (from the decay of the top quark) and greater than or equal to one jet. The two  $tWZ$  SR's differ by the flavours of their leptons which don't originate from the decay of a  $Z$ -boson (non- $Z$  leptons). The  $ZZ$  background has two  $Z$ -bosons which decay into a pair of OSSF lepton pairs, in order to mimic the  $tWZ$  signal. This is taken advantage of, to define a  $tWZ$  region enrich in  $ZZ$  background and one with a minimal  $ZZ$  background component. This is done by requiring that one of the  $tWZ$  SRs has its two non- $Z$  leptons to have opposite flavour and the other  $tWZ$  SR

Baseline selections				
$N_\ell = 4$ $p_T(\ell_1, \ell_2, \ell_3, \ell_4) > (28, 10, 10, 10)$ GeV $p_T(\text{jet}) > 20$ GeV, $ \eta(\text{jet})  < 4.5$ , $\text{jvt} > 0.5$ $ \eta(\ell_e)  < 2.47$ excluding $1.37 <  \eta(\ell_e)  < 1.52$ $ \eta(\ell_\mu)  < 2.5$ $\sum_{i=1}^4 \text{charge}(\ell_i) = 0$ All OSSF lepton pairs require $m_{\text{OSSF}} > 10$ GeV				
Regions				
$tWZ$ OF SR	$tWZ$ SF SR	$t\bar{t}Z$ CR	$ZZb$ CR	$(tWZ)_{\text{fake}}$ CR
$N_\ell(\text{tight}) = 4$	$N_\ell(\text{tight}) = 4$	$N_\ell(\text{tight}) = 4$	$N_\ell(\text{tight}) = 4$	$N_\ell(\text{tight}) = 3$ $N_\ell(\text{loose and NOT tight}) = 1$
$N_Z$ candidate = 1	$N_Z$ candidate = 1	$N_Z$ candidate = 1	$N_Z$ candidate = 2	$N_Z$ candidate = 1
$N_{\text{jet}} \geq 1$	$N_{\text{jet}} \geq 1$	$N_{\text{jet}} \geq 2$	$N_{\text{jet}} \geq 1$	$N_{\text{jet}} \geq 1$
$N_{\text{b-jet}}(\text{tight}) = 1$	$N_{\text{b-jet}}(\text{tight}) = 1$	$N_{\text{b-jet}}(\text{tight}) \geq 1$ $N_{\text{b-jet}}(\text{loose}) \geq 0$ $N_{\text{b-jet}}(\text{tight}) + N_{\text{b-jet}}(\text{loose}) = 2$	$N_{\text{b-jet}}(\text{tight}) = 1$	$N_{\text{b-jet}}(\text{tight}) = 1$
Opp. Flavour non-Z leptons	Same Flavour non-Z leptons	-	-	-

Table 4.3: A summary of the requirements applied for selecting events in the signal and control regions is shown.

is required to have its non- $Z$  leptons to have the same flavour. These two disjoint  $tWZ$  SRs are named  $tWZ$  OF SR and  $tWZ$  SF SR respectively. It is therefore expected that the  $tWZ$  SF SR contains the majority of the  $ZZ$  background events across both  $tWZ$  SRs.

In order to check the modelling of the most dominant background components in our signal region,  $t\bar{t}Z$  and  $ZZb$  control regions are defined. The  $t\bar{t}Z$  control region has the same requirement on the number of reconstructed  $Z$  boson candidates in the signal region (due to a commonality on the number of  $Z$  bosons present in both processes), however it is required that there are at least two jets and that exactly two of these jets are  $b$ -tagged (corresponding to the  $b$ -quark jets originating from the two top-quark decays). We choose to define a  $ZZb$  region, as opposed to a  $ZZ$  region, since the  $ZZ$  background present in the  $tWZ$  signal region contains exactly one  $b$ -tagged jet. Therefore defining a region with  $ZZ$  plus exactly one  $b$ -jet more closely resembles the  $ZZ$  background present in the signal region. In addition to this, mis-modelling of  $ZZ$  has been seen in other analyses [3, 36], further motivating the use of a  $ZZb$  control region over a  $ZZ$  CR. The  $ZZb$  CR requires exactly two  $Z$  boson candidates and exactly one  $b$ -tagged jet, resulting in an implicit requirement on the number of jets ( $N_{\text{jet}} \geq 1$ ).

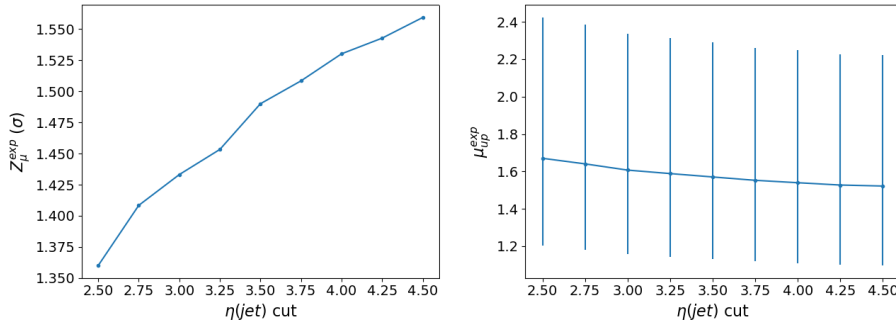
Fake leptons are objects reconstructed as leptons, but do not correspond to the leptons which we are interested in our analysis. Fake leptons can be split up into two main categories, irreducible (prompt) fakes and reducible (non-prompt) fakes. Irreducible fakes are true leptons which do not come from the process of interest. Reducible fakes are objects which are mis-identified or incorrectly reconstructed as leptons. In the ATLAS detector, the probability for a fake to occur is very low. In order to constrain the fake lepton component contained within the  $t\bar{t}Z$  sample, we define a  $(tWZ)_{\text{fake}}$  CR which is as similar as possible to the  $tWZ$  CR but is enhanced in fakes. This is achieved by defining the  $(tWZ)_{\text{fake}}$  CR to inherit the same selection criteria as the  $tWZ$  SRs however, in this case, we require exactly 3 tight leptons and exactly 1 loose (and NOT tight) lepton (since looser leptons are more likely to be fakes, compared to tighter leptons). A  $(t\bar{t}Z)_{\text{fake}}$  CR (requiring exactly 3 tight leptons and exactly 1 loose (and NOT tight) lepton) was tried as an alternative to the  $(tWZ)_{\text{fake}}$  CR, however a much larger suppression of fakes were observed in this region (compared to the  $(tWZ)_{\text{fake}}$  CR). This suppression of fakes can be explained by the extra  $b$ -tagged jet requirement (exactly two  $b$ -tagged jets are required in the  $t\bar{t}Z$  region, compared to exactly one in the  $tWZ$  SRs (See Table 4.3)) which causes suppression of fakes via the overlap removal procedure (See Section 4.2.4).

In Table 4.3, a summary of the final selection criteria and region definitions is shown.

#### 613 4.4.1 Optimization studies for event selection

614 In order to find the selection criteria for jets and leptons which maximized sensitivity to the  $tWZ$  signal, studies  
 615 were performed by plotting the expected significance ( $Z_\mu^{exp}$ ) and expected upper limit ( $\mu_{up}^{exp}$ ) for different selection  
 616 criteria. The fitting procedure as described in Section 4.10.1 was used to calculate the expected upper limits and  
 617 expected significances in this study (these metrics are fully described later in Section 4.10.1). The same selection  
 618 criteria and regions defined in Table 4.3 was used (unless otherwise specified), except for the selection(s) which  
 619 were being optimised in each case.

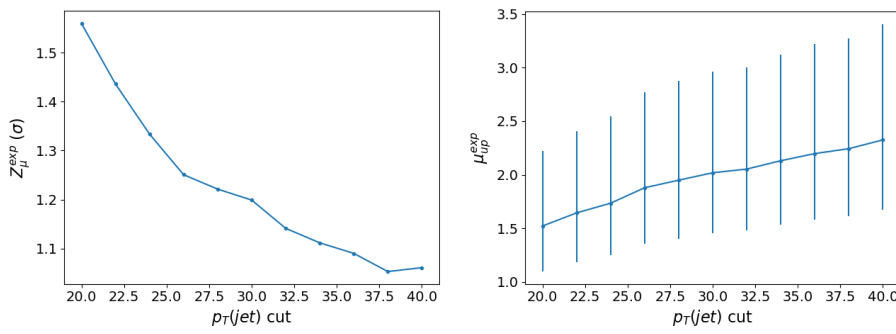
620  
 621 In Figure 4.1 the expected significance ( $Z_\mu^{exp}$ ) and expected upper limits ( $\mu_{up}^{exp}$ ) for different  $\eta(jet)$  cuts are shown.



622  
 623 Figure 4.1: **Left:** Expected significance ( $Z_\mu^{exp}$ ) for different  $\eta(jet)$  cuts is shown. The cuts applied on the  $\eta(jet)$   
 624 are shown on the x-axis and corresponding expected significance from the likelihood fit is shown on the y-axis.  
**Right:** Expected upper limit ( $\mu_{up}^{exp}$ ) for different  $\eta(jet)$  cuts is shown. The cuts applied on the  $\eta(jet)$  are shown  
 625 on the x-axis and corresponding expected upper limits are shown on the y-axis. Error bars representing the total  
 uncertainty on the expected upper limits are shown as vertical lines.

626 From Figure 4.1, we can see that the  $\eta(jet)$  cut which maximises the sensitivity of  $tWZ$  in the tetralepton channel  
 627 is requiring that  $\eta(jet) < 4.5$ . This selection criteria was set for the  $\eta(jet)$  across all regions.

628 In Figure 4.2 the expected significance ( $Z_\mu^{exp}$ ) and expected upper limits ( $\mu_{up}^{exp}$ ) for different  $p_T(jet)$  cuts are shown.



629 Figure 4.2: **Left:** Expected significance ( $Z_\mu^{exp}$ ) for different  $p_T(jet)$  cuts is shown. The cuts applied on the  $p_T(jet)$   
 630 are shown on the x-axis and corresponding expected significance from the likelihood fit is shown on the y-axis.  
**Right:** Expected upper limit ( $\mu_{up}^{exp}$ ) for different  $p_T(jet)$  cuts is shown. The cuts applied on the  $p_T(jet)$  are shown  
 631 on the x-axis and corresponding expected upper limits are shown on the y-axis. Error bars representing the total  
 632 uncertainty on the expected upper limits are shown as vertical lines.

633 From Figure 4.2, we can see that the  $p_T(jet)$  cut which maximises the sensitivity of  $tWZ$  is requiring that  
 634  $p_T(jet) > 20$  GeV. This selection criteria was set for the  $p_T(jet)$  across all regions.

635 In Figure 4.3 the expected significance ( $Z_\mu^{exp}$ ) and expected upper limits ( $\mu_{up}^{exp}$ ) for a range of different configurations  
 636 of DL1r  $b$ -tagged jet working points across different regions.

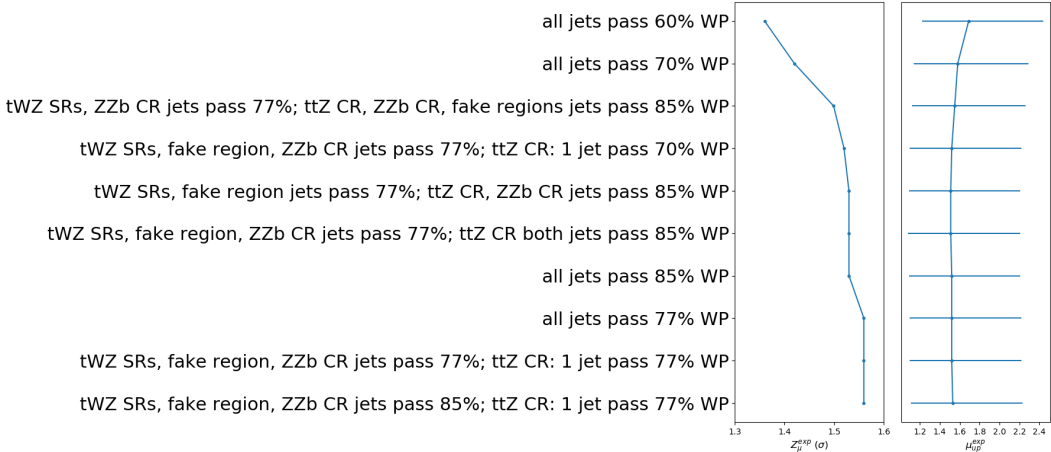


Figure 4.3: Expected significance ( $Z_\mu^{exp}$ ) and expected upper limit ( $\mu_{up}^{exp}$ ) for different configurations of DL1r  $b$ -tagged jet working points is shown. The common y-axis shows the different configurations of DL1r  $b$ -tagged jet working points. On the left panel, the expected significance from the likelihood fit is shown on the x-axis. On the right panel, the expected upper limit from the likelihood fit is shown on the x-axis (with the corresponding total uncertainty represented by horizontal lines).

633 From Figure 4.3, it can be seen that requiring that  $b$ -tagged jets pass the 77% DL1r WP in the  $tWZ$  SR, ( $tWZ$ )<sub>fake</sub>  
 634 CR and the  $ZZb$  CR and that at least one  $b$ -tagged jet in the  $ttZ$  SR passes the 77% DL1r WP (the other jet is  
 635 just required to pass the 85% DL1r WP) maximises the sensitivity overall (compared to the other investigated  
 636 configurations). This configuration was chosen  $b$ -tagged jets.

637 The  $p_T$ (L Lepton) is constrained by the single lepton triggers (Table ??). A cut was chosen to be applied on the  
 638  $p_T$ (NL Lepton) slightly tighter than the tightest single lepton  $p_T$  cut in the trigger. The  $p_T$ (NL Lepton) cut can  
 639 be optimized by comparing the expected significance and limit for a range of  $p_T$ (NL Lepton) cuts to determine the  
 640 cut which maximizes sensitivity.

641 In Figure 4.4 the expected significance ( $Z_\mu^{exp}$ ) and expected upper limits ( $\mu_{up}^{exp}$ ) for different  $p_T$ (NL Lepton) cuts is  
 642 shown.

643 Since there is a very small change between the different  $p_T$ (NL Lepton) cuts on the sensitivity of  $tWZ$ , we choose  
 644 to apply a  $p_T$ (NL Lepton) cut at 18 GeV (avoiding a  $p_T$  cut near the sharp drop in expected significance after  
 645 28 GeV), therefore applying a cut above the tightest, looser dilepton trigger  $p_T$  cut (17 GeV) to suppress any  
 646 systematic from the modelling of the trigger efficiency.

## 649 4.5 Signal and Control Regions

650 In this section, pre-fit distributions of variables in each region are shown. For each figure in this section, the data  
 651 is given by the black points and the MC predictions for each process are given by the histograms. The vertical  
 652 lines on the data points represent the statistical uncertainty in the data and the diagonally-lined bands represent  
 653 the total (statistical and systematic added in quadrature) uncertainty. The lower panel in each plot shows the  
 654 ratios of the data to the theoretical predictions. In order to suppress a bias towards large signal observations in  
 655 the development of the analysis, data has not been analysed in bins where the expected  $\frac{signal}{background}$  exceeds 0.1.  
 656 Blinded bins are shaded with black diagonal lines and their data points are omitted.

657 In Table 4.4, the pre-fit yields for each sample in each region is shown.  
 658 The statistical uncertainty associated with the number of raw MC events (weighted by MC event weights) can  
 659 be quantified by the Number of Equivalent Events [43],  $N_{equiv}$ , which relates the sample of  $N$  weighted events to  
 660  $N_{equiv}$  events with all MC event weights equal to 1, that would have the same relative statistical fluctuation.  $N_{equiv}$

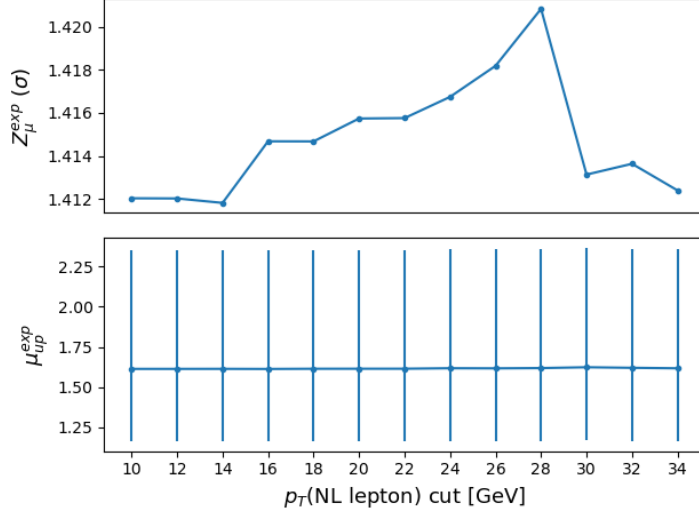


Figure 4.4: Expected significance ( $Z_\mu^{\text{exp}}$ ) and expected upper limit ( $\mu_{\text{up}}^{\text{exp}}$ ) for different  $p_T$ (NL Lepton) cuts is shown. The common x-axis shows cut applied to the  $p_T$  of the next-to-leading lepton. On the top panel, the expected significance from the likelihood fit is shown on the y-axis. On the bottom panel, the expected upper limit from the likelihood fit is shown on the y-axis (with the corresponding total uncertainty represented by vertical lines).

	$tWZ$ OF SR	$tWZ$ SF SR	$t\bar{t}Z$ CR	$ZZb$ CR	$(tWZ)_{\text{fake}}$ CR
$t\bar{t}Z$	$13.9325 \pm 1.84643$	$10.1343 \pm 1.36039$	$31.7149 \pm 4.46776$	$5.26303 \pm 0.696828$	$19.1224 \pm 2.50011$
$t\bar{t}Z$ fakes	$0.0687541 \pm 0.0482172$	$0.032827 \pm 0.026286$	$0.0709734 \pm 0.043509$	$0.0474576 \pm 0.0301512$	$4.94775 \pm 2.48939$
$tWZ$	$3.81359 \pm 0.392241$	$2.57584 \pm 0.326401$	$2.61991 \pm 0.861557$	$1.4023 \pm 0.156686$	$4.93485 \pm 0.692143$
$ZZ$	$0.546045 \pm 0.18975$	$8.76232 \pm 2.66871$	$1.22357 \pm 0.376889$	$46.0616 \pm 13.9203$	$7.76724 \pm 2.36894$
$t\bar{t}$	$6e-06 \pm 3.04506e-06$	$0.250783 \pm 0.44226$	$0.269883 \pm 0.223373$	$6e-06 \pm 3.04506e-06$	$2.36284 \pm 0.927828$
$tZq$	$0.0827265 \pm 0.0399222$	$0.0757694 \pm 0.0355101$	$0.0637132 \pm 0.0293762$	$0.0590199 \pm 0.0244576$	$4.91371 \pm 0.754695$
$t\bar{t}W$	$0.00674747 \pm 0.00793546$	$0.00279491 \pm 0.00287747$	$6e-06 \pm 3.04506e-06$	$0.00221727 \pm 0.00562041$	$0.944039 \pm 0.296854$
$WZ$	$0.0439316 \pm 0.0241635$	$0.0397876 \pm 0.0154764$	$0.0134837 \pm 0.0128327$	$0.0474188 \pm 0.0330635$	$1.84471 \pm 0.397076$
other	$0.000987429 \pm 0.000768187$	$0.00249801 \pm 0.00138007$	$0.0141085 \pm 0.00486102$	$6e-06 \pm 3.04506e-06$	$0.0100745 \pm 0.00367677$
$t\bar{t}\bar{t}$	$0.00934516 \pm 0.0080725$	$0.0107503 \pm 0.00852049$	$0.0570846 \pm 0.0206271$	$6e-06 \pm 3.04506e-06$	$0.0216609 \pm 0.00999533$
$t\bar{t}WW$	$0.0293456 \pm 0.0263573$	$0.0296011 \pm 0.0196075$	$0.26412 \pm 0.0936908$	$0.013096 \pm 0.0323943$	$0.151267 \pm 0.0593376$
$VVV(V = W/Z)$	$0.280384 \pm 0.0866421$	$0.191257 \pm 0.0595588$	$0.0696624 \pm 0.0228108$	$0.171171 \pm 0.0526519$	$0.265957 \pm 0.0821857$
$t\bar{t}H$	$0.854064 \pm 0.177974$	$0.674566 \pm 0.141771$	$1.98187 \pm 0.406211$	$0.151447 \pm 0.0357703$	$2.22981 \pm 0.45726$
Total	$19.6684 \pm 1.95158$	$22.7832 \pm 3.10338$	$38.3633 \pm 4.6342$	$53.2187 \pm 13.9618$	$49.5163 \pm 4.77745$
data	-	-	36	49	57

Table 4.4: The pre-fit yields for each sample in each region is shown.

can be written as,

$$N_{\text{equiv}} = \frac{(\sum_i^N w_i)^2}{\sum_i^N w_i^2} \quad (4.1)$$

where  $w_i$  is the MC event weight for event  $i$ . The standard uncertainty of  $N_{\text{equiv}}$  is given by  $u(N_{\text{equiv}}) = \sqrt{N_{\text{equiv}}}$ .

In Table 4.5, the number of equivalent events,  $N_{\text{equiv}}$  (and its percentage uncertainty), is shown for each sample in each region.  $N_{\text{equiv}}$  is relatively large, compared to the background processes, for the  $tWZ$  signal in all regions.

	$tWZ$ OF SR	$tWZ$ SF SR	$t\bar{t}Z$ CR	$ZZb$ CR	$(tWZ)_{\text{fake}}$ CR			
	$N_{\text{equiv}}$	Uncertainty [%]	$N_{\text{equiv}}$	Uncertainty [%]	$N_{\text{equiv}}$	Uncertainty [%]	$N_{\text{equiv}}$	Uncertainty [%]
$tWZ$	$6463.29 \pm 80.39$	1.24	$4153.0 \pm 64.44$	1.55	$4800.67 \pm 69.29$	1.44	$2497.07 \pm 49.97$	2.0
$t\bar{t}Z$	$1363.87 \pm 36.93$	2.71	$1031.04 \pm 32.11$	3.11	$3237.01 \pm 56.89$	1.76	$561.41 \pm 23.69$	4.22
$ZZ$	$50.89 \pm 7.13$	14.02	$975.61 \pm 31.23$	3.2	$267.85 \pm 16.37$	6.11	$7023.35 \pm 83.81$	1.19
other	$748.0 \pm 27.35$	3.66	$2.47 \pm 1.57$	63.58	$4.23 \pm 2.06$	48.6	$255.32 \pm 15.98$	6.26
$t\bar{t}Z$ fakes	$6.72 \pm 2.59$	38.56	$1.31 \pm 1.14$	87.34	$16.05 \pm 4.01$	24.96	$7.15 \pm 2.67$	37.41
Total	$8632.77 \pm 92.91$	1.08	$6163.44 \pm 78.51$	1.27	$8325.81 \pm 91.25$	1.1	$10344.3 \pm 101.71$	0.98
							$12044.27 \pm 109.75$	0.91

Table 4.5: The number of equivalent events,  $N_{\text{equiv}}$  (and its percentage uncertainty), is shown for each sample in each region.

666 This tells us that we have a large number of raw MC events for the  $tWZ$  sample. An extended  $tWZ$  sample was  
 667 generated to increase the number of signal events used to train the event-level BDT (See Section 4.7.2).

### 668 4.5.1 $tWZ$ OF SR

669 In this section, pre-fit distributions of variables in the  $tWZ$  OF SR are shown.

670

671 In Figure 4.5 MC predictions for  $p_T$ ,  $\eta$  and  $\phi$  for leading (L) leptons and next-to-leading (NL) leptons in the  $tWZ$   
 672 OF SR region is shown.

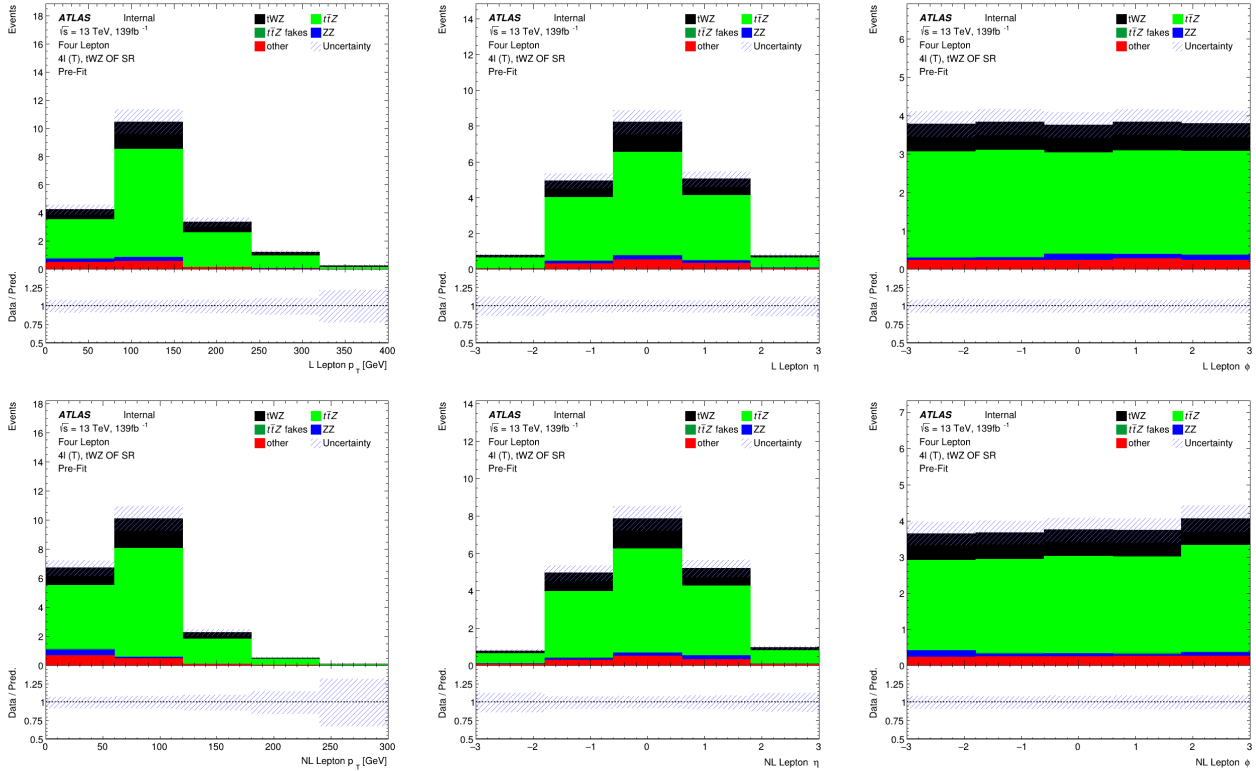


Figure 4.5: MC predictions for  $p_T$ ,  $\eta$  and  $\phi$  for leading (L) leptons (top row) and next-to-leading (NL) leptons (bottom row) in the  $tWZ$  OF SR region is shown.

673 In Figure 4.6 MC predictions for  $p_T$ ,  $\eta$  and  $\phi$  for leading (L) jets and next-to-leading (NL) jets in the  $tWZ$  OF SR  
 674 region is shown.

675 In Figure 4.7 MC predictions for  $p_T$ ,  $\eta$  and  $\phi$  of the next-to-next-to-leading (NNL) jets,  $H_T$  (scalar sum of Jet  $p_T$ )  
 676 and the Number of jets in the  $tWZ$  OF SR region is shown.

677 In Figure 4.8 MC predictions for  $p_T$ ,  $\eta$  and  $\phi$  of the leading b-tagged jets, the scalar sum of b-tagged jet  $p_T$  and  
 678 the Number of b-tagged jets in the  $tWZ$  OF SR region is shown.

### 679 4.5.2 $tWZ$ SF SR

680 In this section, pre-fit distributions of variables in the  $tWZ$  SF SR are shown.

681

682 In Figure 4.9 MC predictions for  $p_T$ ,  $\eta$  and  $\phi$  for leading (L) leptons and next-to-leading (NL) leptons in the  $tWZ$   
 683 SF SR region is shown.

684 In Figure 4.10 MC predictions for  $p_T$ ,  $\eta$  and  $\phi$  for leading (L) jets and next-to-leading (NL) jets in the  $tWZ$  SF SR  
 685 region is shown.

686 In Figure 4.11 MC predictions for  $p_T$ ,  $\eta$  and  $\phi$  of the next-to-next-to-leading (NNL) jets,  $H_T$  (scalar sum of Jet  $p_T$ )  
 687 and the Number of jets in the  $tWZ$  SF SR region is shown.

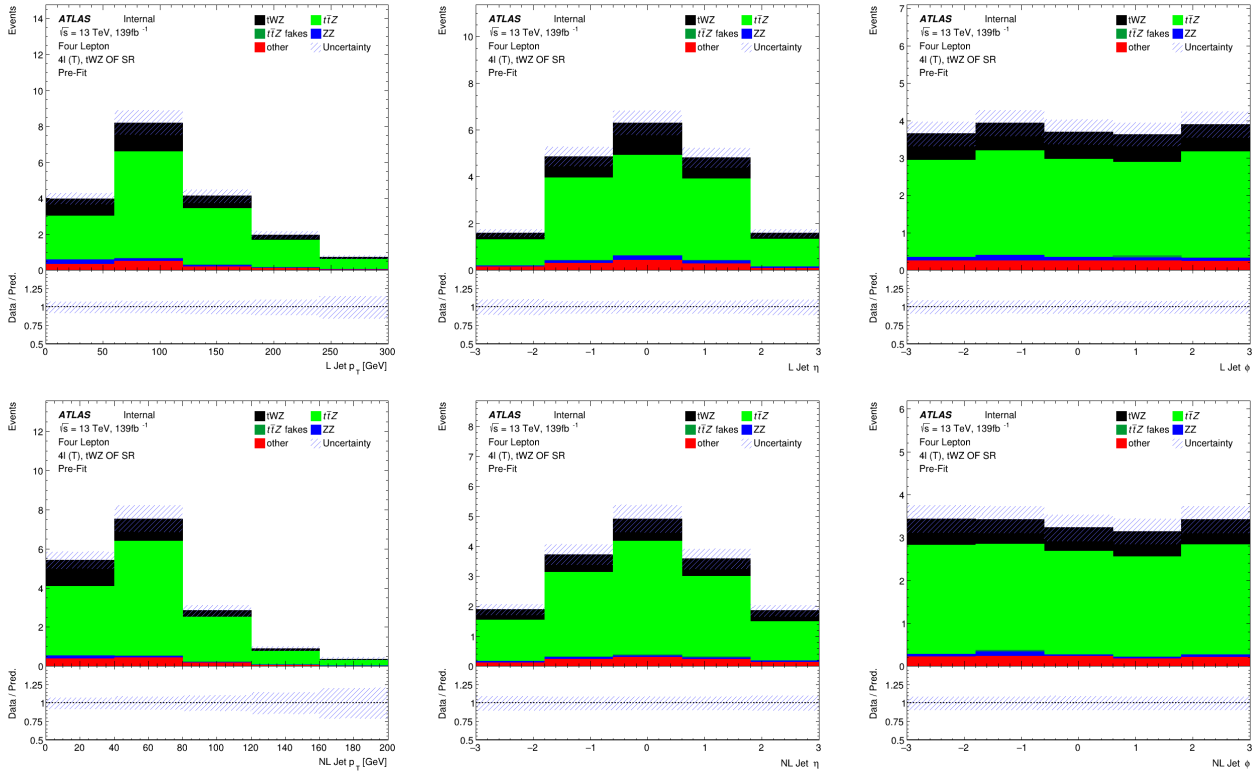


Figure 4.6: MC predictions for  $p_T$ ,  $\eta$  and  $\phi$  for leading (L) jets (top row) and next-to-leading (NL) jets (bottom row) in the  $tWZ$  OF SR region is shown.

688 In Figure 4.12 MC predictions for  $p_T$ ,  $\eta$  and  $\phi$  of the leading b-tagged jets, the scalar sum of b-tagged jet  $p_T$  and  
689 the Number of b-tagged jets in the  $tWZ$  SF SR region is shown.

### 690 4.5.3 $t\bar{t}Z$ CR

691 In this section, pre-fit distributions of variables in the  $t\bar{t}Z$  CR are shown.

692 In Figure 4.13 MC predictions for  $p_T$ ,  $\eta$  and  $\phi$  for leading (L) leptons and next-to-leading (NL) leptons in the  $t\bar{t}Z$   
693 CR region is shown.

694 In Figure 4.14 MC predictions for  $p_T$ ,  $\eta$  and  $\phi$  for leading (L) jets and next-to-leading (NL) jets in the  $t\bar{t}Z$  CR  
695 region is shown.

696 In Figure 4.15 MC predictions for  $p_T$ ,  $\eta$  and  $\phi$  of the next-to-next-to-leading (NNL) jets,  $H_T$  (scalar sum of Jet  $p_T$ )  
697 and the Number of jets in the  $t\bar{t}Z$  CR region is shown.

698 In Figure 4.16 MC predictions for  $p_T$ ,  $\eta$  and  $\phi$  of the leading b-tagged jets, the scalar sum of b-tagged jet  $p_T$  and  
699 the Number of b-tagged jets in the  $t\bar{t}Z$  CR region is shown.

### 700 4.5.4 $ZZb$ CR

701 In this section, pre-fit distributions of variables in the  $ZZb$  CR are shown.

702 In Figure 4.17 MC predictions for  $p_T$ ,  $\eta$  and  $\phi$  for leading (L) leptons and next-to-leading (NL) leptons in the  $ZZb$   
703 CR region is shown.

704 In Figure 4.18 MC predictions for  $p_T$ ,  $\eta$  and  $\phi$  for leading (L) jets and next-to-leading (NL) jets in the  $ZZb$  CR  
705 region is shown.

706 In Figure 4.19 MC predictions for  $p_T$ ,  $\eta$  and  $\phi$  of the next-to-next-to-leading (NNL) jets,  $H_T$  (scalar sum of Jet  $p_T$ )  
707 and the Number of jets in the  $ZZb$  CR region is shown.

708 In Figure 4.20 MC predictions for  $p_T$ ,  $\eta$  and  $\phi$  of the leading b-tagged jets, the scalar sum of b-tagged jet  $p_T$  and  
709 the Number of b-tagged jets in the  $ZZb$  CR region is shown.

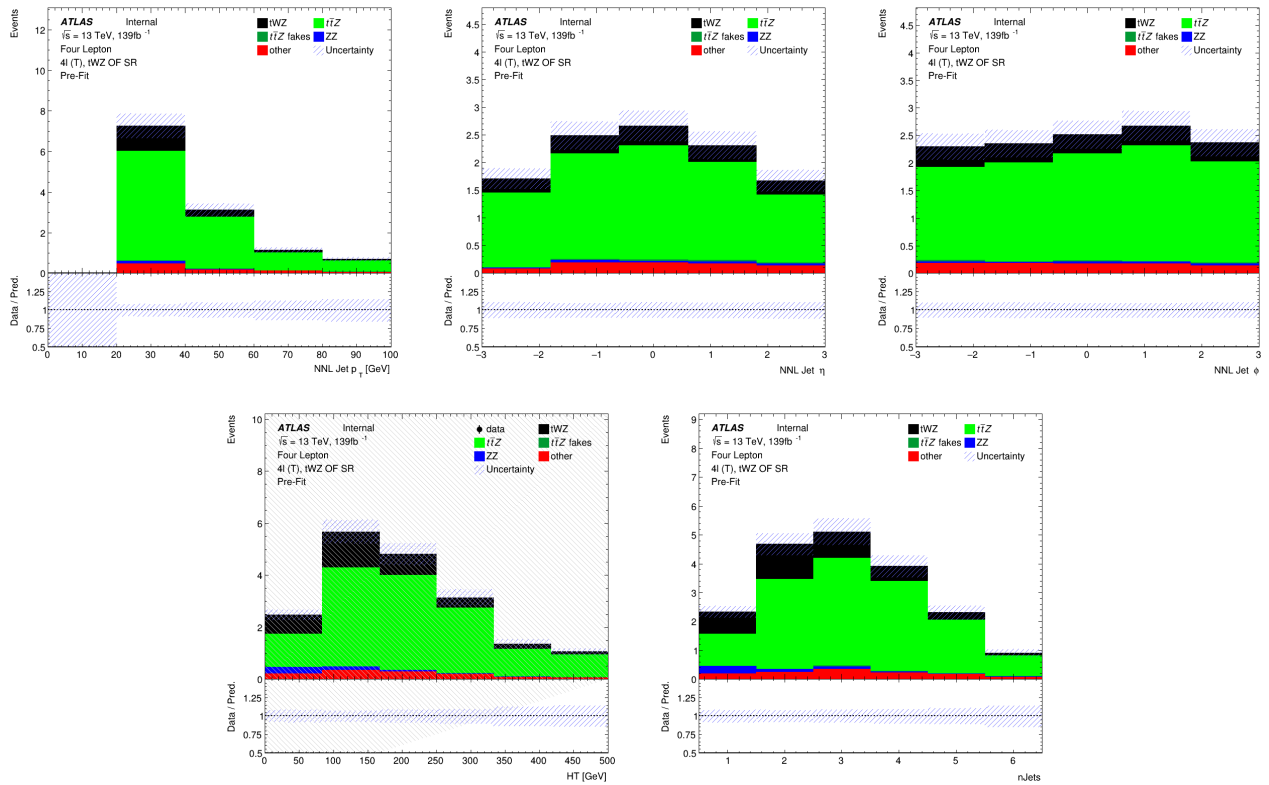


**Figure 4.7: Top row:** MC predictions for  $p_T$ ,  $\eta$  and  $\phi$  for next-to-next-to-leading (NNL) jets in the  $tWZ$  OF SR region is shown. **Bottom row:** MC predictions for  $H_T$  (scalar sum of Jet  $p_T$ ) (left) and the Number of jets (right) in the  $tWZ$  OF SR region is shown.

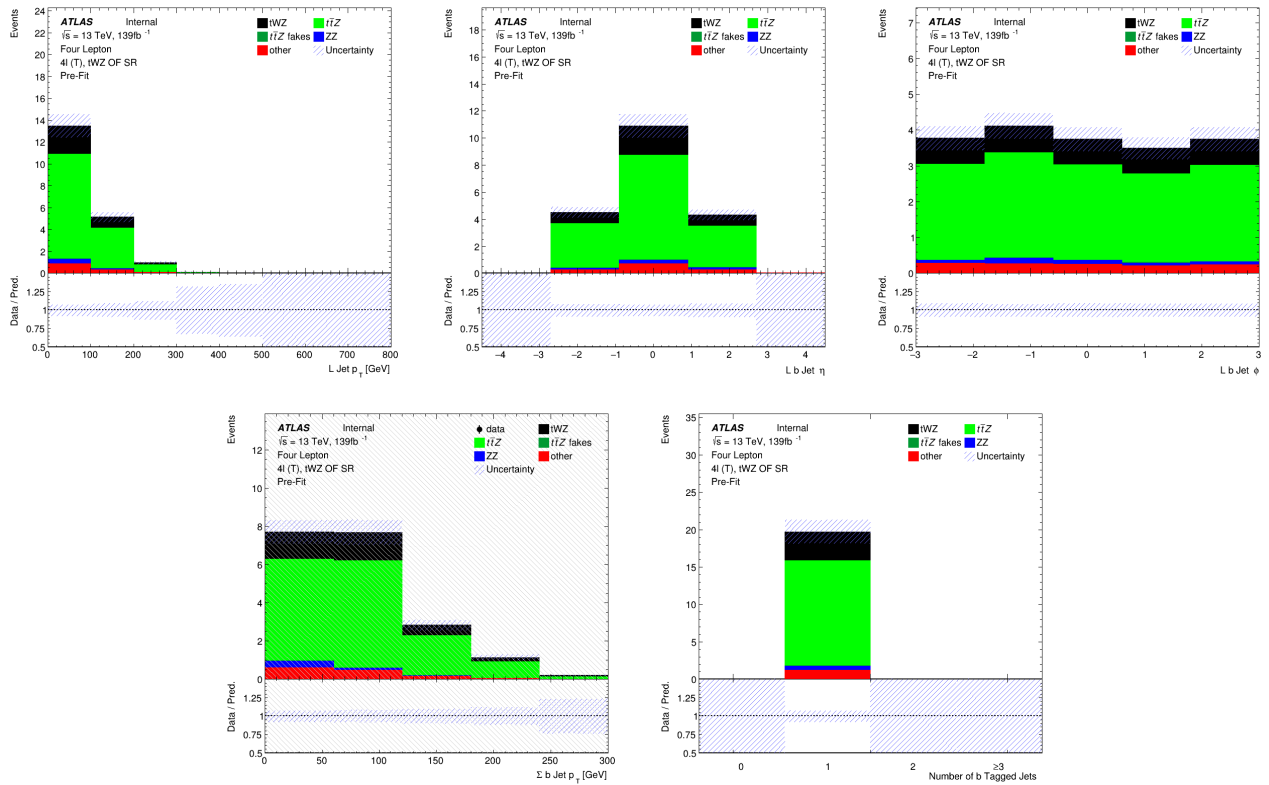


**Figure 4.8:** **Top row:** MC predictions for  $p_T$ ,  $\eta$  and  $\phi$  for leading b-tagged jets in the  $tWZ$  OF SR region is shown. **Bottom row:** MC predictions for the scalar sum of b-tagged jet  $p_T$  (left) and the Number of b-tagged jets (right) in the  $tWZ$  OF SR region is shown.

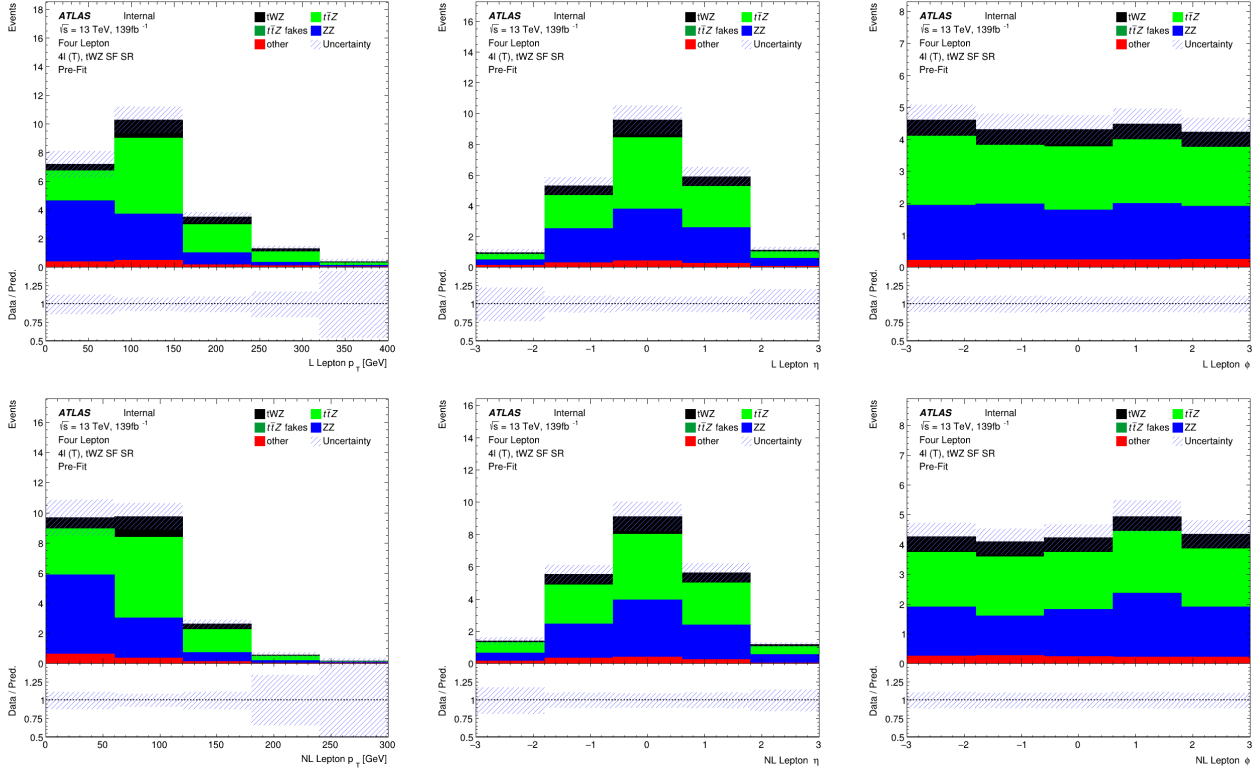


Figure 4.9: MC predictions for  $p_T$ ,  $\eta$  and  $\phi$  for leading (L) leptons (top row) and next-to-leading (NL) leptons (bottom row) in the  $tWZ$  SF SR region is shown.

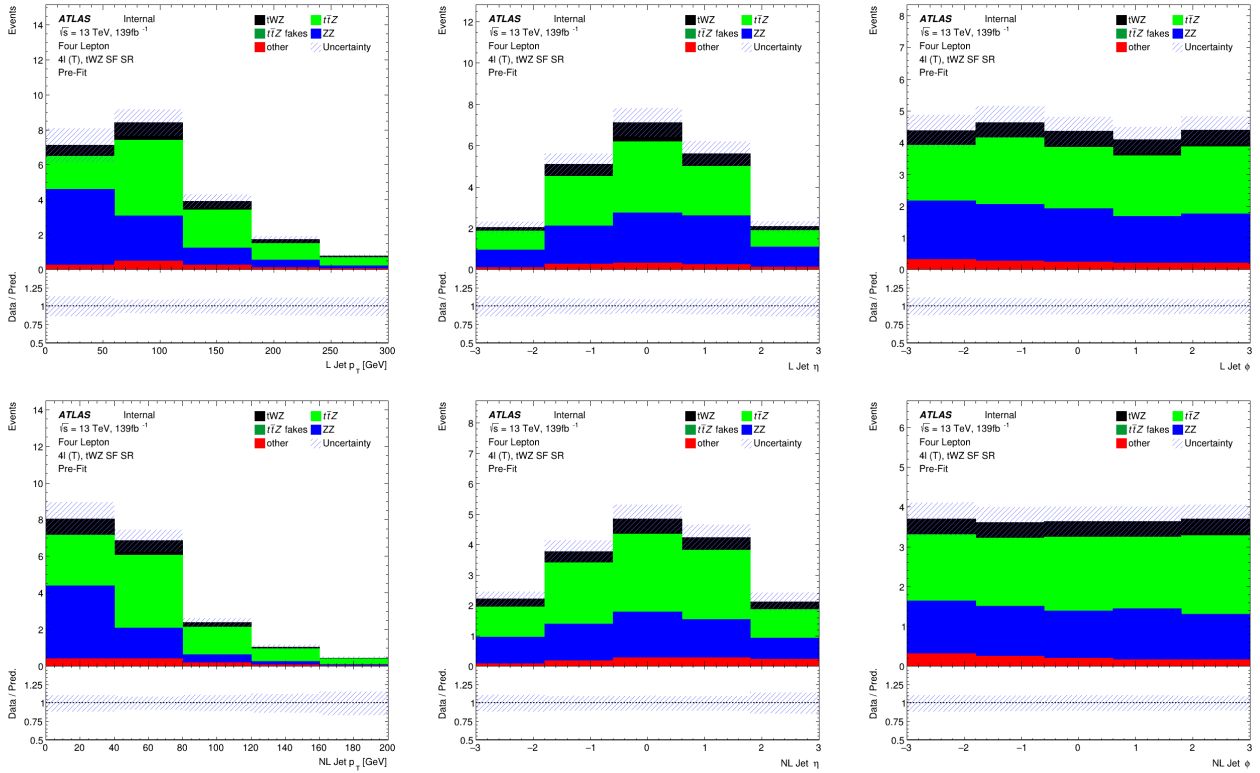
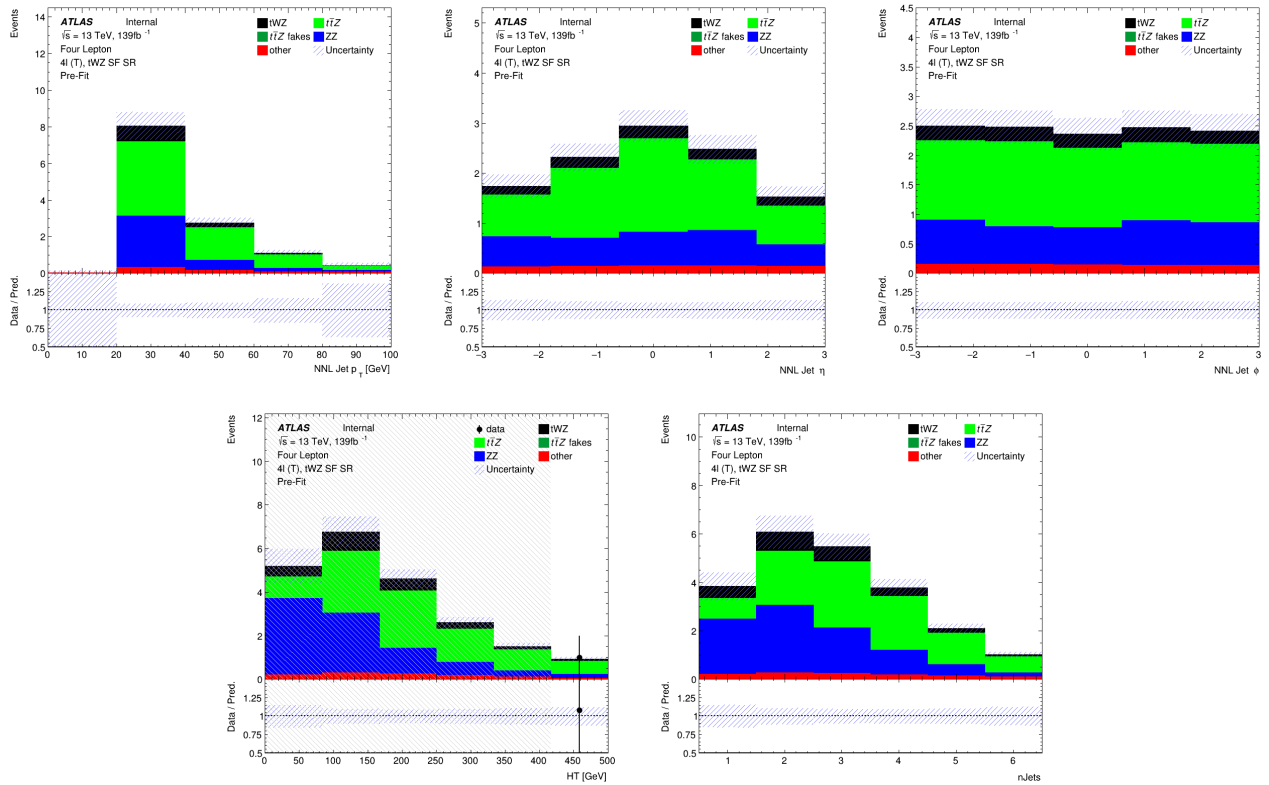


Figure 4.10: MC predictions for  $p_T$ ,  $\eta$  and  $\phi$  for leading (L) jets (top row) and next-to-leading (NL) jets (bottom row) in the  $tWZ$  SF SR region is shown.



**Figure 4.11:** **Top row:** MC predictions for  $p_T$ ,  $\eta$  and  $\phi$  for next-to-next-to-leading (NNL) jets in the  $tWZ$  SF SR region is shown. **Bottom row:** MC predictions for  $H_T$  (scalar sum of Jet  $p_T$ ) (left) and the Number of jets (right) in the  $tWZ$  SF SR region is shown.

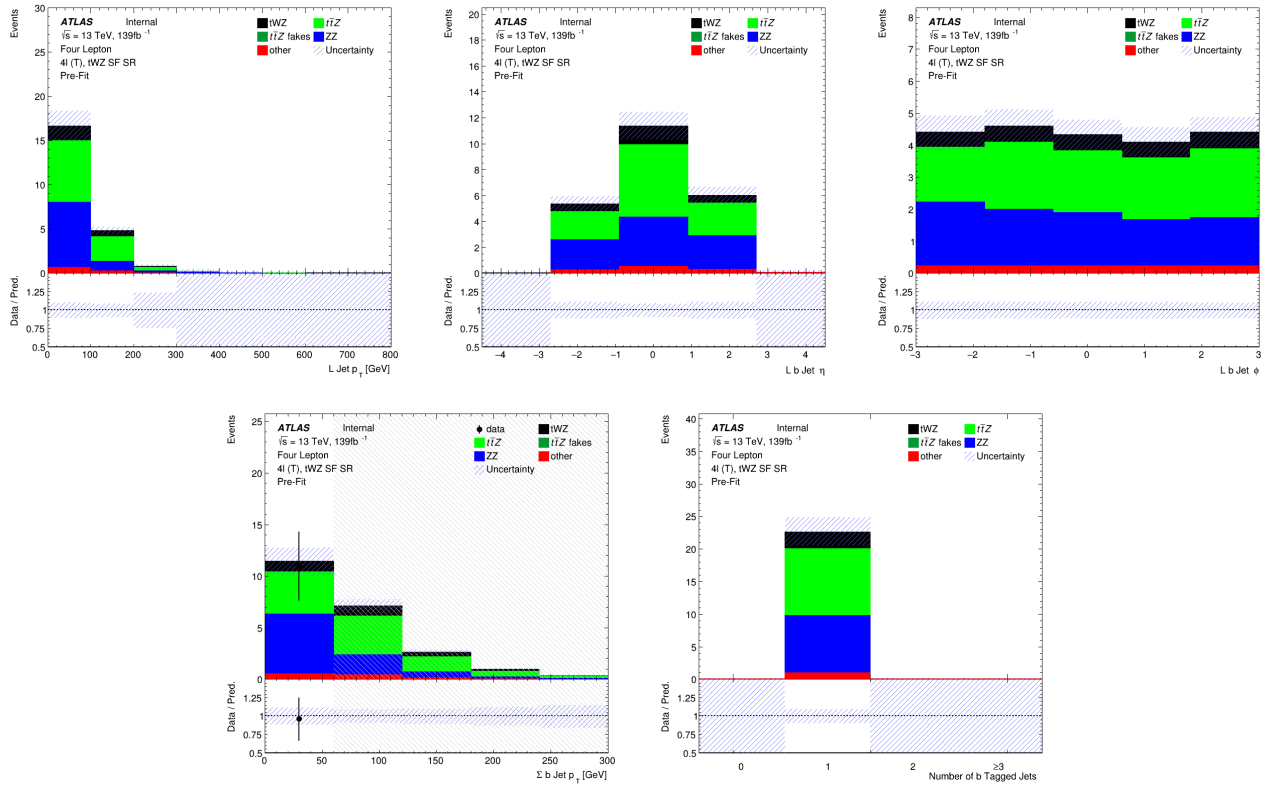


Figure 4.12: **Top row:** MC predictions for  $p_T$ ,  $\eta$  and  $\phi$  for leading b-tagged jets in the  $tWZ$  SF SR region is shown. **Bottom row:** MC predictions for the scalar sum of b-tagged jet  $p_T$  (left) and the Number of b-tagged jets (right) in the  $tWZ$  SF SR region is shown.

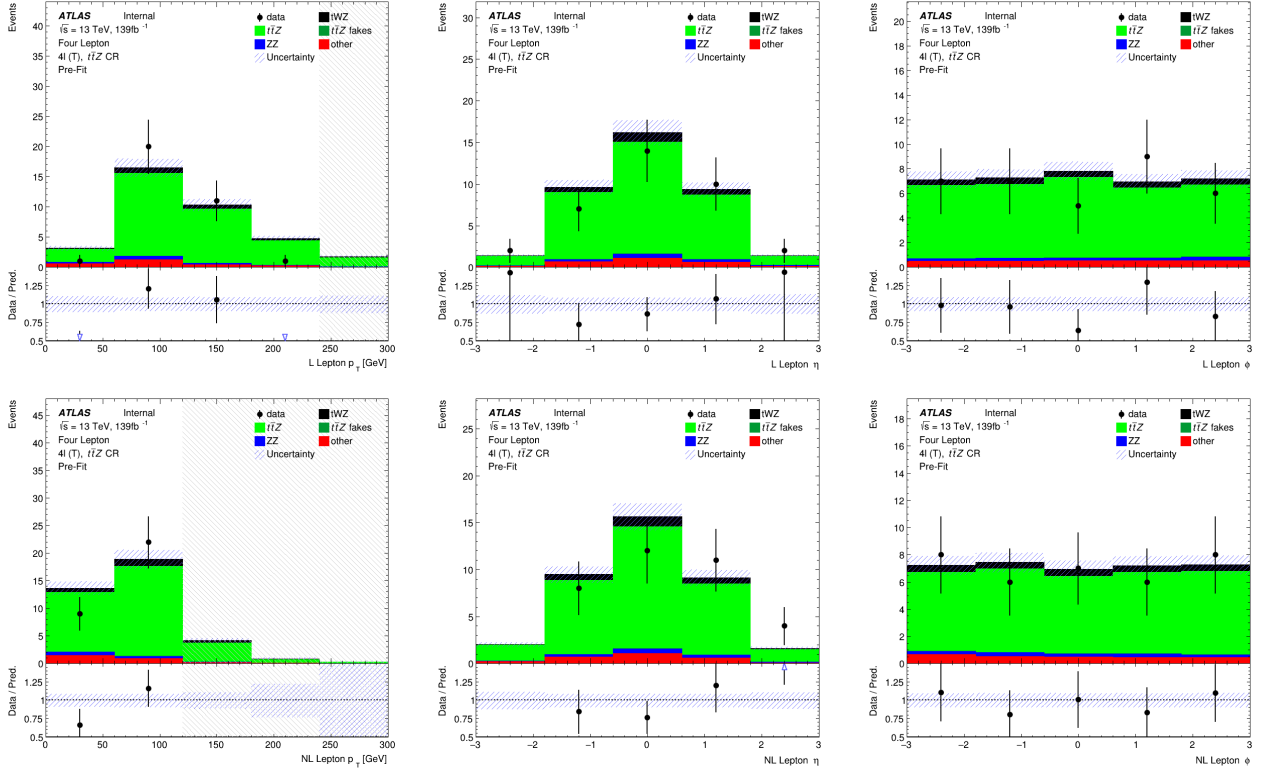


Figure 4.13: MC predictions for  $p_T$ ,  $\eta$  and  $\phi$  for leading (L) leptons (top row) and next-to-leading (NL) leptons (bottom row) in the  $t\bar{t}Z$  CR region is shown.

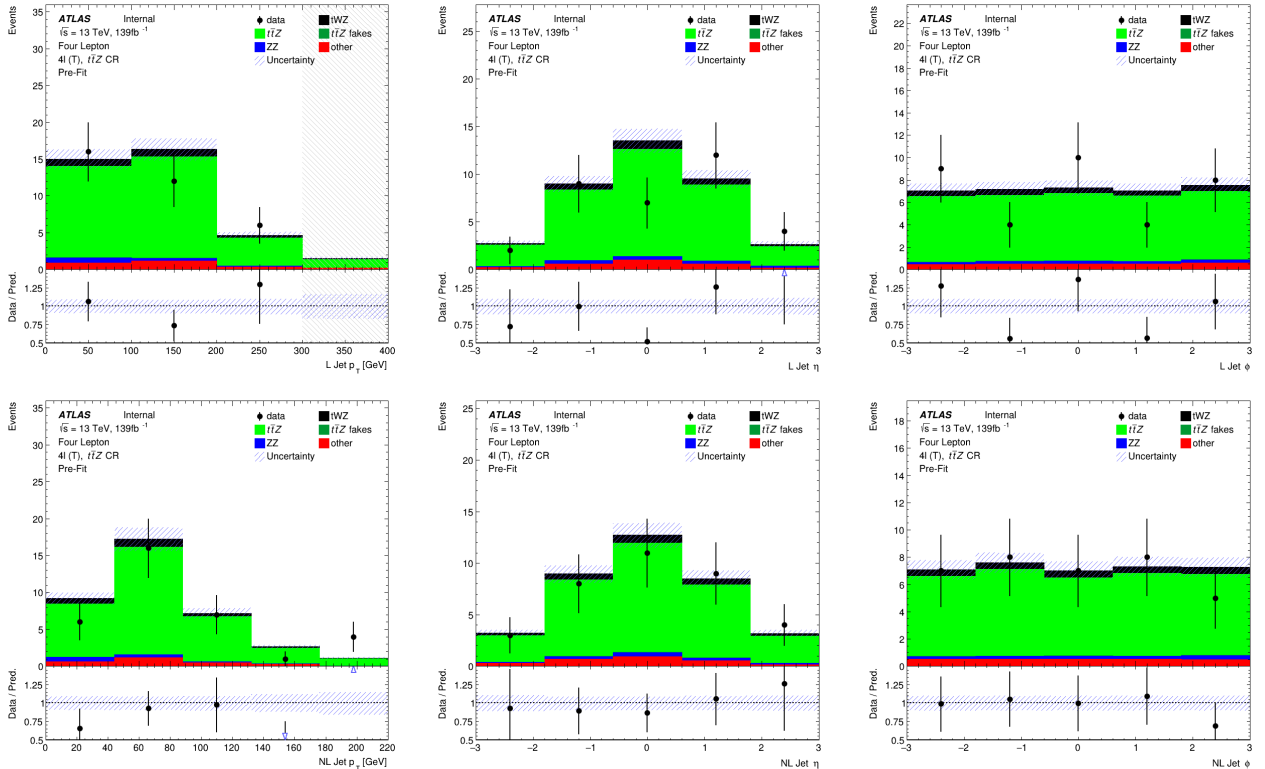


Figure 4.14: MC predictions for  $p_T$ ,  $\eta$  and  $\phi$  for leading (L) jets (top row) and next-to-leading (NL) jets (bottom row) in the  $t\bar{t}Z$  CR region is shown.

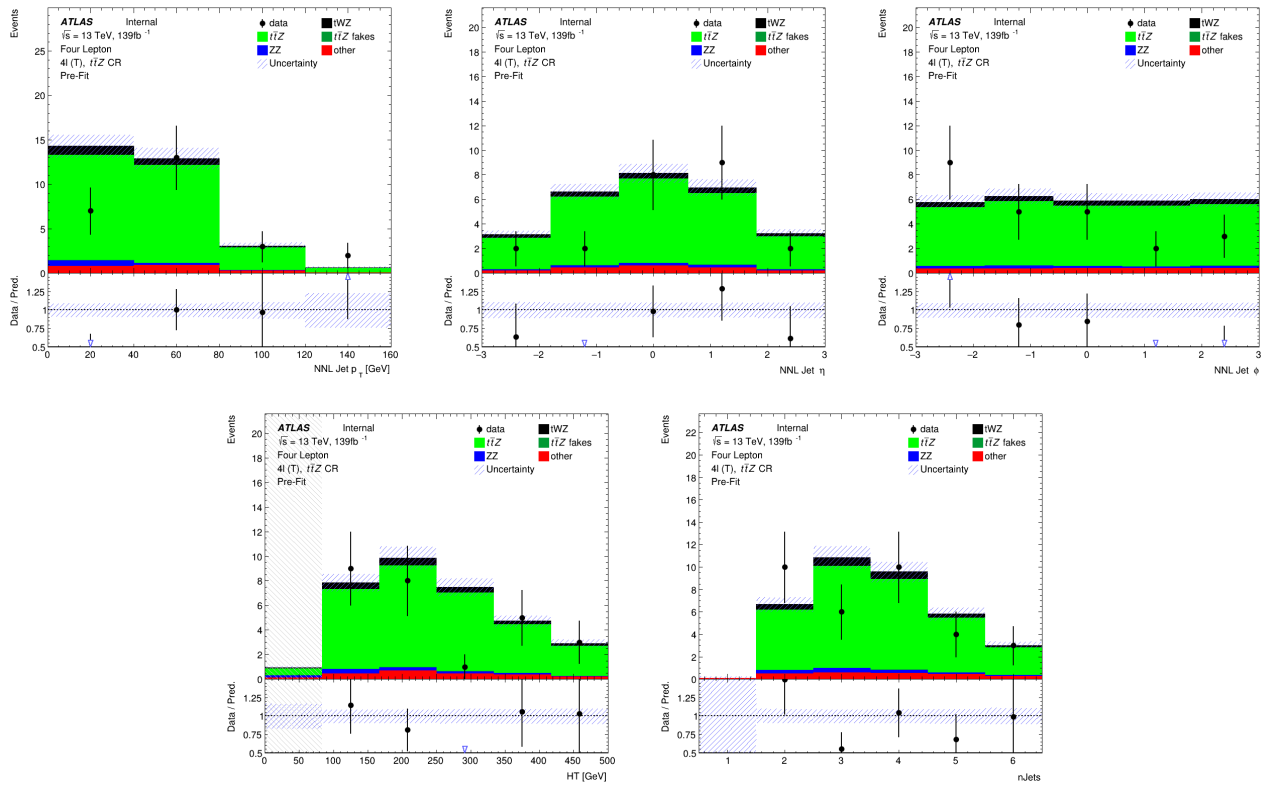
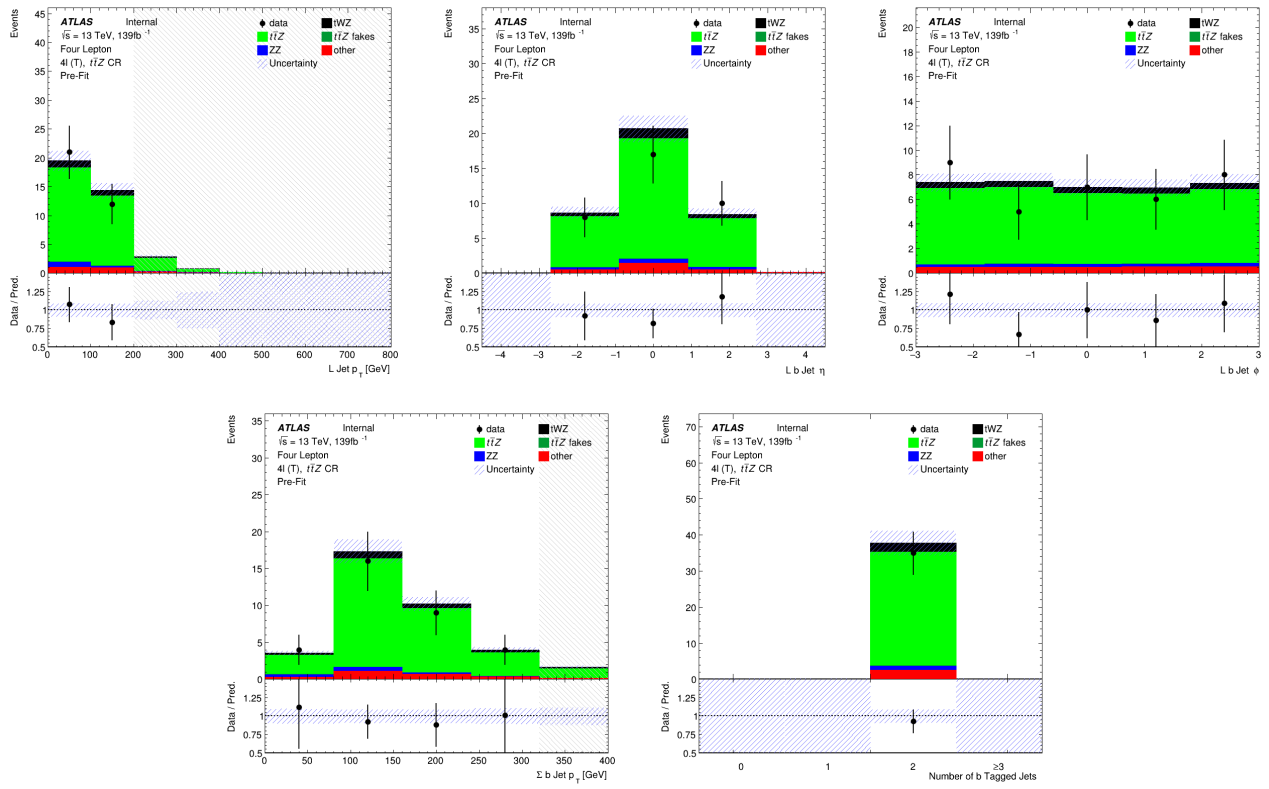


Figure 4.15: **Top row:** MC predictions for  $p_T$ ,  $\eta$  and  $\phi$  for next-to-next-to-leading (NNL) jets in the  $t\bar{t}Z$  CR region is shown. **Bottom row:** MC predictions for  $H_T$  (scalar sum of Jet  $p_T$ ) (left) and the Number of jets (right) in the  $t\bar{t}Z$  CR region is shown.



**Figure 4.16:** **Top row:** MC predictions for  $p_T$ ,  $\eta$  and  $\phi$  for leading b-tagged jets in the  $t\bar{t}Z$  CR region is shown. **Bottom row:** MC predictions for the scalar sum of b-tagged jet  $p_T$  (left) and the Number of b-tagged jets (right) in the  $t\bar{t}Z$  CR region is shown.

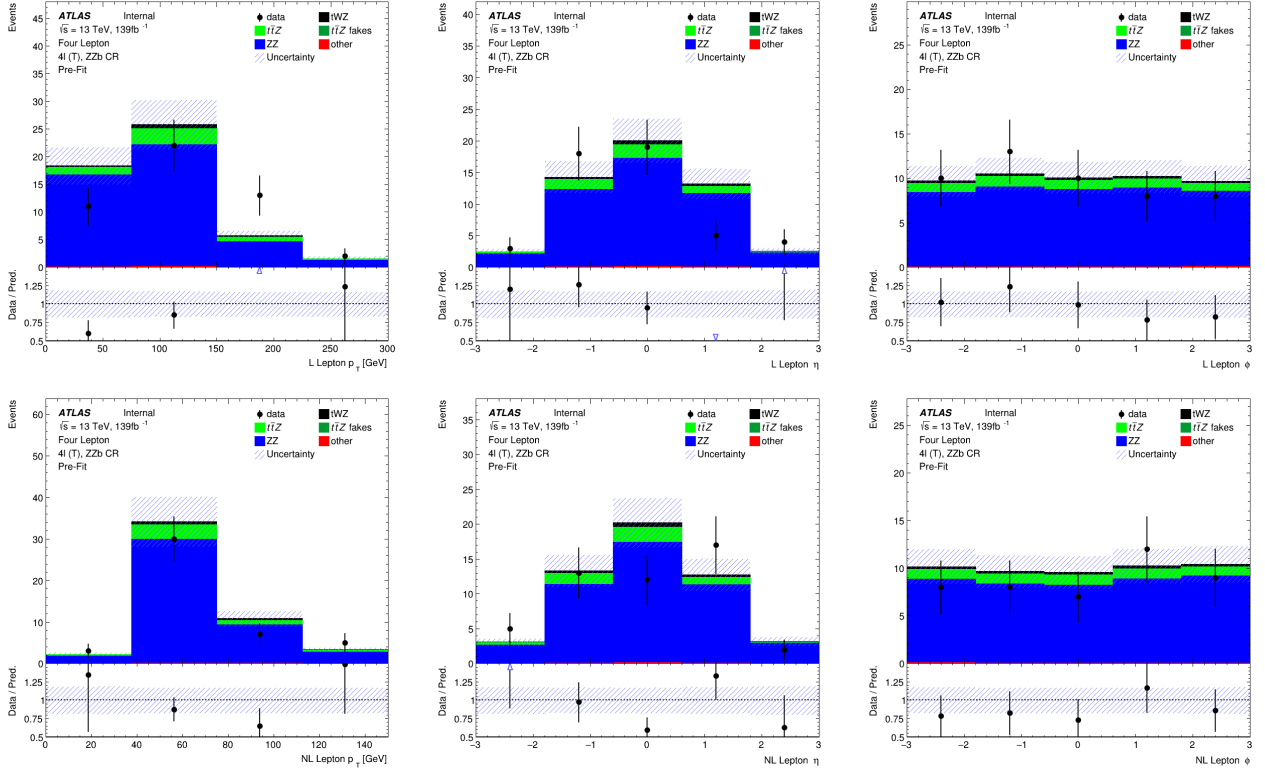


Figure 4.17: MC predictions for  $p_T$ ,  $\eta$  and  $\phi$  for leading (L) leptons (top row) and next-to-leading (NL) leptons (bottom row) in the  $ZZb$  CR region is shown.

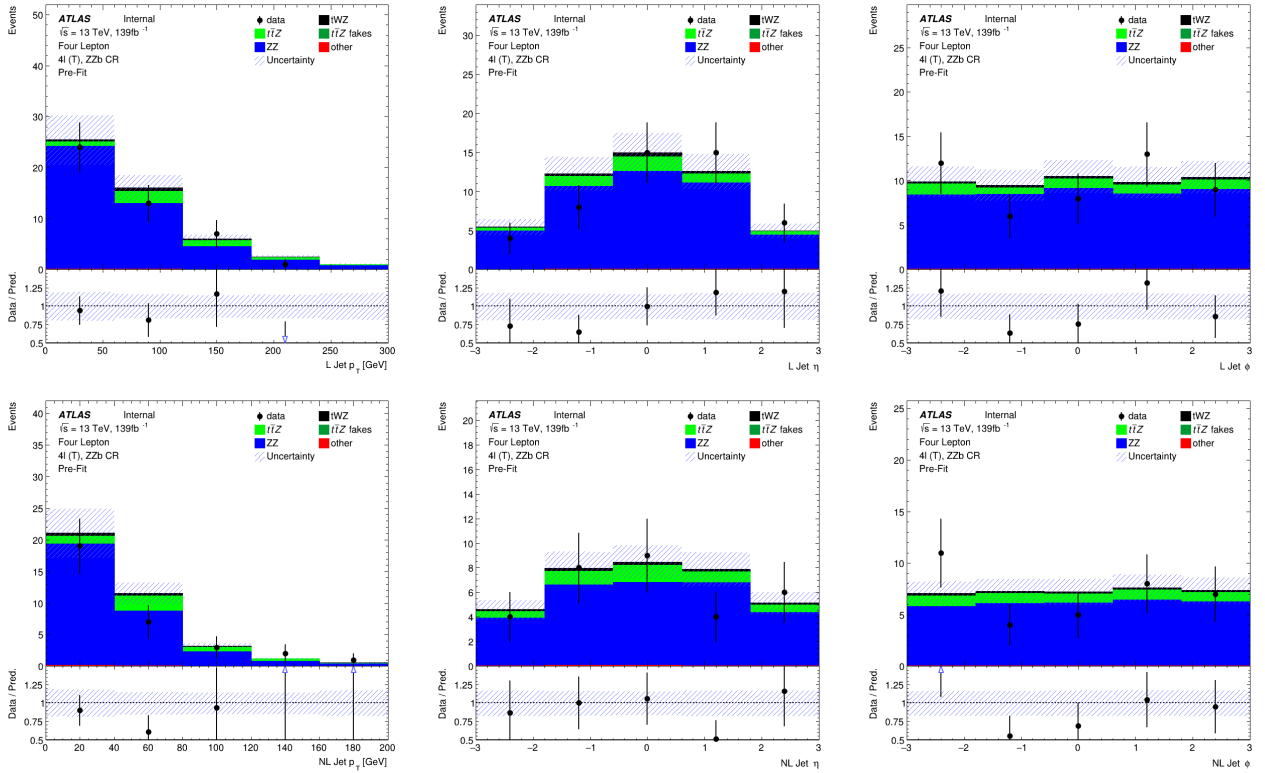


Figure 4.18: MC predictions for  $p_T$ ,  $\eta$  and  $\phi$  for leading (L) jets (top row) and next-to-leading (NL) jets (bottom row) in the  $ZZb$  CR region is shown.

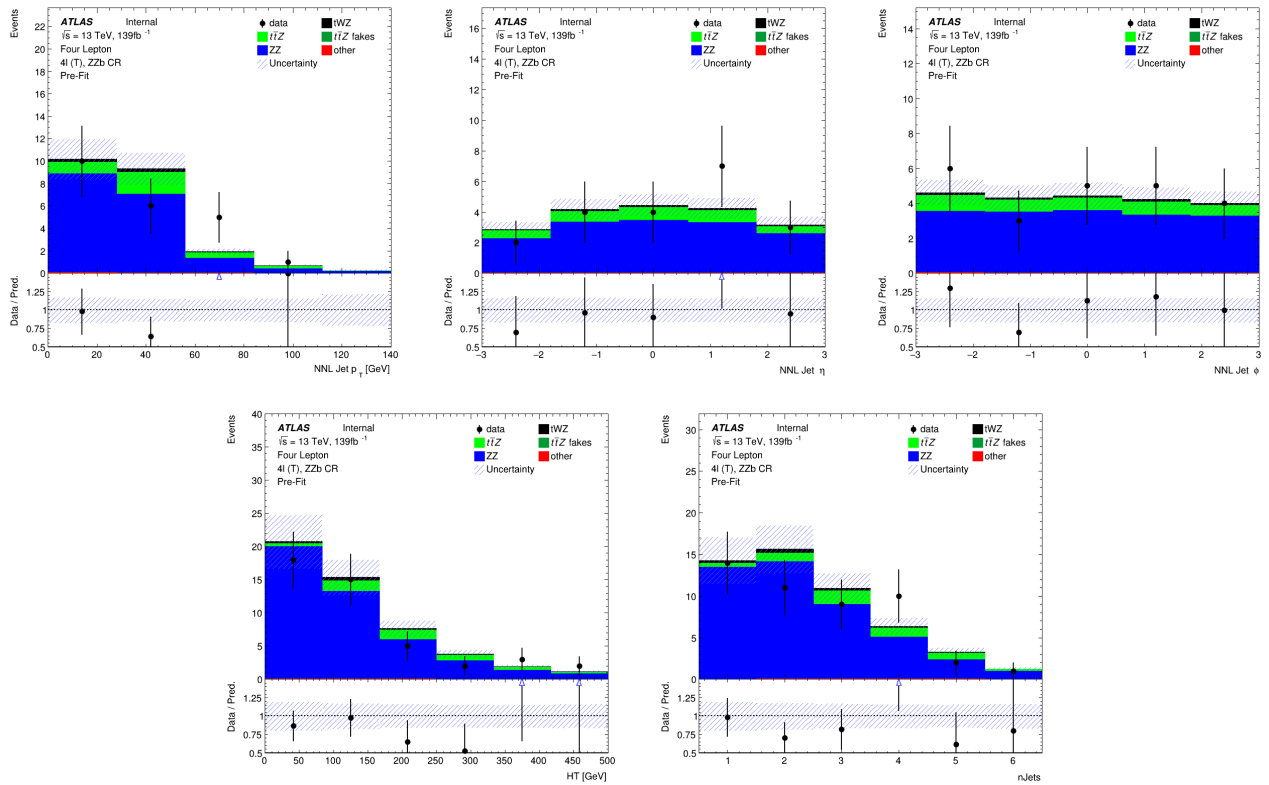


Figure 4.19: **Top row:** MC predictions for  $p_T$ ,  $\eta$  and  $\phi$  for next-to-next-to-leading (NNL) jets in the  $ZZb$  CR region is shown. **Bottom row:** MC predictions for  $H_T$  (scalar sum of Jet  $p_T$ ) (left) and the Number of jets (right) in the  $ZZb$  CR region is shown.

the Number of b-tagged jets in the  $ZZb$  CR region is shown.

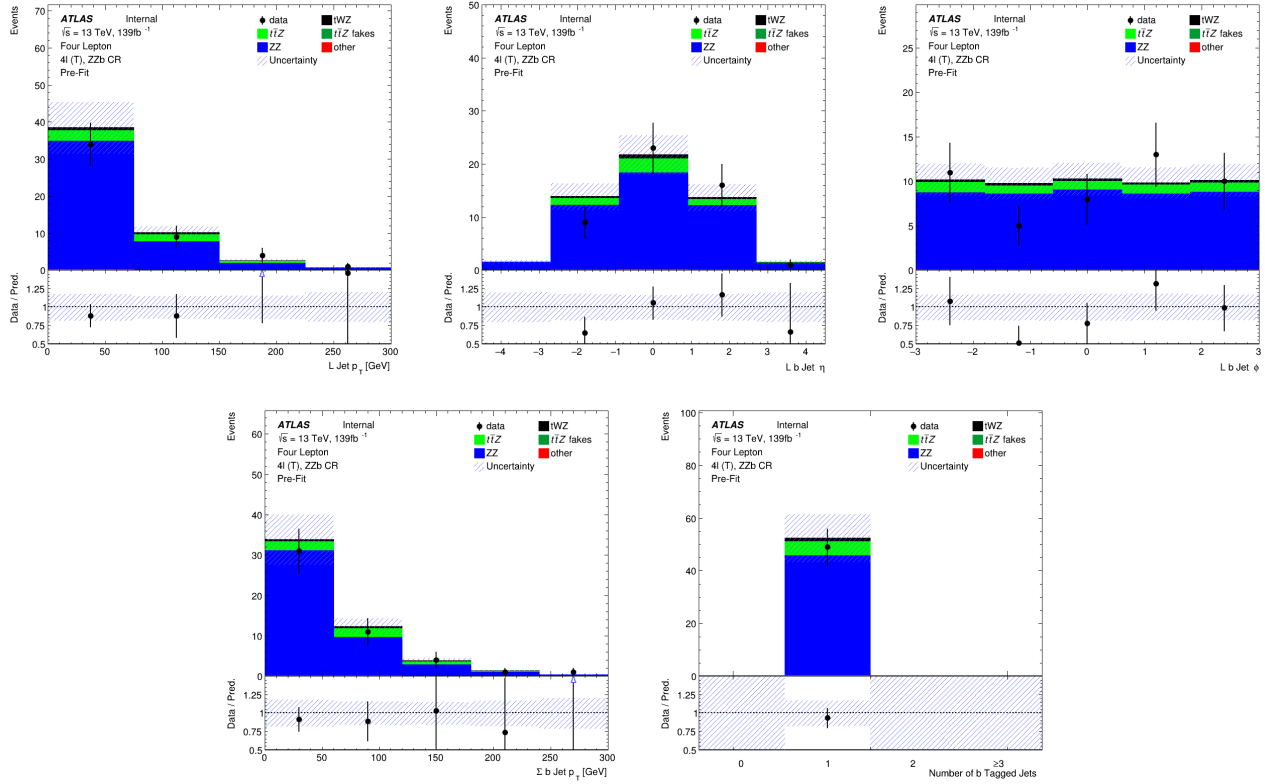


Figure 4.20: **Top row:** MC predictions for  $p_T$ ,  $\eta$  and  $\phi$  for leading b-tagged jets in the  $ZZb$  CR region is shown. **Bottom row:** MC predictions for the scalar sum of b-tagged jet  $p_T$  (left) and the Number of b-tagged jets (right) in the  $ZZb$  CR region is shown.

711

#### 712 4.5.5 $(tWZ)_{\text{fake}}$ CR

713 In this section, pre-fit distributions of variables in the  $(tWZ)_{\text{fake}}$  CR are shown.

714

715 In Figure 4.21 MC predictions for  $p_T$ ,  $\eta$  and  $\phi$  for leading (L) leptons and next-to-leading (NL) leptons in the  
716  $(tWZ)_{\text{fake}}$  CR region is shown.

717 In Figure 4.22 MC predictions for  $p_T$ ,  $\eta$  and  $\phi$  for leading (L) jets and next-to-leading (NL) jets in the  $(tWZ)_{\text{fake}}$   
718 CR region is shown.

719 In Figure 4.23 MC predictions for  $p_T$ ,  $\eta$  and  $\phi$  of the next-to-next-to-leading (NNL) jets,  $H_T$  (scalar sum of Jet  $p_T$ )  
720 and the Number of jets in the  $(tWZ)_{\text{fake}}$  CR region is shown.

721 In Figure 4.24 MC predictions for  $p_T$ ,  $\eta$  and  $\phi$  of the leading b-tagged jets, the scalar sum of b-tagged jet  $p_T$  and  
722 the Number of b-tagged jets in the  $(tWZ)_{\text{fake}}$  CR region is shown.

723 Given the limited statistics which we are presented with in the tetralepton channel, we nevertheless observe relatively  
724 good agreement overall between data and MC.

## 725 4.6 Fake Lepton Estimation

726 We aim to estimate the fake lepton contribution in this analysis. We start off by noticing that  $t\bar{t}Z$  is our most  
727 dominant background ( $\sim 75\%$  of the total background contribution) and will therefore have the largest fake  
728 component compared to all other samples considered in the analysis. The fake lepton efficiency,  $\epsilon$ , can be written  
729 as  $\epsilon = \frac{N_{\text{fake}}^{\text{tight}}}{N_{\text{fake}}^{\text{loose}}}$ , where  $N_{\text{fake}}^{\text{tight}}$  is the number of fake leptons which pass the tight lepton selection (See Section 4.2.1)  
730 and  $N_{\text{fake}}^{\text{loose}}$  is the number of fake leptons which pass the loose lepton selection (See Section 4.2.1). The probability  
731 of one fake lepton to occur,  $P(\text{one fake } \ell)$ , is proportional to  $\epsilon$  and the probability for two fakes to occur is simply,

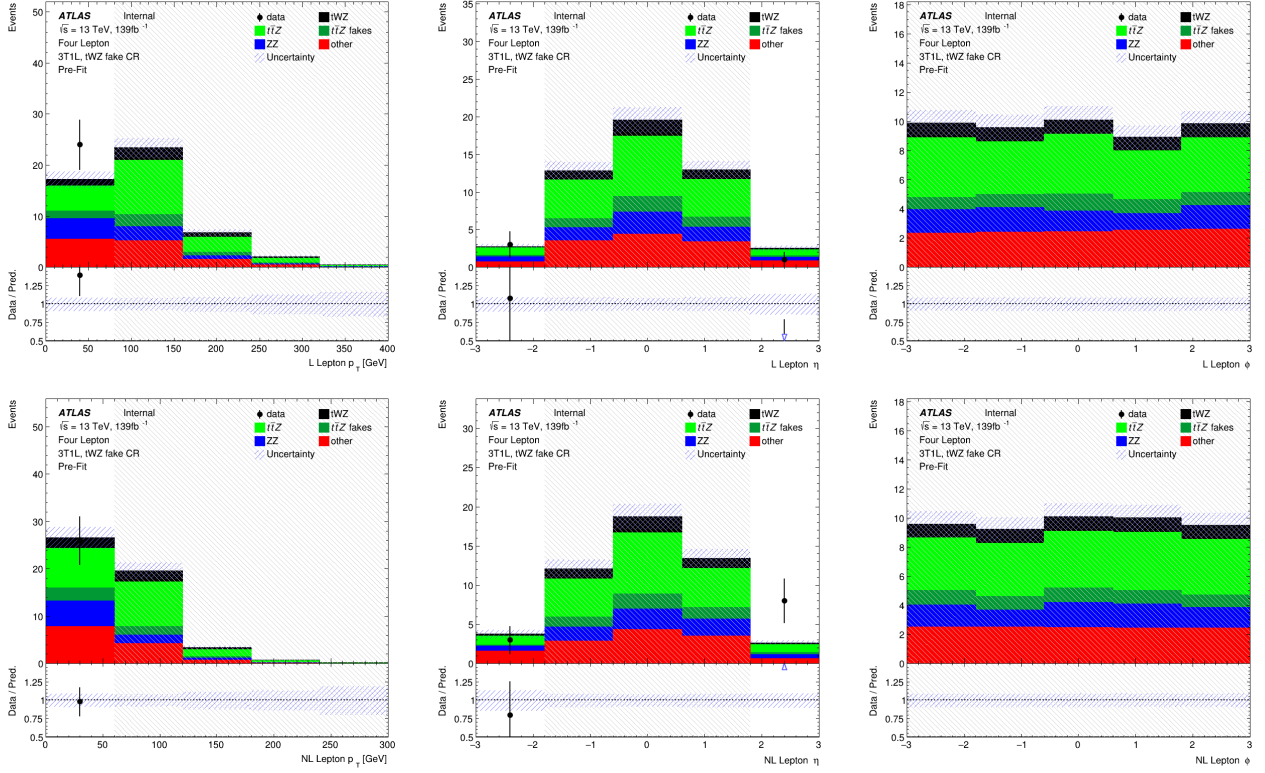


Figure 4.21: MC predictions for  $p_T$ ,  $\eta$  and  $\phi$  for leading (L) leptons (top row) and next-to-leading (NL) leptons (bottom row) in the  $(tWZ)$ fake CR region is shown.

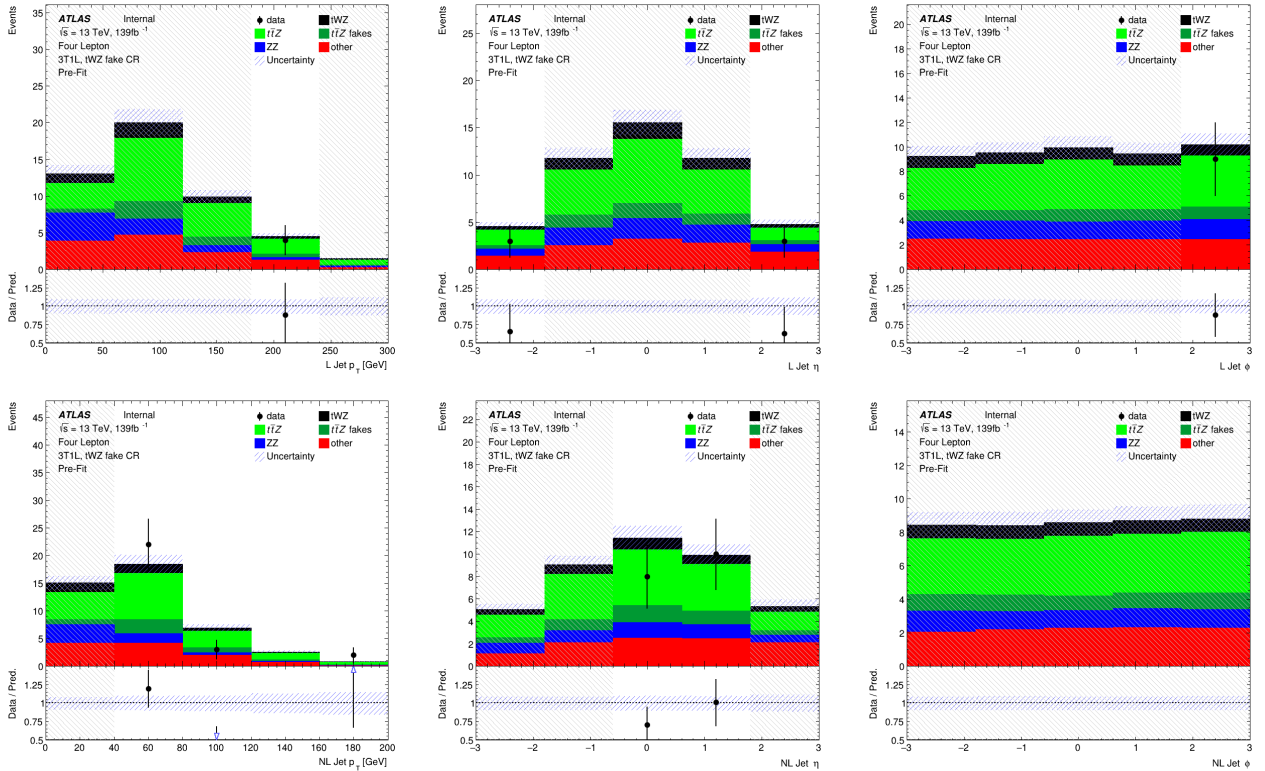


Figure 4.22: MC predictions for  $p_T$ ,  $\eta$  and  $\phi$  for leading (L) jets (top row) and next-to-leading (NL) jets (bottom row) in the  $(tWZ)$ fake CR region is shown.

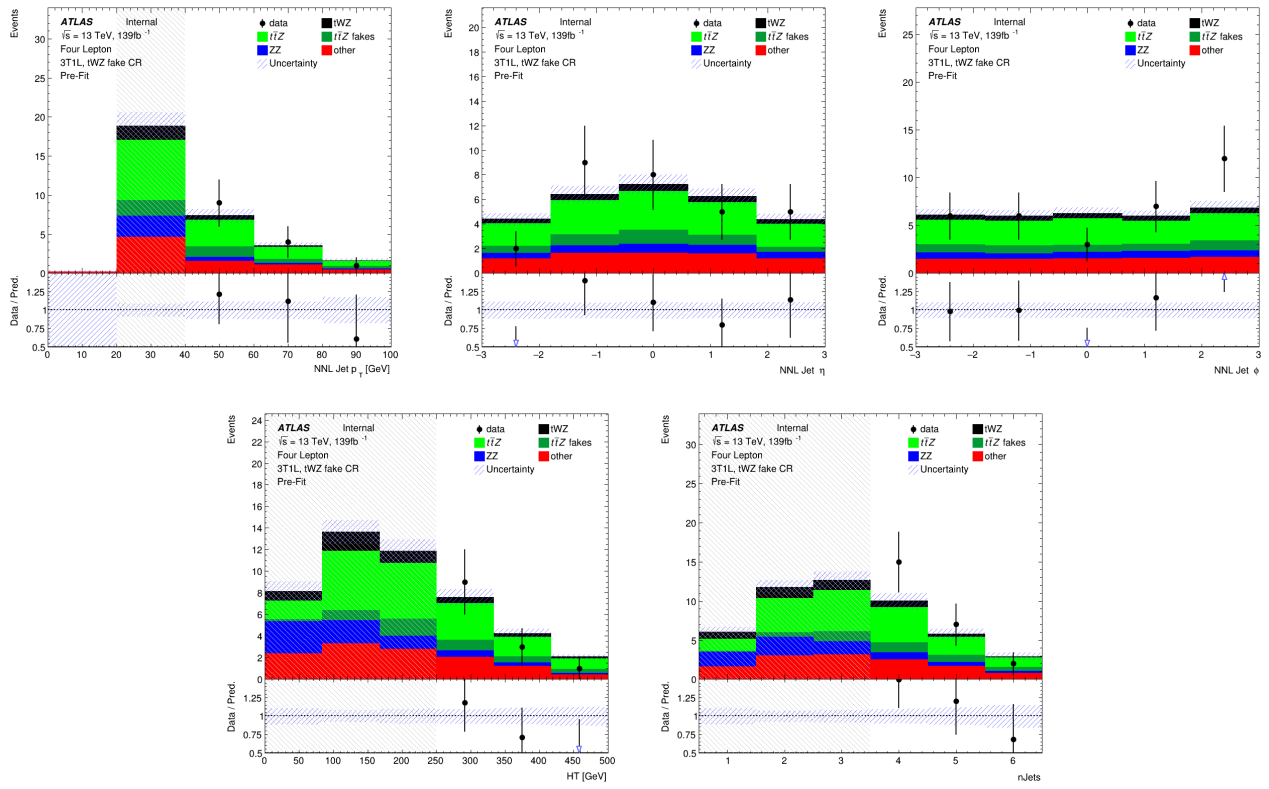


Figure 4.23: **Top row:** MC predictions for  $p_T$ ,  $\eta$  and  $\phi$  for next-to-next-to-leading (NNL) jets in the  $(tWZ)_{\text{fake}}$  CR region is shown. **Bottom row:** MC predictions for  $H_T$  (scalar sum of Jet  $p_T$ ) (left) and the Number of jets (right) in the  $(tWZ)_{\text{fake}}$  CR region is shown.

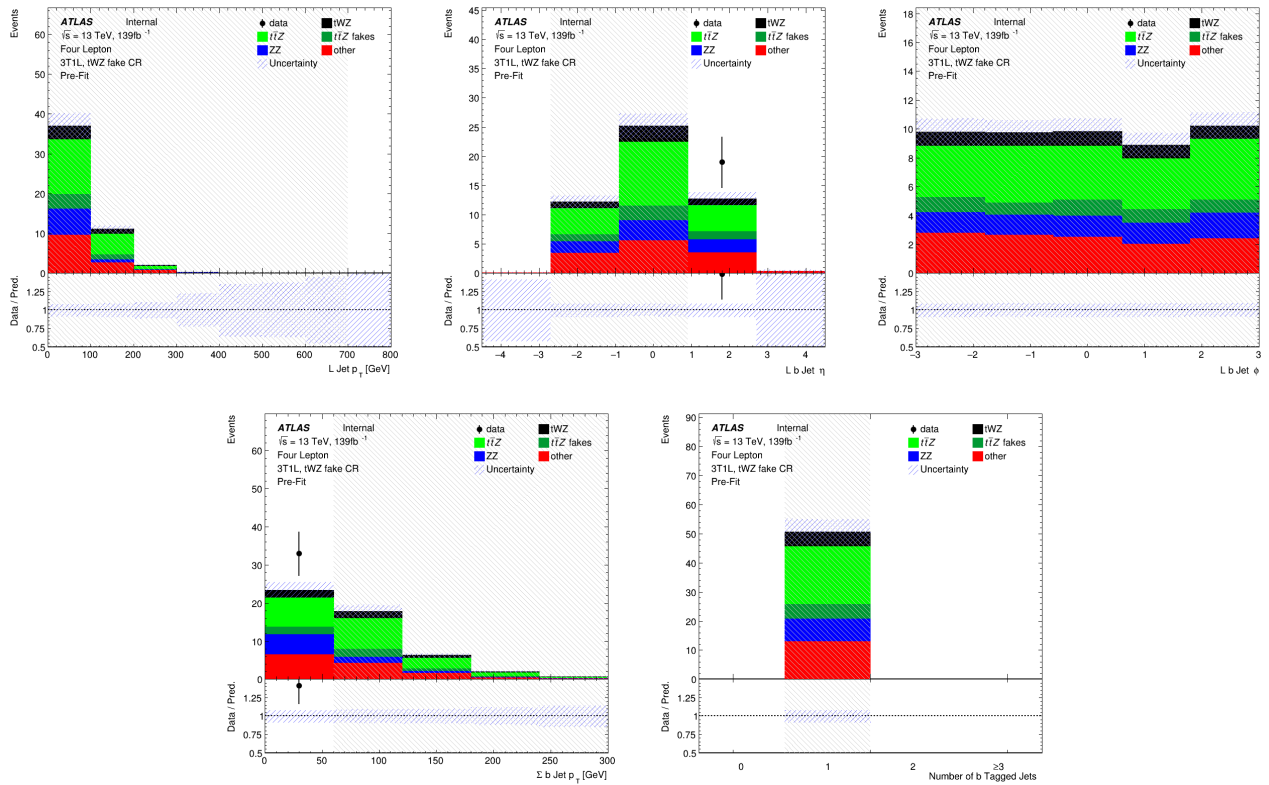


Figure 4.24: **Top row:** MC predictions for  $p_T$ ,  $\eta$  and  $\phi$  for leading b-tagged jets in the  $(tWZ)_{\text{fake}}$  CR region is shown. **Bottom row:** MC predictions for the scalar sum of b-tagged jet  $p_T$  (left) and the Number of b-tagged jets (right) in the  $(tWZ)_{\text{fake}}$  CR region is shown.

732  $P(\text{two fake } \ell) = (P(\text{one fake } \ell))^2 \propto \epsilon^2$ . Since  $\epsilon < 1$ , we have  $P(\text{one fake } \ell) \ll P(\text{two fake } \ell)$ . For this analysis we  
733 shall investigate the fake lepton component to the highest order and therefore we will consider the case where at  
734 least one fake lepton occurs in a  $t\bar{t}Z$  event.

735

736 Firstly, we split up the dominant  $t\bar{t}Z$  background into  $t\bar{t}Z$  and  $(t\bar{t}Z)_{\text{fake}}$  components. Secondly, we define a  
737  $(tWZ)_{\text{fake}}$  CR (See Section 4.4) which is enhanced in fakes and aims to constrain the  $(t\bar{t}Z)_{\text{fake}}$  background in the  
738 SR.

739

740 All events which contribute to the  $(t\bar{t}Z)_{\text{fake}}$  background are determined by the IFF Truth Classifier [51]. The  
741 IFF Truth Classifier is a tool which aims to classify leptons based off their truth information. It uses the more  
742 general MCTruthClassifier [61] tool's output as input and returns one of the following lepton categories: Unknown,  
743 KnownUnknown (leptons which can (in principle) be classified, but the MCTruthClassifier fails to classify the  
744 lepton's truth type or origin), IsoElectron, ChargeFlipIsoElectron, PromptMuon, PromptPhotonConversion,  
745 ElectronFromMuon, TauDecay, BHadronDecay, CHadronDecay or LightFlavorDecay (More details [52]). Given  
746 these categories, we consider leptons classified as PromptPhotonConversion, BHadronDecay, CHadronDecay or  
747 LightFlavorDecay (i.e. a lepton originating from the decay of a  $b$ -Hadron,  $c$ -Hadron or light-flavour jet) to be  
748 fakes. We require that events which contribute to the  $(t\bar{t}Z)_{\text{fake}}$  background are those where at least one lepton  
749 from the  $t\bar{t}Z$  sample are classified by the IFF Truth Classifier with one of the four aforementioned categories.

750

751 The  $(tWZ)_{\text{fake}}$  CR aims to be as similar as possible to the  $tWZ$  SRs, but enhanced in fakes. This CR can then  
752 be used to constrain the normalisation of the  $(t\bar{t}Z)_{\text{fake}}$  template. To ensure that this region is enhanced in fakes,  
753 we require that it contains 3 tight leptons and 1 loose lepton, since loose leptons are more likely to be fakes. By  
754 using the  $p_T$  of the loose lepton ( $p_T(\text{Loose Lepton})$ ) in this region as the variable used in the fit, the shape (and  
755 normalisation) of the  $(t\bar{t}Z)_{\text{fake}}$  template can be constrained.

756

757 In Figure 4.25, the number of leptons classified as fake, split up by their IFF Truth classification, in each region is  
758 shown.

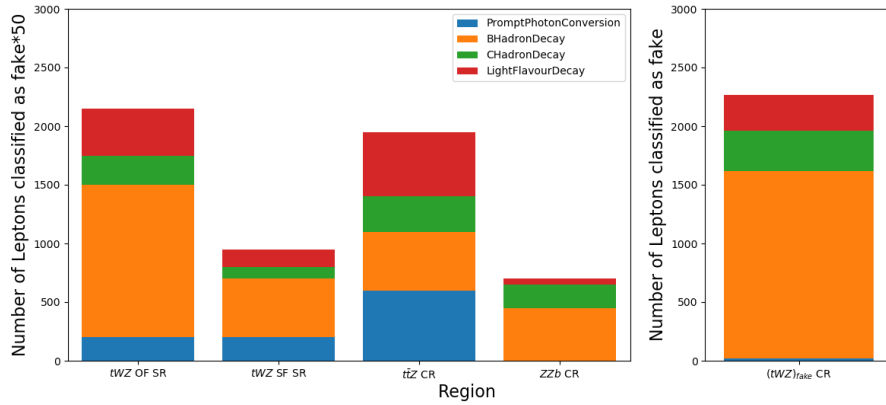


Figure 4.25: The number of leptons classified as fake, split up by their IFF Truth classification, in each region is shown. The left panel shows the number of leptons classified as fakes, scaled by a factor of 50, on the y-axis. The right panel shows the number of leptons classified as fakes (unscaled), on the y-axis. The different signal and control regions are shown on the x-axes of the left and right panels. The IFF truth classification of the leptons are shown in the legend and correspond to the different coloured stacked histograms.

759 Around 50 times more fake leptons pass our selection criteria for the  $(tWZ)_{\text{fake}}$  CR, compared to remaining four  
760 regions. This relative abundance of fake leptons present in the  $(tWZ)_{\text{fake}}$  CR further justifies our use of this region  
761 to constrain the fake lepton component.

762

763 In Figure 4.26, the relative dominance of the different classifications for fake leptons (classified by the IFF truth  
764 classified) in each region, is shown.

765 The majority of fake leptons which pass our selection criteria originate from the decay of  $b$ -hadrons, in all regions  
766 but the  $t\bar{t}Z$  CR. The smaller proportion of fake leptons originating from  $b$ -hadron decays in the  $t\bar{t}Z$  CR could

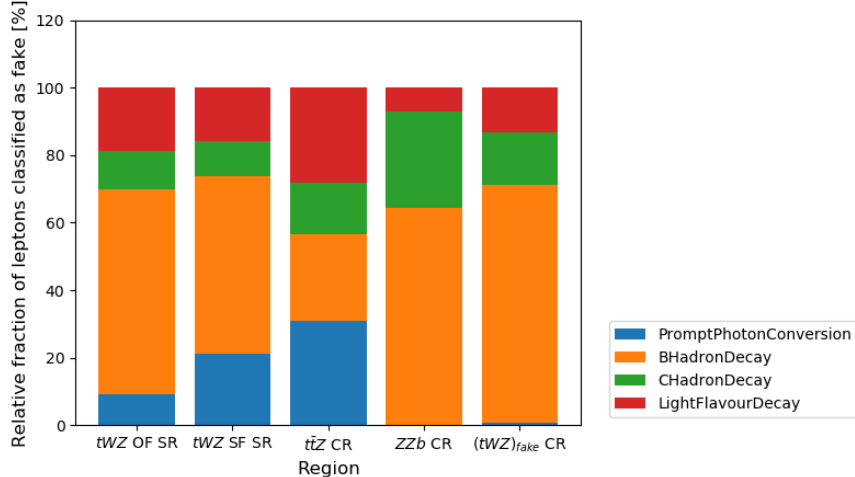


Figure 4.26: The relative dominance of the different classifications for fake leptons (classified by the IFF truth classified) in each region, is shown. The relative dominance of leptons classified as fakes, as a fraction of the total number of fake leptons (in each region), is shown on the y-axis. The different signal and control regions are shown on the x-axis. The IFF truth classification of the leptons are shown in the legend and correspond to the different coloured stacked histograms.

possibly be due to statistical fluctuations resulting from the low number of fake leptons which pass our selection criteria in this region ( $\sim 40$  fake leptons).

In Figure 4.27, the amount of fake and real  $t\bar{Z}$  events which pass our selection criteria, in each region, is shown. Around 20% of all  $t\bar{Z}$  events are classified as fake events (having one or more of its leptons being classified as fake) in the  $(tWZ)_{fake}$  CR. The  $tWZ$  OF SR,  $tWZ$  SF SR,  $t\bar{Z}$  CR and  $ZZb$  CR have less than 1% of their total  $t\bar{Z}$  events being fake. The non-negligible amount of fake  $t\bar{Z}$  events present in the  $(tWZ)_{fake}$  CR, allows the  $t\bar{Z}$  fake background to be constrained by the  $(tWZ)_{fake}$  CR.

## 4.7 Machine Learning Techniques

Now that we have our baseline selections applied and our regions defined, we implement two Boosted Decision Trees (BDT) in order to discriminate between  $tWZ$  and our most prominent background process,  $t\bar{Z}$  and  $ZZ$ . We chose to use a BDT, as opposed to another ML algorithm, since they are very stable and perform well with minimal/no optimisation or tweaking of the hyper parameters. A multi-layered sequential neural network was tried, however, it was out-performed by a BDT. More specifically, Scikit-Learn’s `GradientBoostingClassifier` [71] was used.

Two different BDTs were used, the first aims to discriminate between  $tWZ$  events and its major backgrounds,  $t\bar{Z}$  and  $ZZ$ . The second aims to discriminate between  $\ell b$  systems which originate from the decay of a top quark ( $t \rightarrow W(\rightarrow \ell\nu)b$ ) and those which do not. We refer to these two BDTs as an **event-level** and an **object-level** classifier respectively. The discriminator output from the object-level BDT can be converted to a variable which can then be used as input to the event-level BDT.

### 4.7.1 Object-level BDT

The object-level BDT was trained on a  $t\bar{t}$  sample with a baseline selection of exactly 1 tight lepton with  $p_T > 28$  GeV. Additionally, jets in this sample are required to have  $p_T > 20$  GeV.  $b$ -tagged jets are identified by the 77% DL1r working point. These baseline selections were chosen to mimic those used in the event selection of the analysis (outlined in Table 4.3). We opted to use this disjoint  $t\bar{t}$  sample as to avoid resorting to use our MC samples used in the rest of the analysis which is heavily limited on statistics, therefore maximizing the amount of MC statistics used in the fitting procedure and the training of the event-level BDT.

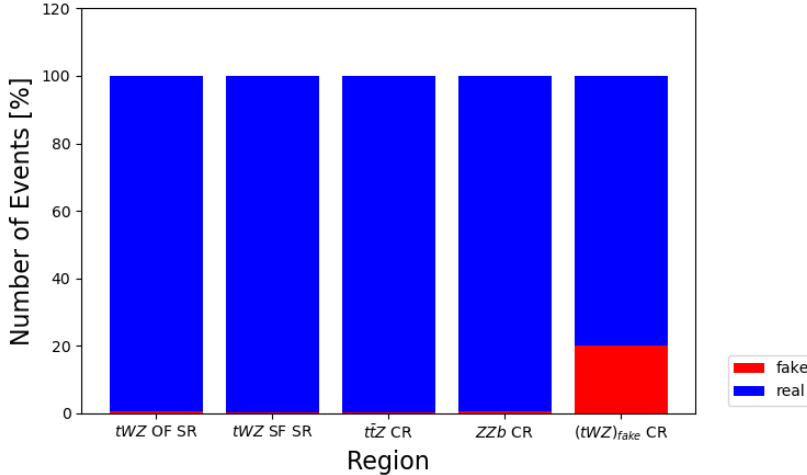


Figure 4.27: The percentage of fake and real  $t\bar{t}Z$  events which pass our selection criteria, in each region, is shown. The relative number of fake and real events (in % of the total number of events in the nominal and fake  $t\bar{t}Z$  background samples) is shown on the y-axis. The different signal and control regions are shown on the x-axis. The blue and red histograms represent the percentage of real and fake events (out of the total number of events in the nominal and fake  $t\bar{t}Z$  background samples), respectively.

795 The signal class is defined to consist of reconstructed  $\ell b$  systems (defined as the sum of the 4-vectors of the  
 796 lepton and  $b$ -jet) coming from top quarks which are well matched to their truth counterparts. In particular, we  
 797 require that  $\Delta R$  between the reconstructed and truth  $\ell b$  system is less than 0.05. We additionally require that the  
 798 reconstructed lepton and the truth top have charges with the same sign (since  $t \rightarrow b\ell^+\bar{\nu}_\ell$  and  $\bar{t} \rightarrow \bar{b}\ell^-\nu_\ell$ ). The  
 799 background class is defined to consist of all reconstructed  $\ell b$  systems which fail to pass the criteria for  $\ell b$  systems  
 800 which are labelled as signal. These definitions for the signal and background classes ensure that the signal class  
 801 consists of mostly  $\ell b$  systems originating from tops and the background class consists of mostly  $\ell b$  systems which  
 802 do not originate from a top decay.

803 Different observables corresponding to an  $\ell b$  system were used as input to training. The optimum values  
 804 for the hyper-parameters used were determined by training the BDT with a range of different values for the  
 805 hyper-parameters and choosing the set of values which maximized the mean accuracy (based off 5 fold kfold  
 806 cross-validation). This method is more commonly referred to as hyper-parameter optimisation or tuning. After  
 807 hyper-parameter optimisation, the mean accuracy of each fold increased from 0.76 to 0.77 ( $\sim 1\%$  increase). Input  
 808 features can be assigned a score called *variable importance*, based on their usefulness on predicting a target  
 809 variable (in this case, a signal or background event). The variable importance for any given variable was obtained  
 810 by computing the mean accuracy of the model, removing the variable from training, retraining the model and  
 811 computing the mean accuracy of this new model. The difference between mean accuracies of the unaltered model  
 812 and the retrained model (after removal of the variable) gives us the variable importance of the variable of interest.  
 813 This method returns positive values for variables which increase the mean accuracy of the model and negative  
 814 values for variables which decrease the mean accuracy of the model. Variables with negative variable importances  
 815 were completely removed from training.

817 In Table 4.6, the variables used in training the object-level BDT are shown.  
 818 In Figure 4.28, normalised distributions of the signal and background classes for the training set of all variables  
 819 used in the object-level BDT are show.

821 Overall the BDT input variables show a large amount of discrimination.

822 We can check the modelling of the input variables to the object-level BDT by studying the agreement between data  
 823 and simulation in the  $t\bar{t}Z$  CR. In Figure 4.29, MC predictions for the input variables to the object-level BDT in  
 824 the  $t\bar{t}Z$  CR are shown.  
 825 Overall, there is good agreement between data and simulation for the input variables to the object-level BDT in

Observable	Description
$m(\ell b)$	Invariant mass of the $\ell b$ system
$p_T(\ell b)$	$p_T$ of the $\ell b$ system
$\Delta\eta(\ell, b)$	$\Delta\eta$ between the $\ell$ and $b$ -tagged jet
$\Delta\phi(\ell, b)$	$\Delta\phi$ between the $\ell$ and $b$ -tagged jet
$\Delta R(\ell, b)$	$\Delta R$ between the $\ell$ and $b$ -tagged jet

Table 4.6: A list of the observables used in the object-level BDT, ordered by importance (descending, top to bottom) is shown.

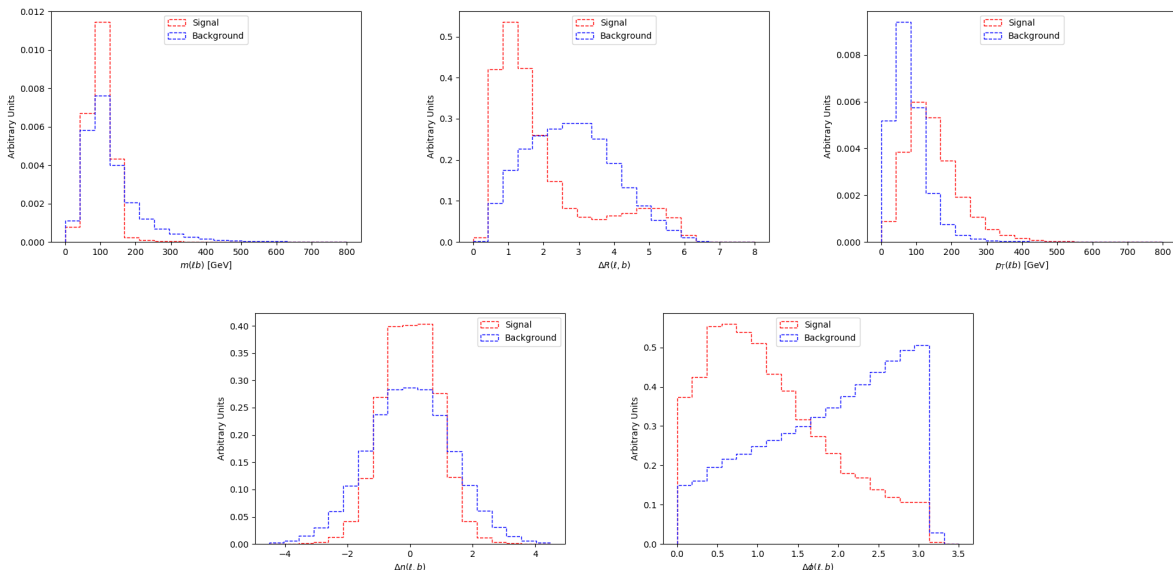


Figure 4.28: Normalised distributions of the signal and background classes for the training set of all variables used in the object-level BDT (ordered from top left to bottom right via decreasing importance) are shown. The red and blue dotted lined histograms represent the signal and background classes events (normalised to an area of 1), respectively. The variable used in training is shown on the x-axis. The y-axis shows the relative number of events for the signal and background classes (in arbitrary units). **From top left to bottom right:** Invariant mass of the  $\ell b$  system.  $\Delta R$  between the  $\ell$  and  $b$ -tagged jet. The  $p_T$  of the  $\ell b$  system.  $\Delta\eta$  between the  $\ell$  and  $b$ -tagged jet.  $\Delta\phi$  between the  $\ell$  and  $b$ -tagged jet.

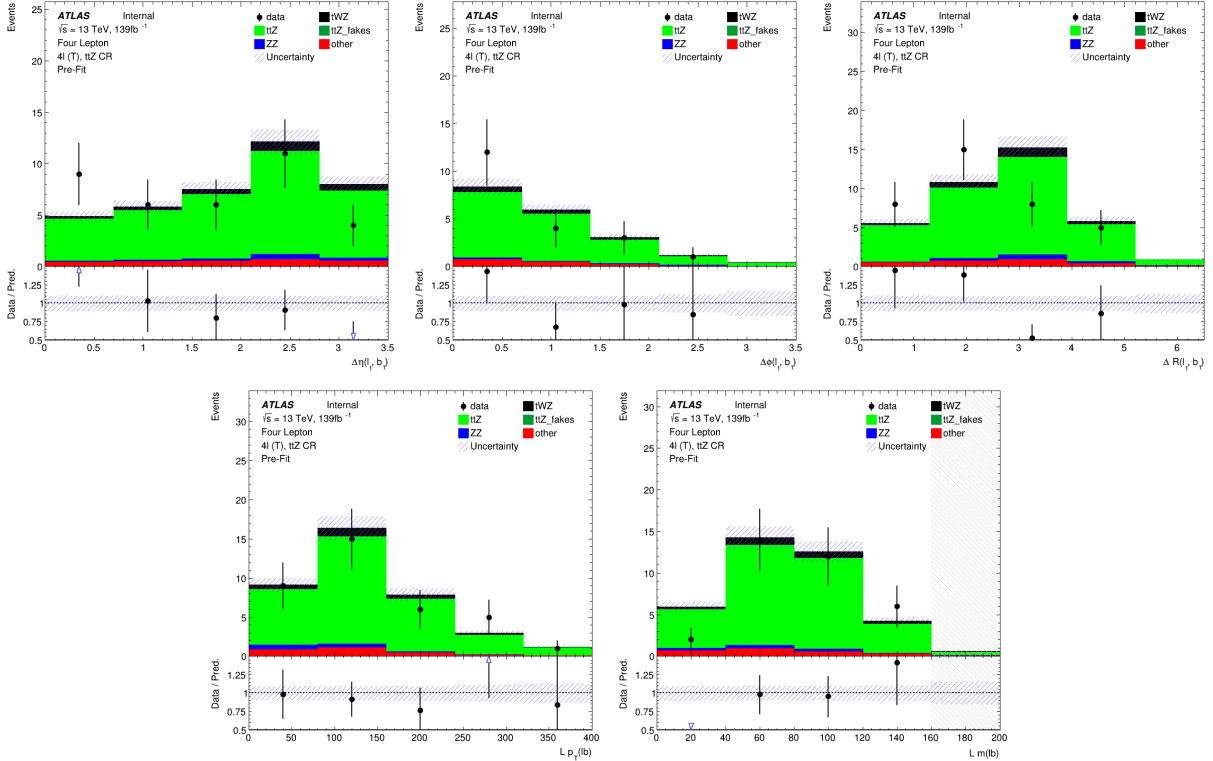


Figure 4.29: Pre-fit distributions of variables used as input to the object-level BDT (ordered from top left to bottom right via decreasing importance), in the  $t\bar{t}Z$  CR, are shown. The data is given by the black points and the MC predictions for each process are given by the histograms. The vertical lines on the data points represent the statistical uncertainty in the data and the blue diagonally-lined bands represent the total (statistical and systematic added in quadrature) uncertainty. The lower panel in each plot shows the ratios of the data to the theoretical predictions. Bins with a  $\frac{signal}{background}$  yield greater than 0.1 are kept blinded. Blinded bins are shaded with black diagonal lines and their data points are omitted. **From top left to bottom right:**  $\Delta\eta$  between the lepton and  $b$ -jet of the leading  $\ell b$  system.  $\Delta\phi$  between the lepton and  $b$ -jet of the leading  $\ell b$  system.  $\Delta R$  between the lepton and  $b$ -jet of the leading  $\ell b$  system.  $p_T$  of the leading  $\ell b$  system. Mass of the leading  $\ell b$  system.

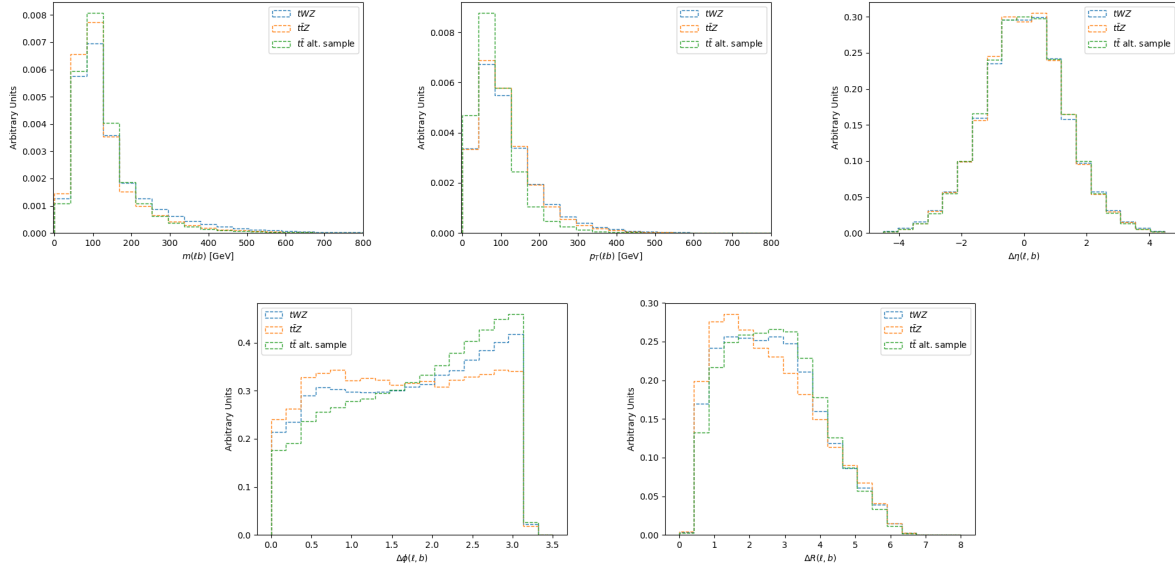


Figure 4.30: Normalised distributions of input variables (ordered from top left to bottom right via decreasing importance) to the object-level BDT in the alternative  $t\bar{t}$ ,  $tWZ$  and  $ttZ$  samples, are shown. The green, blue and orange dotted lined histograms represent events from the alternative  $t\bar{t}$ ,  $tWZ$  and  $ttZ$  samples (normalised to an area of 1), respectively. The variable used in training is shown on the x-axis. The y-axis shows the relative number of events (in arbitrary units). **From top left to bottom right:** Invariant mass of the  $\ell b$  system.  $\Delta R$  between the  $\ell$  and  $b$ -tagged jet. The  $p_T$  of the  $\ell b$  system.  $\Delta\eta$  between the  $\ell$  and  $b$ -tagged jet.  $\Delta\phi$  between the  $\ell$  and  $b$ -tagged jet.

the  $t\bar{t}Z$  CR. This suggests that the input variables to the object-level BDT are well-modelled and are reasonable to include as inputs to the object-level BDT.

A final check can be done to study the similarity of the  $\ell b$  systems present in the alternative  $t\bar{t}$  sample which we use for training the object-level BDT, and the  $\ell b$  systems which we aim to identify using the object-level BDT. More specifically, we want to ensure that the  $\ell b$  systems in the alternative  $t\bar{t}$  sample are similar enough to those in the  $tWZ$  and  $ttZ$  samples (see Table 4.1). In Figure 4.30, normalised distributions of input variables to the object-level BDT in the alternative  $t\bar{t}$ ,  $tWZ$  and  $ttZ$  samples, are shown.

The distributions of the input variables to the object-level classifier, for the three samples, are similar and show no large deviations between one another. This tells us that the  $\ell b$  systems which we use in training are similar enough to those we aim to identify using the classifier. The use of the alternative  $t\bar{t}$  sample for training the object-level classifier is therefore sufficient for this analysis.

In Table 4.7, the hyper-parameters used in the object-level BDT is shown.

Hyper-parameter	Value	Description
loss	deviance	The loss function to be optimised
criterion	friedman_mse	The function used to measure the quality of a split
n_estimators	200	The number of boosting stages to perform
learning_rate	0.1	The step size at each iteration during optimisation
max_depth	6	The maximum depth of the individual regression estimators
min_samples_split	2	The minimum number of samples (events) required to split an internal node
min_samples_leaf	1	The minimum number of samples (events) required to be at a leaf node
validation_fraction	0.1	The proportion of training data to set aside as validation set for early stopping
n_iter_no_change	20	Training terminates when the validation score (determined by the validation set) does not improve in all of the previous

Table 4.7: A list of the hyper-parameters used in the object-level BDT is shown. Hyperparameters not listed in this table use the default values as stated in the Scikit-learn Documentation[72].

The number of events used in training for the signal and background classes were 49871 and 384152 respectively. Imbalanced datasets can cause ML classifiers to ignore small classes while concentrating on classifying large classes

more accurately, which may result in the trained classifier performing sub-optimally. In order to correct this dataset imbalance, we ensure that the relative weighting of each event is such that the sum of the signal weights is equal to the sum of the background weights. In Figure 4.31 the normalised histograms of the training and test sets (extracted from fold 5 from a 5 fold kfold cross validation) for signal and background is shown.

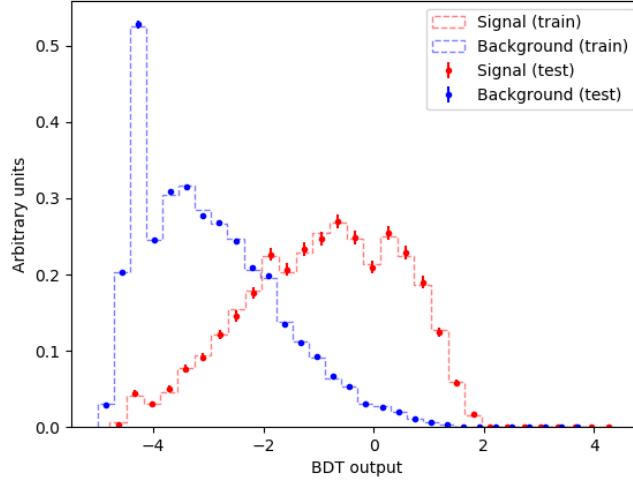


Figure 4.31: Normalised histograms of the object-level BDT discriminator output from the signal and background classes for the training and test sets from the 5th fold in a 5 fold kfold cross validation is shown. The output of the object-level BDT is shown on the x-axis and the relative number of events (in arbitrary units) is shown on the y-axis. The training set for the signal class is shown by the red dotted histogram. The test set for the signal class is shown by the red points, with the total uncertainty represented by the vertical error bars. The training set for the background class is shown by the blue dotted histogram. The test set for the background class is shown by the blue points, with the total uncertainty represented by the vertical error bars.

We can see that the shapes of the training and test sets for both signal and background are very similar. This is a good indicator that no over-training occurred. Another over-training check is performed using 5 fold kfold cross validation. We ensure that the variance of the mean accuracy of each folds' test set in cross validation is substantially small. This indicates that fluctuations in features from different training sets are not learnt by the classifier. For the object-level classifier, a variance of  $3.24 \times 10^{-7}$  was calculated for the mean accuracies of each folds' test set in cross validation, providing further evidence that no over-training occurred.

The output from the object-level BDT was used to construct a variable to be used as input to the event-level BDT. The event-level BDT aims to discriminate between  $tWZ$  and our most prominent background,  $t\bar{t}Z$ . We therefore aim to construct a variable from the output of the object-level BDT which discriminates well between  $tWZ$  and  $t\bar{t}Z$ . Since  $tWZ$  events contain one top quark and  $t\bar{t}Z$  events contain two top quarks, we expect that  $tWZ$  events have one  $\ell b$  combination which scores well and we expect that  $t\bar{t}Z$  events have two  $\ell b$  combinations which score well. We construct a variable,  $BDTScore(\frac{\text{Best}}{\text{2nd Best}})$ , which takes the ratio of the scores of the top scoring  $\ell b$  system to the 2nd best scoring  $\ell b$  system. We expect this variable to be large for  $tWZ$  events and closer to one for  $t\bar{t}Z$  events, therefore providing discrimination between  $tWZ$  and  $t\bar{t}Z$ .

In Figure 4.32, normalised distributions of the signal and total background of the  $BDTScore(\frac{\text{Best}}{\text{2nd Best}})$  variable in the  $tWZ$  OF SR,  $tWZ$  SF SR and  $t\bar{t}Z$  CR are shown.

There doesn't seem to be a large amount of discrimination between signal and background for  $BDTScore(\frac{\text{Best}}{\text{2nd Best}})$  in either of the above regions. We do however see some discrimination in bins near a value of 1, where the number of background events exceed the number of signal events, which is what we expect. This effect is slightly more exaggerated in the  $t\bar{t}Z$  CR than the  $tWZ$  SRs. This can be explained since we expect to have a larger proportion of  $t\bar{t}Z$  events (events with two  $\ell b$  systems) in the  $t\bar{t}Z$  CR. An excess of signal events (compared to background) are observed at larger values. This is to be expected, since these events correspond to a lower score by the  $\ell b$  classifier on the 2nd best scoring  $\ell b$  system in the event. The 2nd best scoring  $\ell b$  system in a  $tWZ$  event is expected to be low, since there is only one  $\ell b$  system originating from a top. Despite the apparent lack of discrimination

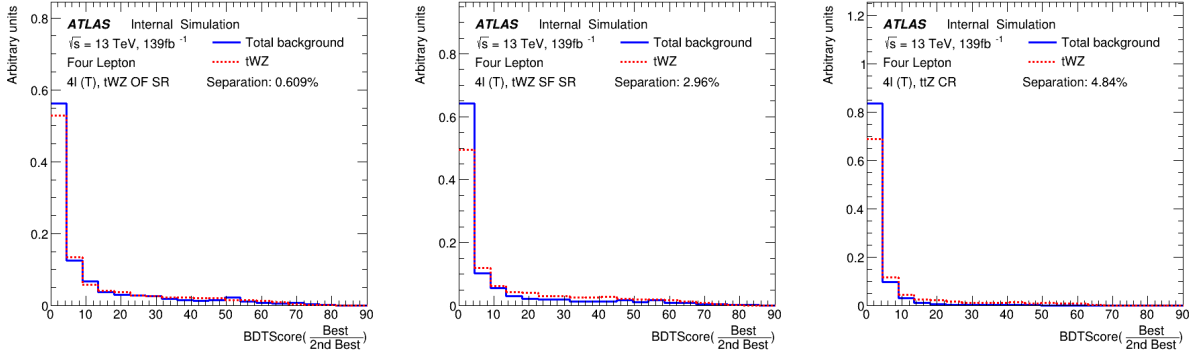


Figure 4.32: Normalised distributions of the signal and total background of the  $\text{BDTScore}(\frac{\text{Best}}{\text{2nd Best}})$  variable in the  $tWZ$  OF SR,  $tWZ$  SF SR and  $t\bar{t}Z$  CR are shown (left to right). The dotted red and solid blue lines represent the distributions (normalised to an area of 1) of the signal and total background events respectively. The x-axis shows the  $\text{BDTScore}(\frac{\text{Best}}{\text{2nd Best}})$  and the y-axis show the relative number of events (in arbitrary units).

between signal and background events from this variable, when used as input to training in the event-level BDT (see Section 4.7.2), improves the mean accuracy of the classifier. This tells us that the event-level BDT is taking advantage of the discrimination between signal and background present in the  $\text{BDTScore}(\frac{\text{Best}}{\text{2nd Best}})$  variable.

In an attempt to optimise the performance of the object-level BDT, we aim to train on signal events which are as pure in  $\ell b$  systems originating from top quarks, as possible. Similarly, we aim to train on background events which are as pure in  $\ell b$  systems not originating from top quarks, as possible. This is done by studying the distribution of  $\Delta R$  between the reconstructed  $\ell b$  system and the truth  $\ell b$  system ( $\Delta R((lb)_{reco}, (lb)_{truth})$ ), and excluding  $\ell b$  systems from training which are moderately matched in  $\Delta R$  to their truth counterparts, leaving well matched  $\ell b$  systems being labelled as signal and badly matched  $\ell b$  systems labelled as background. We call the  $\Delta R$  range where  $\ell b$  systems are excluded from training, the exclusion region. In Figure 4.33, the distribution of  $\Delta R$  between the reconstructed  $\ell b$  system and the truth  $\ell b$  system ( $\Delta R((lb)_{reco}, (lb)_{truth})$ ) in the alternative  $t\bar{t}$  sample, along with the exclusion region, is shown.

A large number of reconstructed  $\ell b$  systems have  $\Delta R((lb)_{reco}, (lb)_{truth})$  at values near 0. These are matched (in  $\Delta R$ ) extremely well to truth  $\ell b$  systems originating from top quarks. We therefore define our exclusion region to be between  $0.05 < \Delta R((lb)_{reco}, (lb)_{truth}) < 3.0$ , such that all reconstructed  $\ell b$  systems with  $\Delta R((lb)_{reco}, (lb)_{truth}) \leq 0.05$  are labelled as signal and reconstructed  $\ell b$  systems with  $\Delta R((lb)_{reco}, (lb)_{truth}) \geq 3.0$  are labelled as background. All reconstructed  $\ell b$  systems with  $0.05 < \Delta R((lb)_{reco}, (lb)_{truth}) < 3.0$  are excluded from training.

The performance of the object-level BDT with and without the exclusion region can be compared by studying the discrimination between signal and background events in the  $\text{BDTScore}(\frac{\text{Best}}{\text{2nd Best}})$  variable (object-level output converted to an event-level variable to be used in the event-level BDT) for both object-level BDTs. In Figure 4.34, normalised distributions of  $\text{BDTScore}(\frac{\text{Best}}{\text{2nd Best}})$  using the object-level BDT without the exclusion region (see Figure 4.33) for the  $tWZ$  OF SR,  $tWZ$  SF SR and  $t\bar{t}Z$  CR are shown.

The amount of discrimination can be quantified by the separation metric, which gives the percentage of the total area of the distributions which do not overlap. A value of 1 indicates that the distributions are fully separated (no overlap) and a value of 0 indicates that the distributions have no separation (fully overlapped). We can compare the separation metrics between the  $\text{BDTScore}(\frac{\text{Best}}{\text{2nd Best}})$  variable in the  $tWZ$  OF SR,  $tWZ$  SF SR and  $t\bar{t}Z$  CR for the  $\ell b$  classifier with (Figure 4.32) and without (Figure 4.34) the exclusion region by taking the absolute difference between the two values in each region. The differences are 0.31%, 0.37% and 0.36% for the  $tWZ$  OF SR,  $tWZ$  SF SR and  $t\bar{t}Z$  CR, respectively. These differences are minimal and the object-level BDT with the exclusion region outperforms the object-level BDT without the exclusion region in the  $tWZ$  SF SR. Due to the small differences in performance between the two BDTs, for simplicity, we ultimately chose to keep the BDT with the exclusion region.

## 4.7.2 Event-level BDT

The event-level BDT was trained on 50% of the  $tWZ$  MC sample's events for the signal class and similarly, 50% of the  $t\bar{t}Z$  and  $ZZ$  MC sample's events were used for the background class. The samples we train on are

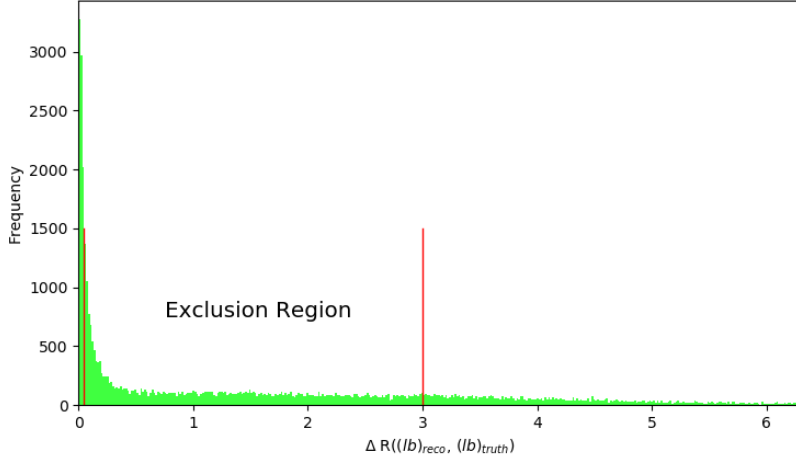


Figure 4.33: The distribution of  $\Delta R$  between the reconstructed  $\ell b$  system and the truth  $\ell b$  system ( $\Delta R((lb)_{reco}, (lb)_{truth})$ ) in the alternative  $t\bar{t}$  sample, along with the exclusion region, is shown. The  $\Delta R$  distribution is shown in green.  $\Delta R$  between the reconstructed  $\ell b$  system and the truth  $\ell b$  system ( $\Delta R((lb)_{reco}, (lb)_{truth})$ ) is shown on the x-axis. The bin frequency is shown on the y-axis. The exclusion region is shown between the vertical red lines situated at  $\Delta R((lb)_{reco}, (lb)_{truth}) = 0.05$  and  $\Delta R((lb)_{reco}, (lb)_{truth}) = 3.0$ . Reconstructed  $\ell b$  systems with  $\Delta R((lb)_{reco}, (lb)_{truth}) \leq 0.05$  are labelled as signal and reconstructed  $\ell b$  systems with  $\Delta R((lb)_{reco}, (lb)_{truth}) \geq 3.0$  are labelled as background.

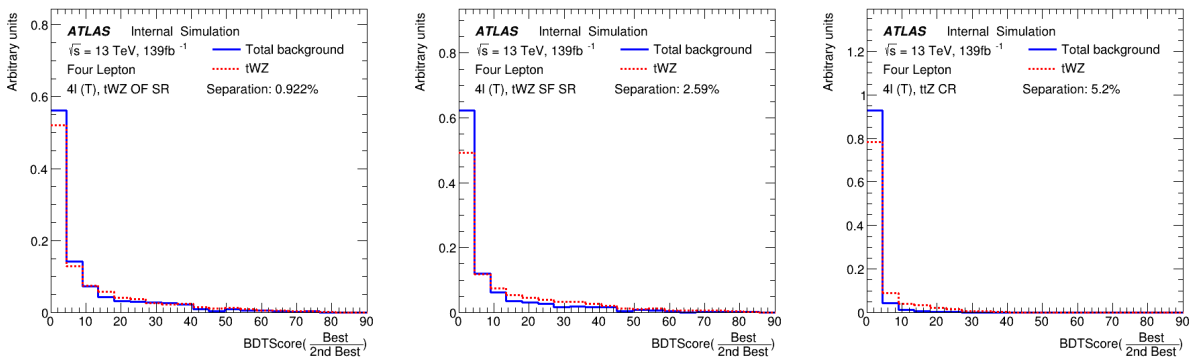


Figure 4.34: Normalised distributions of  $BDTScore(\frac{\text{Best}}{\text{2nd Best}})$  using the object-level BDT without the exclusion region (see Figure 4.33) for the  $tWZ$  OF SR,  $tWZ$  SF SR and  $t\bar{t}Z$  CR are shown (left to right). The dotted red and solid blue lines represent the distributions (normalised to an area of 1) of the signal and total background events respectively. The x-axis shows the  $BDTScore(\frac{\text{Best}}{\text{2nd Best}})$  and the y-axis show the relative number of events (in arbitrary units).

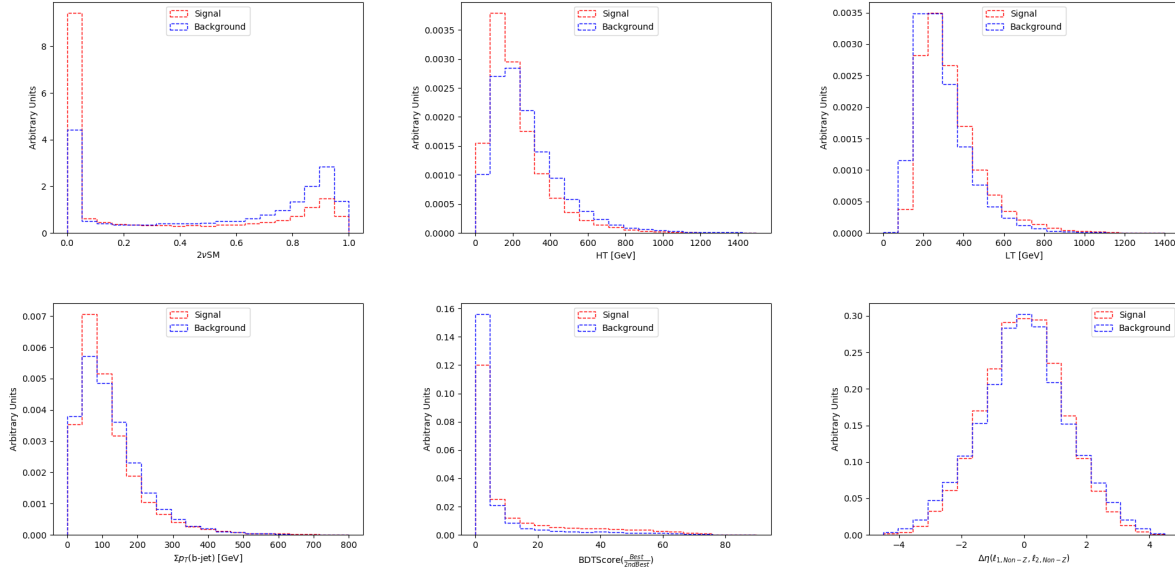


Figure 4.35: Normalised distributions of the signal and background classes for the training set of all variables used in the event-level BDT (ordered from top left to bottom right via decreasing importance) are shown. The red and blue dotted lined histograms represent the signal and background classes events (normalised to an area of 1), respectively. The variable used in training is shown on the x-axis. The y-axis shows the relative number of events for the signal and background classes (in arbitrary units). **From top left to bottom right:** Output weight from the  $2\nu\text{SM}$  algorithm (See Section 4.8). Scalar sum of jet  $p_T$ . Scalar sum of lepton  $p_T$ . Sum of  $b$ -tagged jet  $p_T$ . Ratio of the top scoring  $\ell b$  system to the 2nd best scoring  $\ell b$  system from the output of the object-level BDT (See Section 4.7.1).  $\Delta\eta$  between the two leptons, not coming from a  $Z$  candidate.

909 individual events, with the features being carefully chosen observables. These observables are chosen on the basis  
 910 that they are somewhat uncorrelated from one another and show a relatively large amount of separation power  
 911 between  $tWZ$  and  $t\bar{t}Z$ . Similarly to the object-level BDT, the optimum values for the hyper-parameters used  
 912 were determined via hyper-parameter optimisation. After hyperparameter optimisation, the mean accuracy of  
 913 each fold (determined from 5 fold kfold cross validation) increased from 0.72 to 0.74 ( $\sim 3\%$  increase). The variable  
 914 importance of each variable was computed in the same way as described for the object-level BDT (See Section 4.7.1).  
 915

In Table 4.8, the variables used in training the event-level BDT are shown.

Observable	Description
$2\nu\text{SM}$	Maximum weight from the $2\nu\text{SM}$ algorithm (See Section 4.8)
$HT$	Scalar sum of jet $p_T$
$LT$	Scalar sum of lepton $p_T$
$\sum p_T(b-jet)$	Scalar sum of $b$ -tagged jet $p_T$
$BDTScore(\frac{\text{Best}}{\text{2nd Best}})$	Ratio of the top scoring $\ell b$ system to the 2nd best scoring $\ell b$ system from the output of the object-level BDT ( $\ell b$ classifier)
$\Delta\eta(\ell_{1,\text{non-}Z}, \ell_{2,\text{non-}Z})$	$\Delta\eta$ between the two leptons, not coming from a $Z$ candidate

Table 4.8: A list of the observables used in the event-level BDT, ordered by importance (descending, top to bottom) is shown.

916 In Figure 4.35, normalised distributions of the signal and background classes for the training set of all variables  
 917 used in the event-level BDT are show.  
 918 Overall the BDT input variables show a reasonable amount of discrimination. In particular the output weight  
 919 from the  $2\nu\text{SM}$  algorithm shows the most discrimination. When determining which variables to use in training the  
 920 event-level BDT, the output weight from  $2\nu\text{SM}$  was shown to provide the most sizeable boost in performance of  
 921 the BDT. Surprisingly, the least important variable,  $\Delta\phi$  between the non- $Z$  lepton system (leptons not originating  
 922 from a  $Z$ -candidate) and the leading  $b$ -tagged jet, seem to discriminate well between signal and background. A  
 923 possible explanation for its low ranking importance is due to it being relatively highly correlated with many of the  
 924 other input variables.  
 925

926  
927  
928  
929  
930

We can check the modelling of the input variables to the event-level BDT by referring to the pre-fit distributions of data and simulation in the control regions. Note that certain variables which are ill-defined in certain regions (e.g.  $\Delta\eta(\ell_{1,\text{non-}Z}, \ell_{2,\text{non-}Z})$  in the  $ZZb$  CR, as all leptons originate from a  $b$ -jet in this region) will not be shown.

In Figure 4.36, MC predictions for the input variables to the event-level BDT in the  $t\bar{t}Z$  CR are shown.

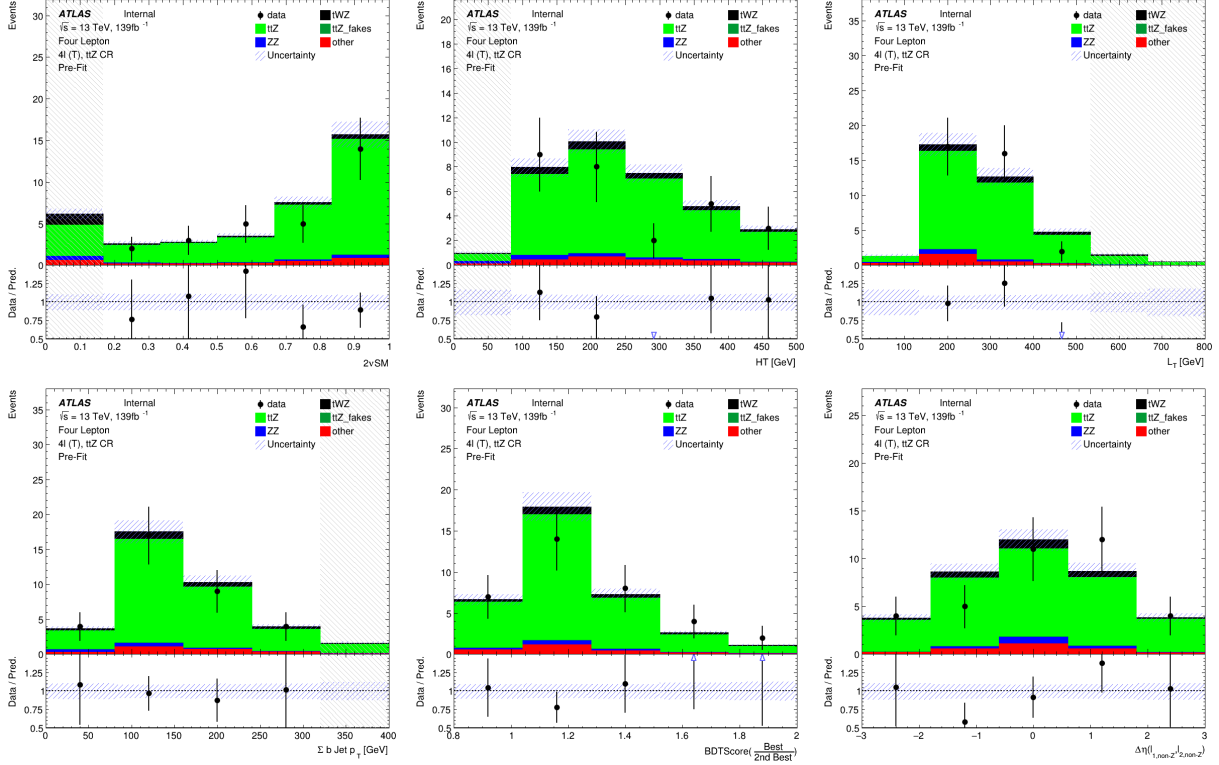


Figure 4.36: Pre-fit distributions of variables used as input to the event-level BDT (ordered from top left to bottom right via decreasing importance), in the  $t\bar{t}Z$  CR, are shown. The data is given by the black points and the MC predictions for each process are given by the histograms. The vertical lines on the data points represent the statistical uncertainty in the data and the blue diagonally-lined bands represent the total (statistical and systematic added in quadrature) uncertainty. The lower panel in each plot shows the ratios of the data to the theoretical predictions. Bins with a  $\frac{\text{signal}}{\text{background}}$  yield greater than 0.1 are kept blinded. Blinded bins are shaded with black diagonal lines and their data points are omitted. **From top left to bottom right:** Output weight from the  $2\nu\text{SM}$  algorithm (See Section 4.8). Scalar sum of jet  $p_T$ . Scalar sum of lepton  $p_T$ . Sum of  $b$ -tagged jet  $p_T$ . Ratio of the top scoring  $\ell\ell$  system to the 2nd best scoring  $\ell\ell$  system from the output of the object-level BDT (See Section 4.7.1).  $\Delta\eta$  between the two leptons, not coming from a  $Z$  candidate.

931

In Figure 4.37, MC predictions for the input variables to the event-level BDT in the  $ZZb$  CR are shown.

In Figure 4.38, MC predictions for the input variables to the event-level BDT in the  $(tWZ)_{\text{fake}}$  CR are shown.

Overall, the agreement between data and simulation for the input variables to the event-level BDT is good. Therefore, these variables are well-modelled and reasonable to include as inputs to the event-level BDT.

936

In Table 4.9, the hyper-parameters used in the event-level BDT are shown.

Since we are training on  $t\bar{t}Z$  and  $ZZ$  events for the background class, we ensure that the relative weighting of these events are such that they mimic the amount of  $t\bar{t}Z$  and  $ZZ$  expected to be present in the regions where we aim to use the BDT discriminator ( $tWZ$  SRs and  $t\bar{t}Z$  CR). This is done by applying normalization weights to each event, defined as,

$$W = \frac{\sigma \mathcal{L} \text{weight(MC)}}{\text{totalWeight(MC)}} \quad (4.2)$$

where  $\sigma$  is the cross section of the process,  $\mathcal{L}$  is the integrated luminosity,  $\text{weight(MC)}$  is the weight assigned to

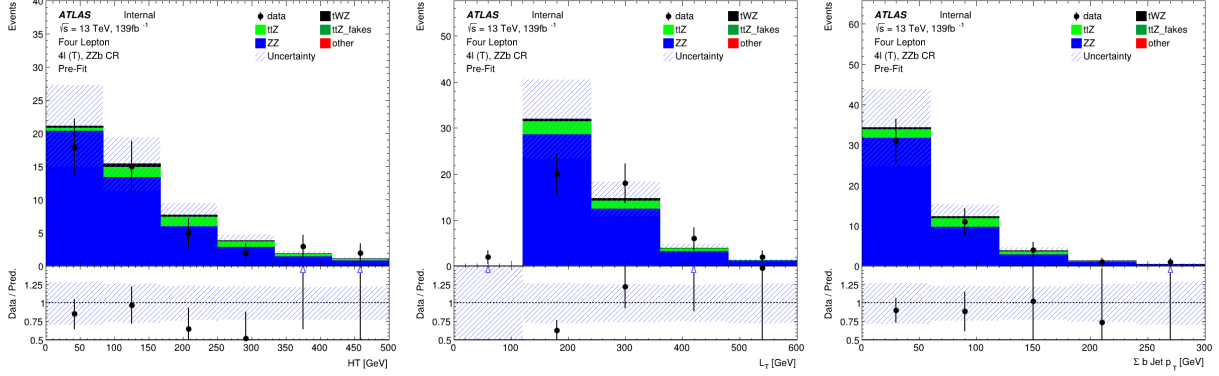


Figure 4.37: Pre-fit distributions of variables used as input to the event-level BDT (ordered from top left to bottom right via decreasing importance), in the  $Z Z b$  CR, are shown. The data is given by the black points and the MC predictions for each process are given by the histograms. The vertical lines on the data points represent the statistical uncertainty in the data and the blue diagonally-lined bands represent the total (statistical and systematic added in quadrature) uncertainty. The lower panel in each plot shows the ratios of the data to the theoretical predictions. Bins with a  $\frac{\text{signal}}{\text{background}}$  yield greater than 0.1 are kept blinded. Blinded bins are shaded with black diagonal lines and their data points are omitted. **From left to right:** Scalar sum of jet  $p_T$ . Scalar sum of lepton  $p_T$ . Sum of  $b$ -tagged jet  $p_T$ .

Hyper-parameter	Value	Description
loss	deviance	The loss function to be optimised
criterion	friedman_mse	The function used to measure the quality of a split
n_estimators	200	The number of boosting stages to perform
learning_rate	0.1	The step size at each iteration during optimisation
max_depth	6	The maximum depth of the individual regression estimators
min_samples_split	2	The minimum number of samples (events) required to split an internal node
min_samples_leaf	1	The minimum number of samples (events) required to be at a leaf node
validation_fraction	0.1	The proportion of training data to set aside as validation set for early stopping
n_iter_no_change	20	Training terminates when the validation score (determined by the validation set) does not improve in all of the previous

Table 4.9: A list of the hyper-parameters used in the event-level BDT is shown. Hyperparameters not listed in this table use the default values as stated in the Scikit-learn Documentation[72].

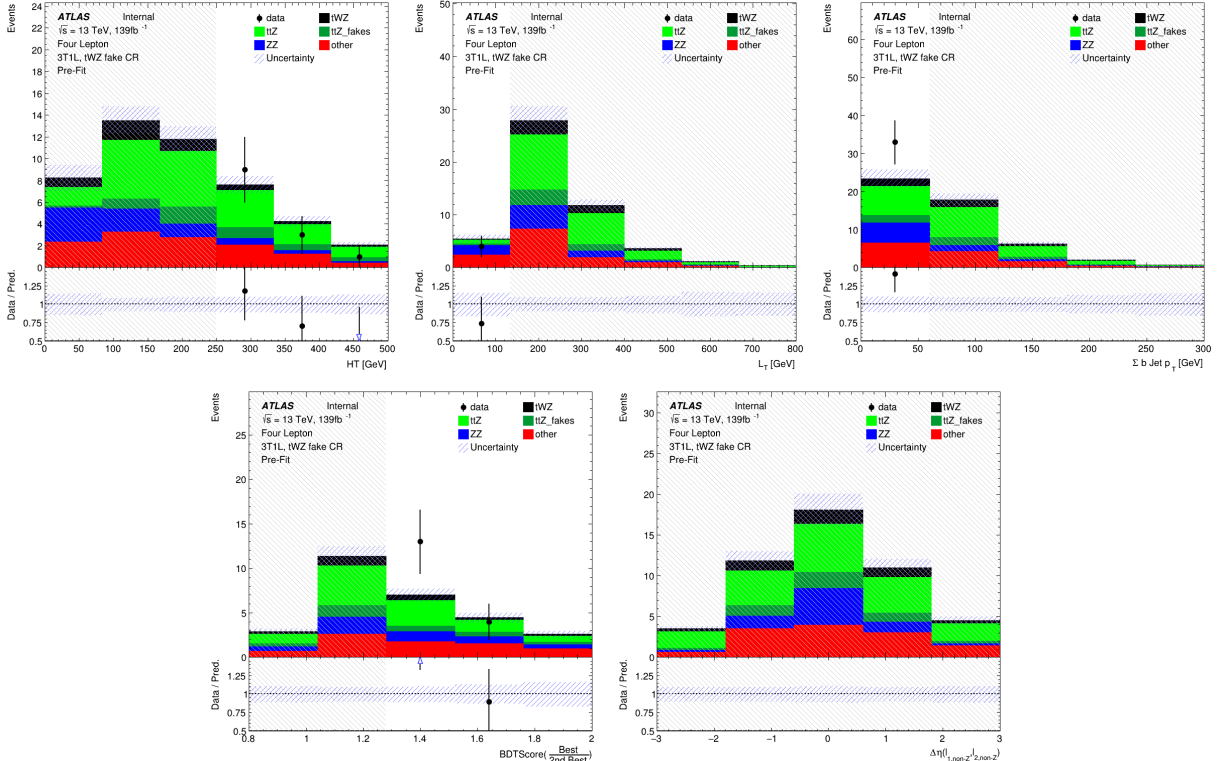


Figure 4.38: Pre-fit distributions of variables used as input to the event-level BDT (ordered from top left to bottom right via decreasing importance), in the  $(tWZ)_{\text{fake}}$  CR, are shown. The data is given by the black points and the MC predictions for each process are given by the histograms. The vertical lines on the data points represent the statistical uncertainty in the data and the blue diagonally-lined bands represent the total (statistical and systematic added in quadrature) uncertainty. The lower panel in each plot shows the ratios of the data to the theoretical predictions. Bins with a  $\frac{\text{signal}}{\text{background}}$  yield greater than 0.1 are kept blinded. Blinded bins are shaded with black diagonal lines and their data points are omitted. **From top left to bottom right:** Output weight from the  $2\nu\text{SM}$  algorithm (See Section 4.8). Scalar sum of jet  $p_T$ . Scalar sum of lepton  $p_T$ . Sum of  $b$ -tagged jet  $p_T$ . Ratio of the top scoring  $\ell b$  system to the 2nd best scoring  $\ell b$  system from the output of the object-level BDT (See Section 4.7.1).  $\Delta\eta$  between the two leptons, not coming from a  $Z$  candidate.

943 the event by the MC generator and totalWeight(MC) is the sum of those weights for all the generated events.  
 944  
 945 The number of events used in training for the signal and background classes were 41066 and 22608 respectively.  
 946 Similarly to the object-level BDT, there is a dataset imbalance. We correct this imbalance (in the same way as  
 947 before with the object-level BDT) by ensuring that the relative weighting of each event is such that the sum of the  
 948 signal weights is equal to the sum of the background weights.  
 949  
 950 In Figure 4.40 the normalised histograms of the training and test sets (extracted from fold 5 from a 5 fold kfold  
 cross validation) for signal and background is shown.

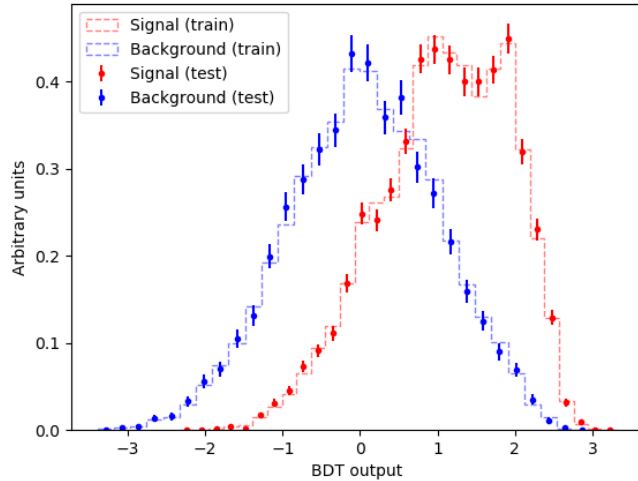


Figure 4.39: Normalised histograms of the event-level BDT discriminator output from the signal and background classes for the training and test sets from the 5th fold in a 5 fold kfold cross validation are shown. The output of the event-level BDT is shown on the x-axis and the relative number of events (normalised to have an area of 1, in arbitrary units) is shown on the y-axis. The training set for the signal class is shown by the red dotted histogram. The test set for the signal class is shown by the red points, with the total uncertainty represented by the vertical error bars. The training set for the background class is shown by the blue dotted histogram. The test set for the background class is shown by the blue points, with the total uncertainty represented by the vertical error bars.

951 We can see that the shapes of the training and test sets for both signal and background are very similar. This is  
 952 a good indicator that no over-training occurred. As with the object-level BDT, we perform another over-training  
 953 check, by ensuring that the variance of the mean accuracy of each folds' test set in a 5 fold kfold cross validation  
 954 is substantially small. This indicates that fluctuations in features from different training sets are not learnt by the  
 955 classifier. For the event-level classifier, a variance of 0.00026 was calculated for the mean accuracies of each folds'  
 956 test set in cross validation, providing further evidence that no over-training occurred.  
 957 In Figure ??, normalised distributions of the signal and total background of the event-level BDT discriminator  
 958 output in the  $tWZ$  OF SR,  $tWZ$  SF SR and  $t\bar{t}Z$  CR, are shown.  
 959 The event-level BDT discriminates well between signal and background events in the  $tWZ$  OF SR,  $tWZ$  SF SR  
 960 and  $t\bar{t}Z$  CR, with separations of 8.98%, 10.6% and 20.6%, respectively.

## 962 4.8 Two Neutrino Scanning Method ( $2\nu$ SM) Algorithm

963 The Two Neutrino Scanning Method ( $2\nu$ SM) algorithm<sup>1</sup> [60, 59] aims to reconstruct  $t\bar{t}$  systems in the  $2\ell$ ,  $3\ell$  and  
 964  $4\ell$  final states (e.g.  $2\ell$  case:  $t\bar{t} \rightarrow \ell^+ \nu_\ell b\ell^- \bar{\nu}_\ell \bar{b}$ ). This was initially designed to suppress the  $t\bar{t}$  background in the  $t\bar{t}Z$   
 965 analysis. We can re-purpose this algorithm to distinguish between  $tWZ$  and  $t\bar{t}Z$  by removing the easily-identifiable  
 966  $Z$  boson.

967  
 1software tool and weights provided by Thomas McCarthy ( $t\bar{t}Z$  analysis group - Max Planck Institute)

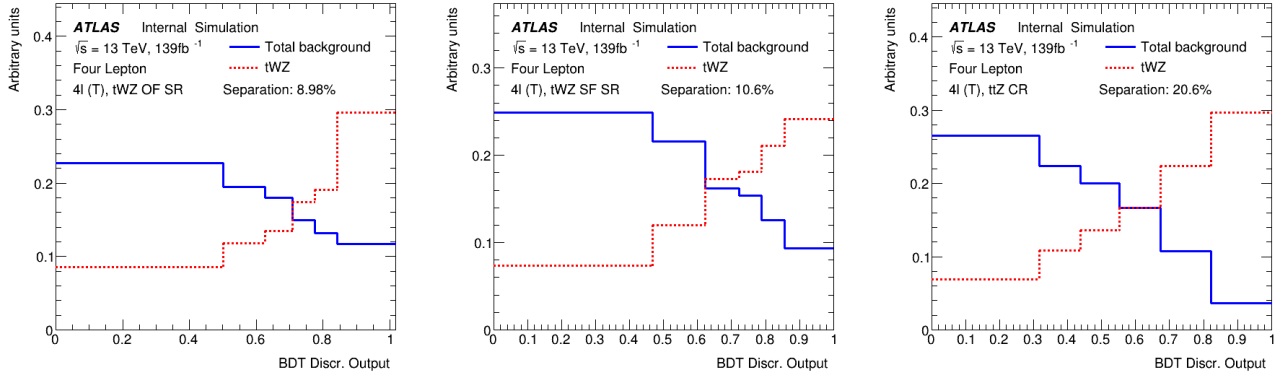


Figure 4.40: Normalised distributions of the signal and total background of the event-level BDT discriminator output in the  $tWZ$  OF SR,  $tWZ$  SF SR and  $t\bar{t}Z$  CR are shown (left to right). The dotted red and solid blue lines represent the distributions (normalised to an area of 1) of the signal and total background events respectively. The x-axis shows the event-level BDT discriminator output and the y-axis shows the relative number of events (in arbitrary units).

968 The  $2\nu$ SM algorithm reconstructs a  $t\bar{t}$  system by scanning through the components of two possible neutrino 4-  
 969 vectors ( $\nu_1$  and  $\nu_2$ ). It then aims to determine which  $\nu_1$  and  $\nu_2$  correspond to the two neutrinos which originate  
 970 from the decay of a  $t\bar{t}$  system the best (quantified by an output weight,  $w_{2\nu SM}$ ).  $w_{2\nu SM}$  is the likelihood under  
 971 the  $t\bar{t}$  dilipeton final state hypothesis. We are able to use this algorithm in our analysis to discriminate between  
 972  $tWZ$  and  $t\bar{t}Z$  since we can easily reconstruct the OSSF leptons which decay from the  $Z$  boson and remove it before  
 973 inputting the event into the algorithm. We would then expect that the  $2\nu$ SM algorithm returns a higher score from  
 974 a  $t\bar{t}Z$  event ( $\sim 1$ , i.e. it looks like a  $t\bar{t}$  event after removal of the  $Z$  boson) and a lower score from a  $tWZ$  event ( $\sim$   
 975 0, i.e. it does not look like a  $t\bar{t}$  event after removal of the  $Z$  boson).

#### 976 4.8.1 The algorithm

977 The  $2\nu$ SM algorithm starts off by writing down four equations which correspond to the invariant masses of the top  
 978 quark ( $m(t)$ ) and  $W$  boson ( $m(W)$ ) for the two top decays (i.e.  $t \rightarrow W^+ b \rightarrow \ell^+ \nu_\ell$ ) in a dileptonic  $t\bar{t}$  event. These  
 979 can be written as,

$$(\ell_1 + \nu_1)^2 = m(W)^2 = (80.385 \text{ GeV})^2 \quad (4.3)$$

$$(\ell_1 + \nu_1 + b_{1,2})^2 = m(t)^2 = (172.5 \text{ GeV})^2 \quad (4.4)$$

$$(\ell_2 + \nu_2)^2 = m(W)^2 = (80.385 \text{ GeV})^2 \quad (4.5)$$

$$(\ell_2 + \nu_2 + b_{2,1})^2 = m(t)^2 = (172.5 \text{ GeV})^2 \quad (4.6)$$

980 where the subscripts indicate that these particles originate from the decay of two different top quarks in a  $t\bar{t}$   
 981 system. We assume that the mass of the neutrinos ( $\nu_1$  and  $\nu_2$ ) are close to zero, which leaves us with 6 unknowns,  
 982  $p_{T\nu_1}$ ,  $\phi_{\nu_1}$ ,  $\eta_{\nu_1}$ ,  $p_{T\nu_2}$ ,  $\phi_{\nu_2}$  and  $\eta_{\nu_2}$  (components of the two neutrino's 4-vectors).

983 The  $2\nu$ SM algorithm takes the 4-vectors of the two reconstructed leptons (not from the  $Z$  boson) and the two jets  
 984 with the highest DL1r  $b$ -tagger score as input. For each neutrino ( $\nu_1$  and  $\nu_2$ ), we scan over a range of possible  $\eta$  and  
 985  $\phi$  values. These values were chosen to be  $\phi_{\nu_1}, \phi_{\nu_2} \in [-\pi, \pi]$  with a step size of  $\approx 0.25$  and  $\eta_{\nu_1}, \eta_{\nu_2} \in [-5, 5]$  with a  
 986 step size of  $\approx 0.31$ . These ranges were chosen to maximize accuracy and minimize computation time. For each of  
 987 these possible  $\eta$  and  $\phi$  values, we calculate the corresponding  $p_T$  for each neutrino. The transverse momentum of  
 988 a neutrino,  $p_{T\nu}$ , can be calculated via (\*\*\*\*\*referecne somewhere here\*\*\*\*\*),

$$p_{T\nu} = \frac{\frac{1}{2}(m(W)^2 - m(\ell)^2)}{E_\ell \cosh \eta_\nu - p_{\ell,z} \sinh \eta_\nu - p_{\ell,x} \cos \phi_\nu - p_{\ell,y} \sin \phi_\nu} \quad (4.7)$$

990 where  $E_\ell$  is the energy of the lepton and  $p_{\ell,z}$ ,  $p_{\ell,x}$ ,  $p_{\ell,y}$  are the  $z$ ,  $x$  and  $y$  components of lepton's momentum. At  
 991 this stage, we have possible 4-vectors for  $\nu_1$  and  $\nu_2$ . Using these possible neutrino 4-vectors, we reconstruct the two

992 possible  $t\bar{t}$  systems,

$$t_1 = \ell_1 + b_1 + \nu_1 \text{ and } t_2 = \ell_2 + b_2 + \nu_2 \quad (4.8)$$

**OR**

$$t_1 = \ell_1 + b_2 + \nu_1 \text{ and } t_2 = \ell_2 + b_1 + \nu_2 \quad (4.9)$$

993 These reconstructed  $t\bar{t}$  systems are then used to calculate a weight,  $w_{2\nu SM}$ . The  $w_{2\nu SM}$  weight (a value ranging  
994 from 0 to 1) is defined as a product of four probabilities (described below) and can be written as,

$$w_{2\nu SM} = P_{m_{t_1}} \times P_{m_{t_2}} \times P_{\Delta E_x} \times P_{\Delta E_y} \quad (4.10)$$

995 The  $w_{2\nu SM}$  is calculated for each pair of reconstructed neutrinos (or reconstructed  $t\bar{t}$  systems), with the maximum  
996 value being chosen as the final value for the event.

### 997 4.8.2 Calculating $w_{2\nu SM}$

998 We use distributions of well modelled observables ( $m_{b\ell\nu}$  and  $\Delta E_x$ ) from simulated  $t\bar{t}$  events in order to determine  
999 how well our reconstructed neutrinos (and in turn top quarks) resemble neutrinos (and top quarks) present in a  $t\bar{t}$   
1000 event.

#### 1001 4.8.2.1 $P_{m_{t_1}}$ and $P_{m_{t_2}}$

1002 A normalised distribution of the mass of reconstructed top quarks ( $m_{b\ell\nu}$ ) from a  $t\bar{t}$  sample is generated to  
1003 determine the probabilities  $P_{m_{t_1}}$  and  $P_{m_{t_2}}$ . The distribution is generated from reco-level leptons, generator-level  
1004 neutrinos and reoc-level jets matched in  $\Delta R$  to generator-level  $b$ -quarks, therefore only filling the distribution with  
1005 correct detector-level objects. We then use the distribution to interpolate our two reconstructed top quarks, which  
1006 returns a weight value from 0 to 1, with higher values corresponding to a reconstructed top quark which has a  
1007 mass close to that of a top quark from a  $t\bar{t}$  system. This interpolation is done for both reconstructed tops,  $t_1$  and  
1008  $t_2$ , corresponding to probabilities  $P_{m_{t_1}}$  and  $P_{m_{t_2}}$ . The distribution used is shown in Figure 4.41.

1009  
1010 In Figure 4.41, the  $m_{b\ell\nu}$  distribution (generated from simulated  $t\bar{t}$  events), used to calculate  $P_{m_{t_1}}$  and  $P_{m_{t_2}}$  is  
1011 shown.

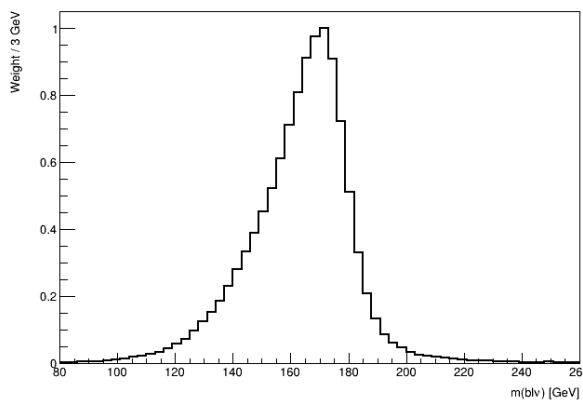


Figure 4.41:  $m_{b\ell\nu}$  distribution generated from simulated  $t\bar{t}$  events, used to calculate  $P_{m_{t_1}}$  and  $P_{m_{t_2}}$  is shown. The  $m_{b\ell\nu}$  distribution is shown by the black lined histogram. The mass of the  $b\ell\nu$  system is shown on the x-axis. The corresponding weight of the  $m_{b\ell\nu}$  distribution is shown on the y-axis.

#### 1012 4.8.2.2 $P_{\Delta E_x}$ and $P_{\Delta E_y}$

1013 A similar method is used to determine  $P_{\Delta E_x}$  and  $P_{\Delta E_y}$ . In this case we generate a weight distribution of  $\Delta E_x =$   
1014  $(p_{T,\nu_1})_x + (p_{T,\nu_2})_x - (E_T^{\text{miss}})_x$  based off simulated  $t\bar{t}$  events. In particular, this distribution is generated using reco-  
1015 level  $E_T^{\text{miss}}$  and generator-level neutrinos. The use of this distribution lies under the assumption that neutrinos are

the dominant source of  $E_T^{\text{miss}}$ , and therefore,  $(E_T^{\text{miss}})_x \approx (p_{T,\nu_1})_x + (p_{T,\nu_2})_x$  and  $(E_T^{\text{miss}})_y \approx (p_{T,\nu_1})_y + (p_{T,\nu_2})_y$ . We then use the distribution to interpolate the value of  $\Delta E_x$  and  $\Delta E_y$  from our reconstructed neutrinos. This returns a weight value from 0 to 1, with higher values corresponding to  $\Delta E_x$  and  $\Delta E_y$  (and in turn our reconstructed neutrino's  $p_T$ ) closer to those observed in a  $t\bar{t}$  event. We expect the  $\Delta E_x$  and  $\Delta E_y$  distributions to have the same shapes, therefore we only need to generate one (we have chosen  $\Delta E_x$ ). In Figure 4.42, the  $m_{b\ell\nu}$  distribution (generated from simulated  $t\bar{t}$  events), used to calculate  $P_{m_{t_1}}$  and  $P_{m_{t_2}}$  is shown.

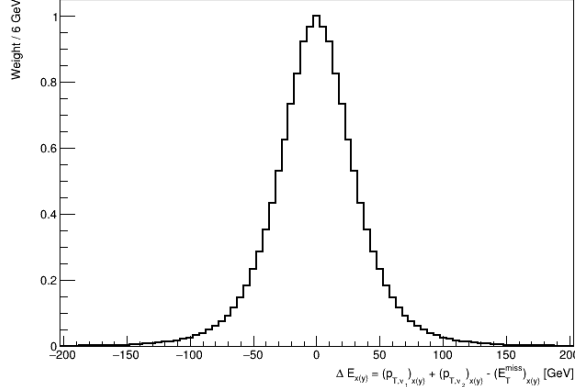


Figure 4.42:  $\Delta E_x$  distribution generated from simulated  $t\bar{t}$  events, used to calculate  $P_{\Delta E_x}$  and  $P_{\Delta E_y}$  is shown. The  $\Delta E_x$  distribution is shown by the black lined histogram.  $\Delta E_x$  is shown on the x-axis. The corresponding weight of  $\Delta E_x$  distribution is shown on the y-axis.

### 4.8.3 Kinematic Veto

The  $2\nu$ SM algorithm is extremely computationally intensive. The computation time depends on the number step size of the  $\phi$  and  $\eta$  ranges which we scan over to reconstruct the neutrinos. For example, consider the step sizes chosen in this analysis,  $\Delta\eta \approx 0.31$  and  $\Delta\phi \approx 0.25$  which corresponds to 32 values for  $\eta$  and 25 values for  $\phi$ . There will be  $(32)(32)(25) = 640\,000$  possible pairs of neutrinos ( $\nu_1$  and  $\nu_2$ ) to consider **per event**. Since we have to consider two possible  $t\bar{t}$  systems (See Equations 4.8 and 4.9), this number effectively increases to  $(2)(640\,000) = 128\,000$  iterations **per event**. In order to reduce the number of  $t\bar{t}$  systems we need to consider, therefore decreasing computation time, we look at distributions of well modelled observables from  $t\bar{t}$  events and veto (discard) a possible reconstructed  $t\bar{t}$  system if the observable in question is improbable or unlikely to be observed in a  $t\bar{t}$  event. To achieve this, we define a threshold range for these observables (See Figure 4.45 and Figure 4.47), and if the possible reconstructed  $t\bar{t}$  system's corresponding value for this observable lies outside this range, it is vetoed and the algorithm continues with the next iteration.

#### 4.8.3.1 $\Delta\langle m(\ell b) \rangle$

The first observable which we consider is the difference between average mass of the two possible  $\ell b$  system combinations,  $\Delta\langle m(\ell b) \rangle$ . The two possible  $\ell b$  system combinations are,

$$(\ell b)_1 = \ell_1 + b_1 \text{ and } (\ell b)_2 = \ell_2 + b_2 \quad (4.11)$$

**OR**

$$(\ell b)_1 = \ell_1 + b_2 \text{ and } (\ell b)_2 = \ell_2 + b_1 \quad (4.12)$$

$$(4.13)$$

$\Delta\langle m(\ell b) \rangle$  is therefore defined as,

$$\Delta\langle m(\ell b) \rangle = \frac{1}{2} |[(m(\ell_1 b_1) + m(\ell_1 b_1)) - (m(\ell_2 b_2) + m(\ell_2 b_1))]| \quad (4.14)$$

The idea here is that, if  $\Delta\langle m(\ell b) \rangle$  is large, it's more likely that we can simply select the  $\ell b$  combination with the smaller (minimum) average mass. To illustrate this, we look at the distribution (constructed from  $t\bar{t}$  events) of  $P(\text{Correct combination of } \ell b \text{ systems} | \text{minimum}\langle m(\ell b) \rangle)$  vs  $\Delta\langle m(\ell b) \rangle$  for  $b$ -tagged jets in the same ( $\eta(b_1) \times \eta(b_2) \geq 0$ )

1041 and opposite hemispheres ( $\eta(b_1) \times \eta(b_2) < 0$ ).

1042 In Figure 4.43 the  $P(\text{Correct combination of } \ell b \text{ systems} | \text{minimum}\langle m(\ell b) \rangle)$  vs  $\Delta\langle m(\ell b) \rangle$ , for  $b$ -tagged jets in the same and opposite hemispheres, constructed from  $t\bar{t}$  events is shown.

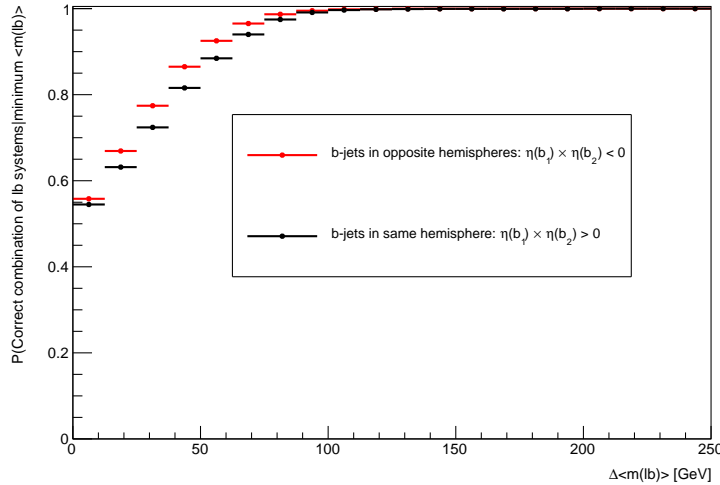


Figure 4.43:  $P(\text{Correct combination of } \ell b \text{ systems} | \text{minimum}\langle m(\ell b) \rangle)$  vs  $\Delta\langle m(\ell b) \rangle$ , for  $b$ -tagged jets in the same and opposite hemispheres, constructed from  $t\bar{t}$  events is shown. The horizontal red lines represent the distribution in the case when the two  $b$ -jets are in opposite hemispheres. The dot in the middle of the line represents the midpoint of the line. The horizontal black lines represent the distribution in the case when the two  $b$ -jets are in the same hemispheres. The dot in the middle of the line represents the midpoint of the line. The average  $m(\ell b)$  is shown on the x-axis. The  $P(\text{Correct combination of } \ell b \text{ systems} | \text{minimum}\langle m(\ell b) \rangle)$  is shown on the y-axis.

1043 From Figure 4.43, for both cases where the  $b$ -tagged jets are in the same and opposite hemispheres, the  
 1044 probability for a correct  $\ell b$  system being chosen given that we are considering the  $\ell b$  system with  
 1045 minimum average mass is an increasing function which plateaus to 1 at  $\sim 90$  GeV. We use these two distribu-  
 1046 tions to interpolate the  $P(\text{Correct combination of } \ell b \text{ systems} | \text{minimum}\langle m(\ell b) \rangle)$  from  $\Delta\langle m(\ell b) \rangle$ . We require that  
 1047  $P(\text{Correct combination of } \ell b \text{ systems} | \text{minimum}\langle m(\ell b) \rangle) > 0.8$ , before vetoing any  $\ell b$  combination, such that we  
 1048 have are at least 80% certain that we know the correct  $\ell b$  combination. In this case, the  $\ell b$  combination with the  
 1049 maximum  $\Delta\langle m(\ell b) \rangle$  is vetoed. If  $P(\text{Correct combination of } \ell b \text{ systems} | \text{minimum}\langle m(\ell b) \rangle) < 0.8$  we need to consider  
 1050 both possible  $\ell b$  system combinations.  
 1051

#### 1052 4.8.3.2 $\eta(b\bar{b}\ell\ell)$

1053 We consider  $\eta$  of the  $b\bar{b}\ell\ell$  system,  $\eta(b\bar{b}\ell\ell)$  to veto improbable  $\eta(\nu_1)$  and  $\eta(\nu_2)$  values.

1054  
 1055 In the same way as for  $\Delta\langle m(\ell b) \rangle$ , we generate a distribution to determine values  $\eta(\nu)$  which are improbable for a  $t\bar{t}$   
 1056 event. In this case, we generate a 2D histogram from simulated  $t\bar{t}$  events (dileptonic final state) at generator-level  
 1057 of  $\eta(\nu)$  vs  $\eta(b\bar{b}\ell\ell)$ .

1058 In Figure 4.44, a heatmap of occupancy for  $\eta(\nu)$  vs  $\eta(b\bar{b}\ell\ell)$  (produced from simulated  $t\bar{t}$  events) is shown.  
 1059 Using the above heatmap, we define a veto region (where a  $t\bar{t}$  event is extremely unlikely to occur) based off  
 1060 double-sided 95% limits (\*\*something here on confidence limit??\*\*). We apply a veto if either possible neutrino  
 1061 lies within this region. The veto region is shown in Figure 4.45.

1063  
 1064 In Figure 4.45, the veto region (extracted from Figure 4.44) for vetoing improbable neutrinos is shown.

#### 1065 4.8.3.3 $L_T$

1066 The final kinematic constraint which we consider is the scalar sum of lepton  $p_T$ ,  $L_T = p_T(\ell_1) + p_T(\ell_2)$  which we  
 1067 use to veto certain possible neutrinos,  $\nu_1$  and  $\nu_2$ .

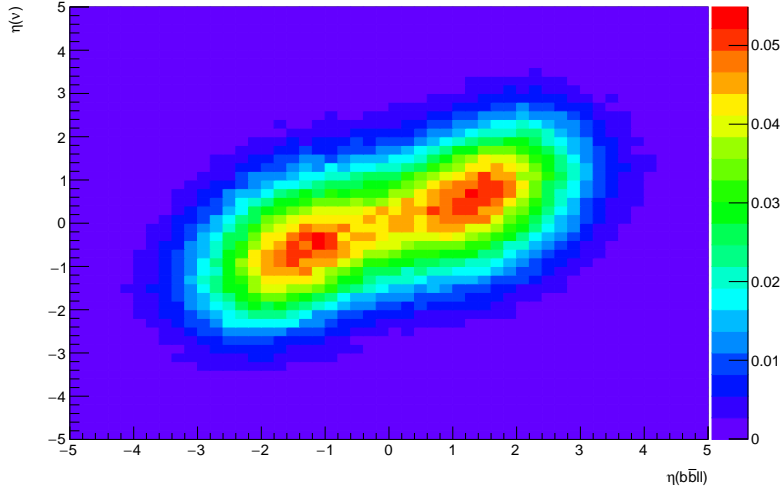


Figure 4.44: Heatmap of occupancy for  $\eta(\nu)$  vs  $\eta(b\bar{b}\ell\ell)$  produced from simulated  $t\bar{t}$  events (dileptonic final state) at generator-level is shown.  $\eta$  of the  $b\bar{b}\ell\ell$  system is shown on the x-axis.  $\eta$  of the neutrino is shown on the y-axis. The colorbar on the right represents the occupancy (normalised) in the phase space.

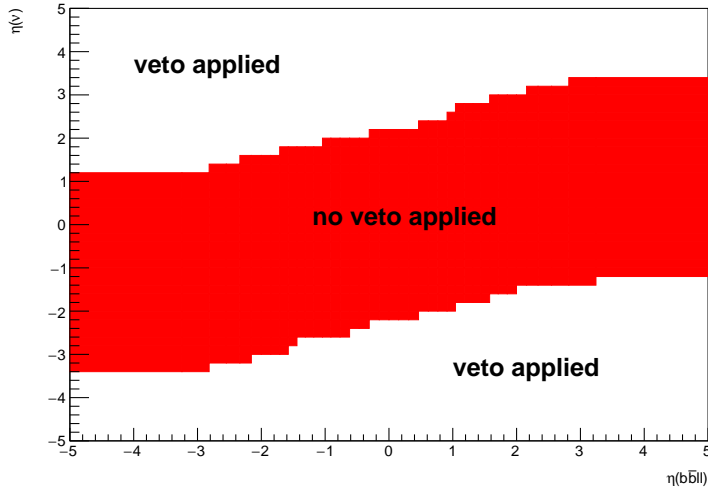


Figure 4.45: The regions where vetoes are applied for the  $\eta(b_1 b_2 \ell_1 \ell_2)$  constraint is shown.  $\eta$  of the  $b\bar{b}\ell\ell$  system is shown on the x-axis.  $\eta$  of the neutrino is shown on the y-axis. The red band shows the region where the neutrino would not be vetoed. The white areas (above and below the red band) are regions where the neutrino is vetoed.

1069 Again, we generate a distribution to determine (and veto) improbable possible neutrinos in simulated  $t\bar{t}$  events  
 1070 (dilepton final state).

1071 In Figure 4.46, a heatmap of occupancy for  $\Delta R(\ell, \nu)$  vs  $L_T$  (produced from simulated  $t\bar{t}$  events) is shown.

1072 Using the same method as described in Section 4.8.3.2, we define a veto region where a veto is applied if either  
 1073 possible neutrino lies within this region. In Figure 4.45, the veto region (extracted from Figure 4.46) for vetoing  
 1074 improbable neutrinos values is shown.

## 1075 4.9 Systematics

1076 The systematic uncertainties can be separated into experimental (detector) systematics, which are related to the  
 1077 reconstruction of physics objects in the detector and theoretical uncertainties related to the modelling of the different  
 1078 processes background.

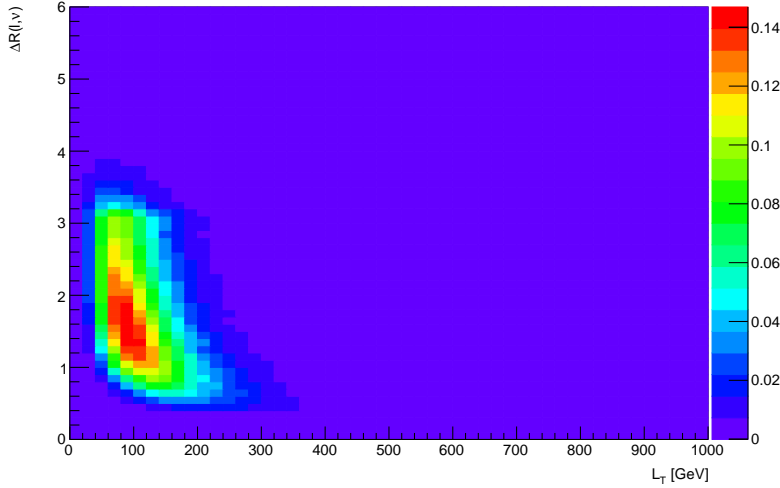


Figure 4.46: A heatmap of occupancy for  $\Delta R(\ell, \nu)$  vs  $L_T$  produced from simulated  $t\bar{t}$  events (dileptonic final state) at generator-level is shown.  $\Delta R$  between leptons and neutrinos is shown on the x-axis.  $L_T$  (scalar sum of lepton  $p_T$ ) is shown on the y-axis. The colorbar on the right represents the occupancy (normalised) in the phase space.

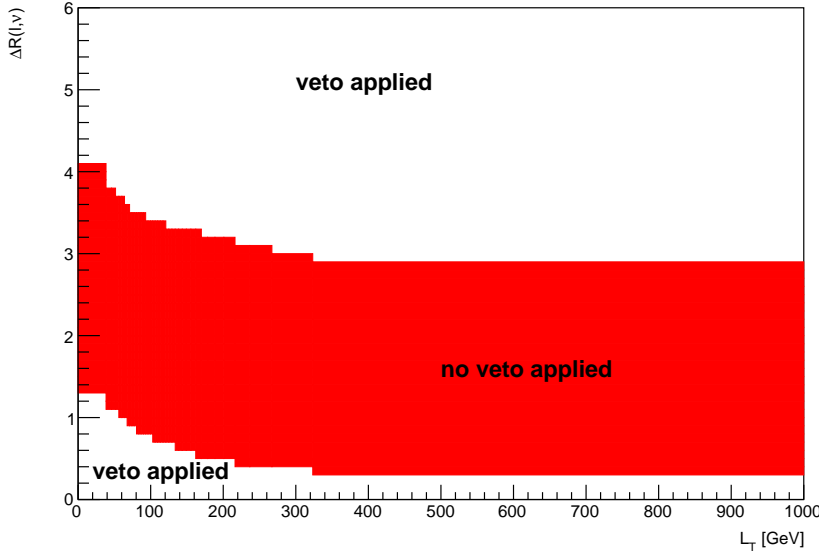


Figure 4.47: The regions where vetoes are applied for the  $L_T$  constraint is shown.  $\Delta R$  between leptons and neutrinos is shown on the x-axis.  $L_T$  (scalar sum of lepton  $p_T$ ) is shown on the y-axis. The red band shows the region where the neutrino would not be vetoed. The white areas (above and below the red band) are regions where the neutrino is vetoed.

#### <sup>1079</sup> 4.9.1 Experimental uncertainties

<sup>1080</sup> In this section, the experimental systematics are outlined.

- <sup>1081</sup> • **Luminosity:**

<sup>1082</sup> The 2015–2018 luminosity estimate of  $139\text{fb}^{-1}$  has a relative uncertainty of 3%. This uncertainty is obtained  
<sup>1083</sup> using the LUCID-2 detector [23] for the primary luminosity measurements. This systematic uncertainty affects  
<sup>1084</sup> all processes modelled using MC simulations.

- <sup>1085</sup> • **Pile-up reweighting:**

1086 An uncertainty related to the SFs used for MC to account for differences in pile-up distributions between  
 1087 MC and data is applied. This uncertainty is obtained by re-scaling the  $\langle \mu \rangle$  value in data by 1.00 and 1/1.18  
 1088 corrections are only applied to MC.

- 1089 • **Jet vertex tagger:**

1090 Uncertainties associated to the *JVT* are applied via the `JetJvtEfficiency` package [21] which account for  
 1091 the residual contamination from pile-up jets after pile-up suppression and the MC generator choice [14].

- 1092 • **Heavy- and light-flavor tagging:**

1093 The efficiency of the flavour-tagging algorithm is measured for each jet flavour using control samples in data  
 1094 and in simulation. From these measurements, correction factors are derived to correct the tagging rates in the  
 1095 simulation. In the case of  $b$ -tagged jets, the correction factors and their uncertainties are estimated from data  
 1096 using dileptonic  $t\bar{t}$  events [16, 11]. In the case of  $c$ -jets, they are derived from jets arising from  $W$  boson decays  
 1097 in  $t\bar{t}$  events [15]. In the case of light-flavour jets, the correction factors are derived using dijet events [12].  
 1098 Sources of uncertainty affecting the  $b$ - and  $c$ -tagging efficiencies are evaluated as a function of jet  $p_T$ , including  
 1099 bin-to-bin correlations. The uncertainties in the efficiency for tagging light-flavour jets depend on the jet  $p_T$   
 1100 and on  $\eta$ . An additional uncertainty is assigned to account for the extrapolation of the  $b$ -tagging efficiency  
 1101 measurement from the  $p_T$  region used to determine the correction factors to regions with higher  $p_T$ .

- 1102 • **Electron efficiency:**

1103 Uncertainties associated with the electron efficiency SFs are provided by the egamma CP group [19] and  
 1104 arise from the reconstruction, ID, isolation and trigger efficiencies. They correct for the efficiency difference  
 1105 between data and MC [13] and are measured with a “tag-and-probe” method in  $Z \rightarrow e^+e^-$  and  $J/\psi \rightarrow e^+e^-$   
 1106 events. The information on the correlation of the different components of the systematic uncertainties are  
 1107 provided for all efficiency measurements. The default correlation model for the uncertainties is used, which  
 1108 provides one up/down variation for each of the SF components separately [19, 20].

- 1109 • **Muon efficiency:**

1110 As for electrons, SFs obtained from  $Z \rightarrow \mu^+\mu^-$  and  $J/\psi \rightarrow \mu^+\mu^-$  events are applied to correct for the  
 1111 differences between data and MC in the muon ID, isolation and trigger efficiencies [17]. Uncertainties on these  
 1112 SFs are provided by the muon CP group [22] and applied as up/down variations of the nominal SFs for each  
 1113 component.

#### 1114 4.9.2 Theoretical uncertainties

1115 In this section, the theoretical systematics are outlined.

- 1116 •  **$t\bar{t}Z$  background:**

1117 An overall normalization uncertainty of 10% is considered for the  $t\bar{t}Z$  background. Two generic shape sys-  
 1118 tematics are considered for the  $t\bar{t}Z$  background. They are constructed (see Section 4.9.3) by either applying a  
 1119 linear or triangular interpolation to up and down variations which are defined to be  $\pm 20\%$  from the nominal  
 1120  $t\bar{t}Z$  background.

- 1121 •  **$ZZ$  background:**

1122 An overall normalization uncertainty of 30% is considered for the  $ZZ$  background.

- 1123 •  **$t\bar{t}H$  background:**

1124 An overall normalization uncertainty of 20% is considered for the  $t\bar{t}H$  background.

- 1125 •  **$tZq$  background:**

1126 An overall normalization uncertainty of 14% is considered for the  $tZq$  background.

- 1127 •  **$t\bar{t}Z$  fake background:**

1128 An overall normalization uncertainty of 50% is considered for the  $t\bar{t}Z$  fake background.

1129 • **other background processes:**

1130 The 'other' background consists of many processes which have minimal but non-negligible contribution in  
 1131 the signal regions (See Table 4.4). An overall normalization uncertainty of 30% is considered for the 'other'  
 1132 background processes.

1133 •  **$tWZ$ :** A modelling uncertainty on  $tWZ$  is considered by comparing the nominal sample (using the DR1  
 1134 scheme) and a minimal DR2 sample.

1135 Two generic shape systematics are considered for the  $tWZ$  background. They are constructed (see Sec-  
 1136 tion 4.9.3) by either applying a linear or triangular interpolation to up and down variations which are defined  
 1137 to be  $\pm 20\%$  from the nominal  $tWZ$  background.

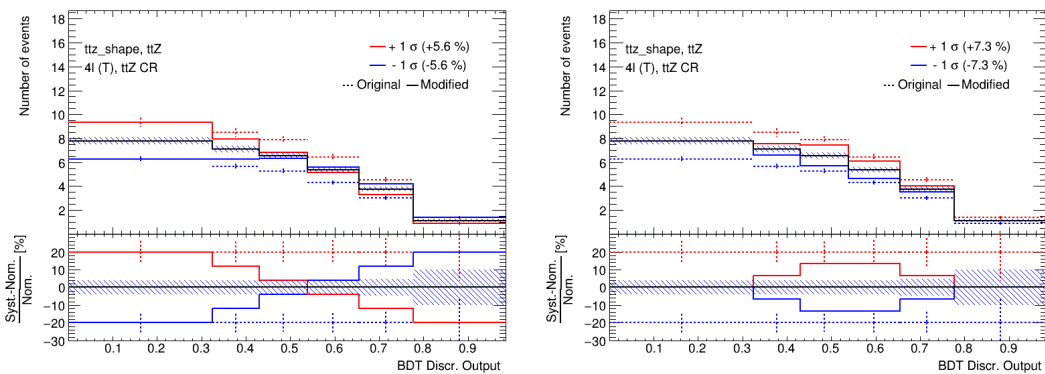
1138 **4.9.3 Generic shape systematics**

1139 It is evident that the tetralepton channel is statistically limited. We therefore expect that the uncertainty on  $u_{tWZ}$   
 1140 is dominated by statistical uncertainty and that the impact of shape systematics will be negligible in comparison.

1141 In order to include shape uncertainties related to the modelling of our samples, we construct generic shape  
 1142 systematics for any given sample process. Given that we choose a sufficiently large set of values for which the  
 1143 systematics can take in the fit, the constructed systematics could represent many shape systematics which we have  
 1144 not yet considered to include in the fitting procedure.

1145 We start by constructing an envelope (error bars) consisting of two MC templates. One with the nominal MC  
 1146 template increased by 20% on its normalisation and the other with the nominal MC template decreased by 20% on  
 1147 its normalisation. The templates are then modified from their original shape either by doing linear interpolation  
 1148 (from the leftmost-up variation to the rightmost-down variation) or triangular interpolation (shape is set to zero at  
 1149 the rightmost and leftmost parts and reaches the envelope in the middle). The linear and triangular interpolation is  
 1150 done using TRF's ForceShape option [68], which alters the original templates (as described above). This envelope  
 1151 now represents the bounds which the systematic can vary in the fit.

1152 In Figure 4.48 the envelope before and after the shape change, for both the linear and triangular interpolations, for  
 1153 the  $t\bar{t}Z$  background in the  $t\bar{t}Z$  CR is shown.



1154 Figure 4.48:  $t\bar{t}Z$  generic shape systematic before (original) and after (modified) linear (left) and triangular (right)  
 1155 interpolation in the  $t\bar{t}Z$  CR is shown. The output from the event-level BDT shown on the x-axis. In the upper panel,  
 1156 the number of events is shown on the y-axis. In the lower panel, the difference between the systematic variation  
 (the envelope's templates) and the nominal template, divided by the nominal template, is shown on the y-axis.  
 The nominal  $t\bar{t}Z$  template is shown by the solid black lined histogram, with the diagonal lined bands representing  
 its total uncertainty. The templates of the upper and lower envelopes (before modification) is given by the dotted  
 red and blue lined histograms respectively. The templates of the upper and lower envelopes (after modification) is  
 given by the solid red and blue lined histograms respectively, with the vertical dotted lines representing its total  
 uncertainty.

1157 We consider two shape systematics (linear and triangular shapes) for  $tWZ$  and the most dominant background  
 1158 processes across both channels. In particular, we consider these shape systematics for  $t\bar{t}Z$  for both the tri- and

1159 tetralepton channels. Additionally, we consider these shape systematics for the  $WZ + b$  and  $WZ + c$  backgrounds  
1160 in the trilepton channel.

## 1161 4.10 Analysis Pipeline and TRexFitter

1162 We make use of industry standard **ROOT**<sup>2</sup> wrappers in this analysis, namely, **PyROOT** and **TRexFitter**.

1163

1164 **Python** is used extensively in many fields of science (not limited to physics and data science) due to its simplicity  
1165 and ongoing support by the communities which utilize it. **PyROOT** allows users to access the full **ROOT** functionality  
1166 within **Python**. More specifically, **PyROOT** provides **Python** bindings for **ROOT**.

1167

1168 **TRexFitter** is a framework for binned template profile likelihood fits[79]. In this analysis, we used **TRexFitter**  
1169 (tag: **TRexFitter-00-04-13**) to produce all pre-fit and post-fit plots (including fit statistics, e.g. limit, significance,  
1170  $\mu_{best-fit}$ ).

1171

1172 The analysis pipeline starts with sample derivations (derived dataset) being submitted to the grid for ntuple  
1173 production. This applies cuts and selections to the already reduced derivations and produces ntuples with trees  
1174 containing variables (e.g. scale factors, observables, MC truth flags) that will be used at future stages in the analysis.  
1175 These ntuples are then read by **PyROOT** where the events are looped over, before being written to **ROOT** files as input  
1176 to **TRexFitter**. The **Python** scripts are used to define the different regions and apply the final cuts and selections  
1177 outlined in Table 4.3. In addition to this purpose, they are used to train the two BDTs and to produce the output  
1178 from these trained BDTs. As each event is looped over, the cuts and selection criteria are checked for the given  
1179 event and is either thrown away (if the event does not pass the selection criteria), or gets written to a **ROOT** file (if  
1180 the event passes the selection criteria) corresponding to the MC sample and Run 2 data-set which it belongs to.  
1181 These **ROOT** files contain all observables, weights and scale factors (corresponding to an event) which we wish to use  
1182 in **TRexFitter**. **TRexFitter** then takes these files as input, runs a maximum likelihood fit and produces relevant  
1183 plots (e.g. pre-fit, post-fit, pull plots) and statistical parameters (e.g. limit, significance,  $\mu_{best-fit}$ ).

### 1184 4.10.1 Fitting Procedure

1185 Using the **TRexFitter** framework, binned profile-likelihood fits are performed to determine the signal strength,  
1186  $\mu_{tWZ} = \frac{\sigma_{obs}(tWZ)}{\sigma_{SM}(tWZ)}$ , of  $tWZ$  production. A fit across all regions in the tetralepton channel is performed to determine  
1187 the sensitivity  $tWZ$  in this channel. In Section 4.11.2, a combined fit is performed across all regions in the trilepton  
1188 and tetralepton channels to take advantage of the sensitivity of  $tWZ$  in both channels in order to further boost  
1189 the sensitivity of  $tWZ$ .

1190

1191 To characterise the sensitivity and associated uncertainty of our measurement of  $\mu(tWZ)$ , we compute two metrics:  
1192 the expected significance ( $Z_\mu^{exp}$ ) and the expected upper limit ( $\mu_{up}^{exp}$ ). In this context, the expected significance  
1193 can be interpreted as, the probability that the measured signal is due to a background fluctuation. Larger values  
1194 indicate lower probabilities and smaller values indicate higher probabilities. Particle physicists have adopted a  
1195 standard to define the sensitivity necessary for evidence and discovery of a particular particle or phenomena. A  
1196  $3\sigma$  (corresponding to a background fluctuation probability of  $\approx 10^{-3}$ ) significance is considered to be evidence  
1197 for observation and a  $5\sigma$  (corresponding to a background fluctuation probability of  $\approx 10^{-7}$ ) is considered to be  
1198 a discovery. The expected upper limit is a single-sided interval test statistic, associated with the POI in the  
1199 maximum-likelihood fit ( $\mu(tWZ)$ , in our case). In this context, the expected upper limit can be understood in the  
1200 following way: consider running an ensemble of MC toy experiments, each with their own confidence interval (a  
1201 range of possible values for  $\mu(tWZ)$ ). An expected upper limit, at some fixed percentage  $x\%$  (or *confidence level*),  
1202 can be determined from this ensemble. The expected upper limit tells us that,  $x\%$  of the toy MC experiment's  
1203 confidence intervals will contain the true value of  $\mu(tWZ)$ . A commonly used percentage in particle physics is  
1204 95%, which we adopt for this analysis. In particle physics, this is referred to as the *CLs Method* [39]. The CLs  
1205 test statistic can be calculated 'brute force' by running these MC toy experiments, however this is very CPU  
1206 intensive. Asymptotic formulae are able to describe the underlining CLs test statistic distributions under certain  
1207 approximations [9]. Instead of running toy MC experiments, we use asymptotic formulae to perform the CLs  
1208 method, which reduces computation time from several millions of CPU hours to several CPU minutes. The

<sup>2</sup>CERN's HEP data analysis framework (written in C++)

significance and upper limits which are calculated in this analysis are given a prefix of 'expected' to indicate that these are results from a blinded analysis.

In the separate and combined fits, the *mixed data and MC* fit setup [80] is used. This is done to obtain the most accurate prediction of the expected results while keeping the signal regions blinded. For this setup, first a background-only fit to the control regions using real data is done to determine estimates of the nuisance parameters. Then these estimates are used to construct a modified ASIMOV dataset in the signal regions. Finally, the fit is performed using real data in the control regions and the aforementioned modified ASIMOV data-set in the signal regions.

In these fits, the parameter of interest (POI) is  $\mu_{tWZ}$ . The POI is ultimately the quantity which we wish to measure and is set as a free parameter (unconstrained; can take any value in the fit). The nuisance parameters are assigned to the systematic uncertainties outlined in Section 4.9. Furthermore, a gamma ( $\gamma$ ) nuisance parameter for a bin is added to the likelihood function if the statistical uncertainty in the bin exceeds 0.1% of its nominal value.

Pruning is done per sample and per region on the shape and normalisation uncertainties for samples. A sample's shape and normalisation nuisance parameter is pruned (removed from the limit/fit) if the fraction of signal yield to the total yield (signal + background) is less than 0.01.

An auto-binning algorithm, `TransfoD` [29], was used to define the binning. This aims to maximise  $\frac{\text{signal}}{\text{background}}$  in each bin. Furthermore, it aims to avoid defining bins with a low number of events.

## 4.11 Results

In the section, an expected upper limit and an expected significance are set on the cross section of  $tWZ$ . This is performed for the current analysis in the tetralepton channel as well as for a combined analysis across the trilepton and tetralepton channels. The trilepton analysis was performed as an independent study by Benjamin Warren (UCT) [81]. Note that throughout this section, all signal regions remain blinded.

### 4.11.1 Tetralepton Channel

In Figure 4.49 pre-fit distributions for the variables used in the likelihood fit in each region are shown.

In Figure 4.50 pre-fit distributions for the variables used in the likelihood fit in each region are shown.

In Table 4.10, the post-fit yields for each sample in each region is shown.

	$tWZ$ OF SR	$tWZ$ SF SR	$t\bar{t}Z$ CR	$ZZb$ CR	$(tWZ)_{\text{fake}}$ CR
$t\bar{t}Z$	$13.2379 \pm 1.52295$	$9.62061 \pm 1.12291$	$29.9054 \pm 3.60908$	$5.08899 \pm 0.620121$	$18.5393 \pm 2.23036$
$t\bar{t}Z$ fakes	$0.0702522 \pm 0.0468691$	$0.0334067 \pm 0.0256903$	$0.0723509 \pm 0.0418526$	$0.0485273 \pm 0.029133$	$5.04378 \pm 2.34732$
$tWZ$	$7.83414 \pm 3.31679$	$5.33547 \pm 2.24801$	$5.69373 \pm 2.58041$	$2.89889 \pm 1.23837$	$10.278 \pm 4.3345$
$ZZ$	$0.481776 \pm 0.119774$	$7.72372 \pm 1.2351$	$1.07955 \pm 0.182461$	$40.6067 \pm 6.26078$	$6.86097 \pm 1.11443$
other	$t\bar{t}$	$6.00553e-06 \pm 3.02819e-06$	$0.252557 \pm 0.442116$	$0.273507 \pm 0.223201$	$6.00553e-06 \pm 3.02819e-06$
	$tZq$	$0.0827905 \pm 0.0398773$	$0.0756107 \pm 0.0354584$	$0.063585 \pm 0.0293325$	$0.05884 \pm 0.0244084$
	$t\bar{t}W$	$0.00668643 \pm 0.00792217$	$0.00279748 \pm 0.00287361$	$6.00553e-06 \pm 3.02819e-06$	$0.002306 \pm 0.00564349$
	$WZ$	$0.0442934 \pm 0.024156$	$0.0396511 \pm 0.0154282$	$0.0133471 \pm 0.0128199$	$0.0472562 \pm 0.0330315$
	$t\bar{t}t$	$0.000987164 \pm 0.000766266$	$0.00247481 \pm 0.00136945$	$0.01040869 \pm 0.00479496$	$6.00553e-06 \pm 3.02819e-06$
	$t\bar{t}\bar{t}$	$0.00934035 \pm 0.0080554$	$0.0107458 \pm 0.00849984$	$0.0571373 \pm 0.0204011$	$6.00553e-06 \pm 3.02819e-06$
	$t\bar{t}WW$	$0.0294618 \pm 0.0263174$	$0.029771 \pm 0.0195582$	$0.264364 \pm 0.0926252$	$0.0129431 \pm 0.0323803$
	$VVV(V = W/Z)$	$0.280643 \pm 0.0853411$	$0.191433 \pm 0.0586778$	$0.0697266 \pm 0.0225059$	$0.171142 \pm 0.0518102$
	$t\bar{t}H$	$0.846054 \pm 0.175495$	$0.669375 \pm 0.140107$	$1.96662 \pm 0.401199$	$0.150025 \pm 0.0353826$
Total	$22.9243 \pm 2.96284$	$23.9876 \pm 2.11249$	$39.4734 \pm 3.44937$	$49.0856 \pm 6.04162$	$53.4282 \pm 4.31683$
data	-	-	36	49	57

Table 4.10: The post-fit yields for each sample in each region is shown.

The expected upper limit of  $tWZ$  in the tetralepton channel is measured as,

$$\mu_{up}^{exp} = 1.61^{+2.35}_{-1.16} \quad (4.15)$$

The expected significance of  $tWZ$  in the tetralepton channel is measured as,

$$Z_\mu^{exp} = 1.44\sigma \quad (4.16)$$

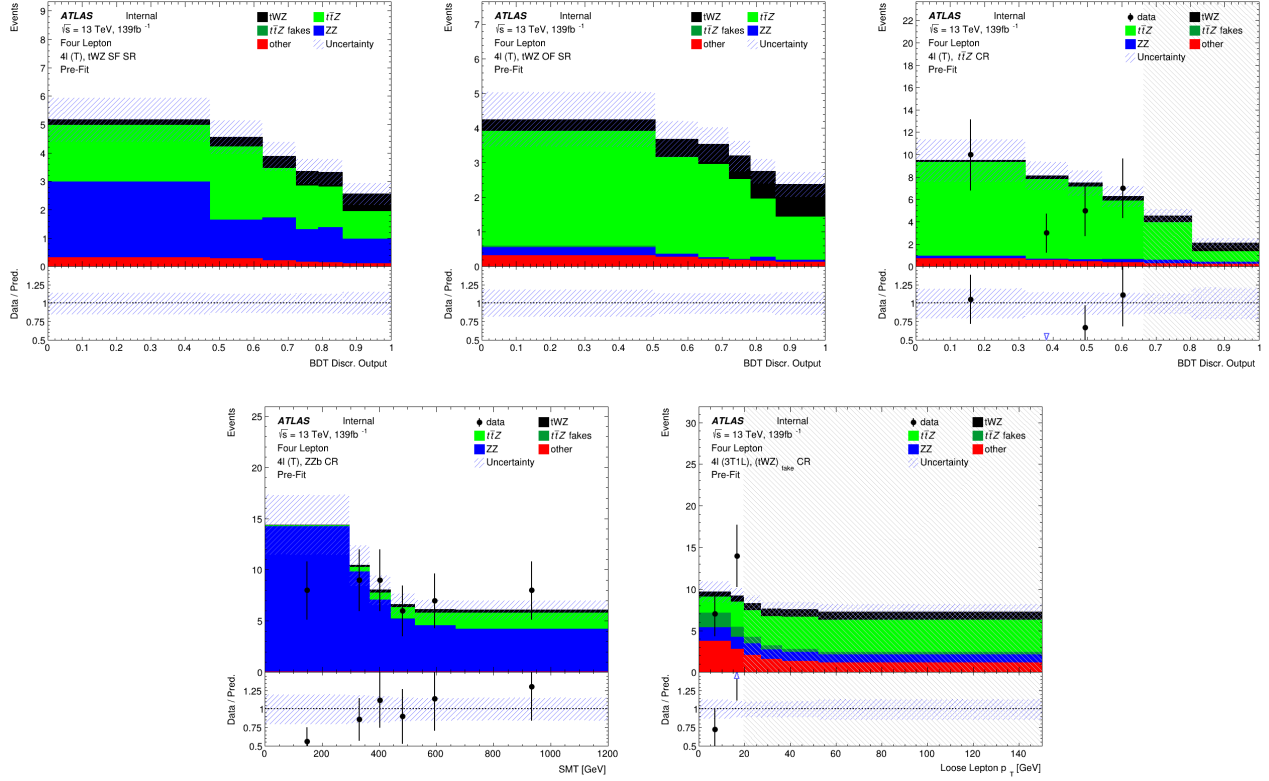


Figure 4.49: Pre-fit distributions (blinded) of variables used in the fit are shown. The data is given by the black points and the MC predictions for each process are given by the histograms. The vertical lines on the data points represent the statistical uncertainty in the data and the diagonally-lined bands represent the total (statistical and systematic added in quadrature) uncertainty. The lower panel in each plot shows the ratios of the data to the theoretical predictions. The plots in the  $tWZ$  OF SR and  $tWZ$  SF SR are kept blinded by omitting the data points. **Top left:** The event-level BDT Disc. Output in the  $tWZ$  SF (4T) SR region is shown. **Middle Top:** The event-level BDT Disc. Output in the  $tWZ$  SF (4T) SR region is shown. **Top right:** The event-level BDT Disc. Output in the  $t\bar{t}Z$  CR region is shown. **Bottom left:**  $SMT = \sum p_T(\ell) + \sum p_T(jet) + E_T^{\text{miss}}$  in the  $ZZb$  CR is shown. **Bottom right:**  $p_T$ (loose lepton) in the  $(tWZ)$ fake (3T1L) CR is shown.

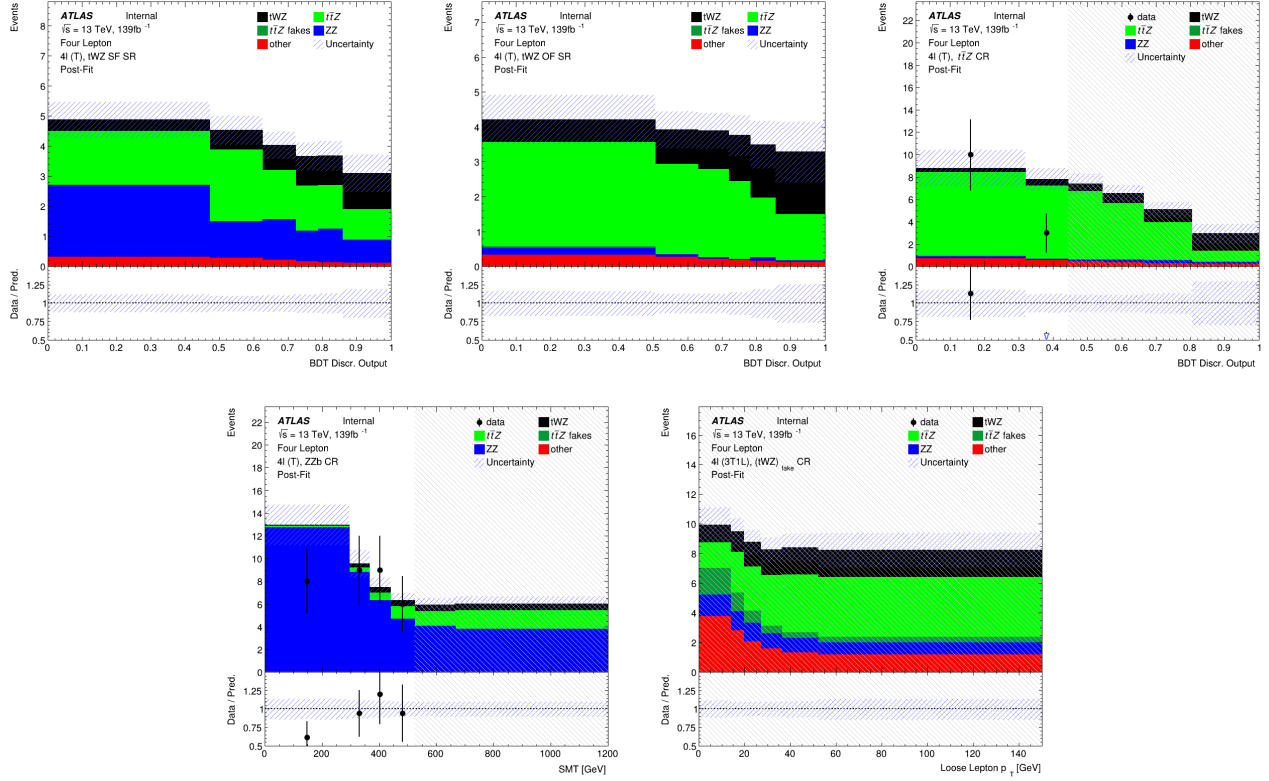


Figure 4.50: Post-fit distributions (blinded) of variables used in the fit are shown. The data is given by the black points and the MC predictions for each process are given by the histograms. The vertical lines on the data points represent the statistical uncertainty in the data and the diagonally-lined bands represent the total (statistical and systematic added in quadrature) uncertainty. The lower panel in each plot shows the ratios of the data to the theoretical predictions. The plots in the  $tWZ$  OF SR and  $tWZ$  SF SR are kept blinded by omitting the data points. **Top left:** The event-level BDT Disc. Output in the  $tWZ$  SF (4T) SR region is shown. **Middle Top:** The event-level BDT Disc. Output in the  $tWZ$  SF (4T) SR region is shown. **Top right:** The event-level BDT Disc. Output in the  $t\bar{t}Z$  CR region is shown. **Bottom left:**  $SMT = \sum p_T(\ell) + \sum p_T(jet) + E_T^{\text{miss}}$  in the  $ZZb$  CR is shown. **Bottom right:**  $p_T$ (loose lepton) in the  $(tWZ)$ fake (3T1L) CR is shown.

1241 The best-fit value of the signal strength,  $\mu(tWZ) = \frac{\sigma(tWZ)}{\sigma(tWZ)_{SM}}$ , from the likelihood fit is measured as,

$$\mu(tWZ) = 1.91^{+0.95}_{-0.82} \quad (4.17)$$

1242 The expected upper limit is in agreement with the extracted best-fit value on the signal strength, therefore no  
 1243 deviations from the SM cross section of  $tWZ$  is observed. Neither the  $3\sigma$  evidence nor the  $5\sigma$  discovery standards  
 1244 are reached for the expected significance. This is not surprising, given the low amount of events present in the  
 1245 tetralepton channel.

1246 In Figure 4.51, a ranking plot showing the impact of the systematic uncertainties on the POI,  $\mu(tWZ)$  is shown.

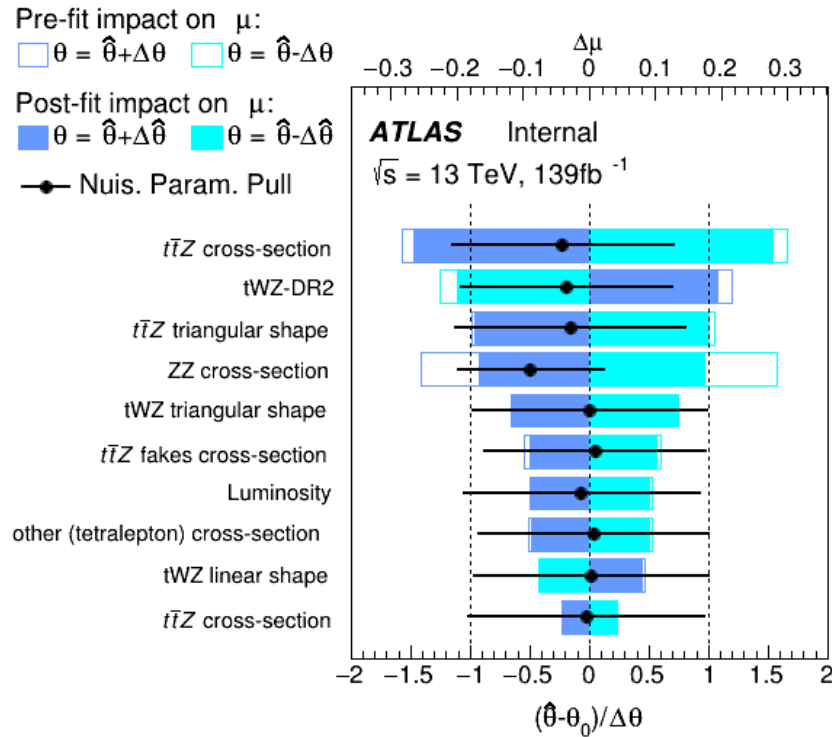


Figure 4.51: A ranking plot showing the impact (ordered from top to bottom via decreasing impact) of the systematic uncertainties (top 10) on the POI,  $\mu(tWZ)$ , in the tetralepton channel is shown.  $\hat{\theta}$  is the best-fit value of the nuisance parameter.  $\Delta\hat{\theta}$  and  $\Delta\theta$  are the post-fit and pre-fit uncertainties respectively. The post-fit and pre-fit impact of each nuisance parameter on  $\mu(tWZ)$  are shown with the solid and lined rectangles respectively. The empty and solid blue rectangles correspond to the pre-fit and post-fit impacts on  $\mu(tWZ)$  respectively. These impacts are shown on the upper axis ( $\Delta\mu$ ). On the lower axis, the nuisance parameter pull,  $\frac{\hat{\theta} - \theta_0}{\Delta\theta}$ , is shown ( $\theta_0$  is the nominal pre-fit value of the nuisance parameter). The nuisance parameter pull is indicated by the black points, with their relative post-fit errors ( $\frac{\Delta\hat{\theta}}{\Delta\theta}$ ) shown by the black horizontal error bars.

1248 The most important systematics are the cross sections of  $t\bar{t}Z$  and  $ZZ$ , and shape modelling on  $t\bar{t}Z$  ( $t\bar{t}Z$  triangular  
 1249 shape) and  $tWZ$  ( $tWZ$ -DR2 and  $tWZ$  triangular shape). The cross section of  $ZZ$  is significantly shifted down  
 1250 in the fit from its nominal value. The  $t\bar{t}Z$  cross section,  $tWZ$ -DR2 and  $t\bar{t}Z$  triangular shape nuisance parameters  
 1251 are similarly shifted down in the fit from their nominal values, but to a much lesser degree than the cross section  
 1252 of  $ZZ$ . These pulls are all within  $1\sigma$  uncertainty and are thus relatively small. It is expected that the modelling  
 1253 uncertainties (shape and normalisations) of the most dominant backgrounds (e.g.  $t\bar{t}Z$ ,  $ZZ$ ) have relatively large  
 1254 impacts on  $\mu(tWZ)$ , since the uncertainty of the analysis is dominated by statistical uncertainty.

#### 1255 4.11.2 Trilepton and Tetralepton Channels

1256 In the section, an expected upper limit and an expected significance are set on the cross section of  $tWZ$  from the  
 1257 combined fit across all regions of  $tWZ$  in the tetralepton and trilepton channels.

Nuisance Parameter	Channel Affected	
	trilepton	tetralepton
$\sigma(t\bar{t}H)$	✓	✓
$\sigma(t\bar{t}Z)$	✓	✓
$\sigma(WZ)$	✓	✓
$\sigma(tZq)$	✓	✓
$\sigma(ZZ)$	✓	✓
$\sigma(\text{other(trilepton)})$	✓	✗
$\sigma(\text{other(tetralepton)})$	✗	✓
$\sigma(t\bar{t}Z)_{\text{fakes}}$	✗	✓
$\sigma(t\bar{t})_{\text{fakes}}$	✓	✗
$\sigma(Z + \text{jets})_{\text{fakes}}$	✓	✗
Luminosity	✓	✓
$jvt$	✓	✓
pileup	✓	✓
DL1r SF (b jets)	✓	✓
DL1r SF (light jets)	✓	✓
$\sigma(tWZ - DR2)$	✗	✓
lepton SF	✓	✓
$t\bar{t}Z$ triangular shape	✓	✓
$t\bar{t}Z$ linear shape	✓	✓
$WZ + b$ triangular shape	✓	✗
$WZ + b$ linear shape	✓	✗
$WZ + c$ triangular shape	✓	✗
$WZ + c$ linear shape	✓	✗

Table 4.11: A summary of the nuisance parameters used in the combined fit is shown. The channels which are affected by each nuisance parameter are indicated with a ✓ (is affected) or a ✗ (is not affected).

1259 The trilepton analysis follows a similar analysis strategy to that of the tetralepton analysis. It includes an  
 1260 event-level BDT which aims to discriminate between the  $tWZ$  and all background as well as an object-level  
 1261 BDT which aims to identify hadronically decaying  $W$  bosons to discriminate between  $tWZ$  and the large  $WZ$   
 1262 background. One  $tWZ$  SR is defined and five CRs are defined.  $WZ$  and  $t\bar{t}Z$  CRs are defined to constrain the  
 1263 dominant  $WZ$  and  $t\bar{t}Z$  backgrounds. Three CRs which require that one of the three selected leptons are loose, are  
 1264 defined for  $WZ$ ,  $t\bar{t}Z$  and  $tWZ$  in order to constraint the fake lepton component (using the MC template method -  
 1265 similar to the method used in Section 4.6 to estimate the fake lepton component).

1266  
 1267 The expected upper limit of  $tWZ$  in the trilepton channel is measured as,

$$\mu_{up}^{exp} = 2.65^{+3.67}_{-1.91} \quad (4.18)$$

1268 The expected significance of  $tWZ$  in the trilepton channel is measured as,

$$Z_\mu^{exp} = 0.75\sigma \quad (4.19)$$

1269 The best-fit value of the signal strength,  $\mu(tWZ) = \frac{\sigma(tWZ)}{\sigma(tWZ)_{SM}}$ , from the likelihood fit is measured as,

$$\mu(tWZ) = 1.16^{+1.33}_{-1.30} \quad (4.20)$$

1270 The expected upper limit is in agreement with the extracted best-fit value on the signal strength, therefore no  
 1271 deviations from the SM cross section of  $tWZ$  is observed.

1272  
 1273 In Table 4.11, the nuisance parameters used in the fit, including which channel's regions are affected by each, are  
 1274 shown.

1275 The expected upper limit of  $tWZ$  across both channels is measured as,

$$\mu_{up}^{exp} = 1.43^{+2.04}_{-1.03} \quad (4.21)$$

1276 The expected significance of  $tWZ$  across both channels is measured as,

$$Z_\mu^{exp} = 1.61\sigma \quad (4.22)$$

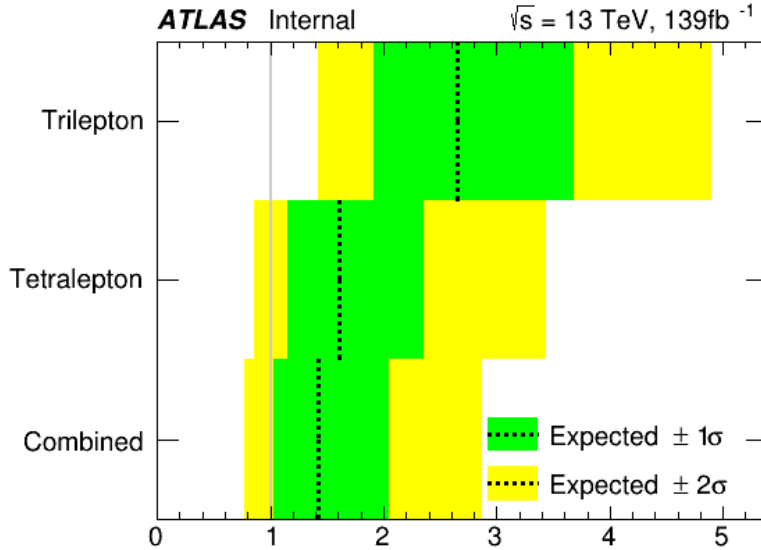


Figure 4.52: The expected upper limits of the trilepton channel, tetralepton channel and both channels combine are shown. The y-axis shows the channels in which the fitting procedure was performed. The expected limits are represented by the vertical dotted line. One- and two-  $\sigma$  uncertainty bands are shown in green and yellow respectively. The vertical grey line indicates when  $\mu(tWZ) = 1$ .

<sup>1277</sup> The best-fit value of the signal strength,  $\mu(tWZ) = \frac{\sigma(tWZ)}{\sigma(tWZ)_{SM}}$ , from the likelihood fit is measured as,

$$\mu(tWZ) = 1.80^{+0.70}_{-0.65} \quad (4.23)$$

<sup>1278</sup> In Figure 4.52, the expected upper limits of the trilepton channel, tetralepton channel and both channels combined are shown.

<sup>1280</sup> It can be seen that the sensitivity of  $tWZ$  is mostly driven by the tetralepton analysis, with the trilepton analysis attributing a small decrease in the expected upper limit of the combined analysis, and its associated uncertainty.

<sup>1282</sup> In Figure 4.53, the best-fit values of  $\mu(tWZ)$  from the fit for the trilepton channel, tetralepton channel and both channels combined are shown.

<sup>1285</sup> It can be seen from Figures 4.52 and 4.53 that the best fit value for the signal strength on  $tWZ$ ,  $\mu(tWZ)$ , and the expected limits for the tri- and tetralepton channels are consistent with one-another (their uncertainties overlap). Therefore it is appropriate to combine these two analyses.

<sup>1288</sup> In Figure 4.54, a ranking plot showing the impact of the systematic uncertainties on the POI,  $\mu(tWZ)$ , in the combined fit across both the tri- and tetralepton channels is shown.

<sup>1291</sup> Some nuisance parameters are pulled down from their nominal pre-fit values, however these are all within  $1\sigma$  uncertainty and are thus relatively small. It is expected that the modelling uncertainties (shape and normalisations) of the most dominant backgrounds (e.g.  $t\bar{t}Z$ ,  $ZZ$ ,  $WZ$ ) have relatively large impacts on  $\mu(tWZ)$ , since the uncertainty of the analysis is dominated by statistical uncertainty.

<sup>1295</sup> The most important systematics are the cross sections of  $t\bar{t}Z$ ,  $ZZ$  and  $WZ + b$ , and shape modelling on  $t\bar{t}Z$  ( $t\bar{t}Z$  triangular shape). The aforementioned nuisance parameters are significantly shifted down in the fit from its nominal value. The less important systematics are pulled in the fit from their nominal values, but to a much lesser degree than the cross section of those mentioned above. It is expected that the modelling uncertainties (shape and normalisations) of the most dominant backgrounds (e.g.  $t\bar{t}Z$ ,  $ZZ$  and  $WZ + b$ ) have relatively large impacts on  $\mu(tWZ)$ , since the uncertainty of the analysis is dominated by statistical uncertainty.

#### <sup>1302</sup> 4.11.2.1 Projection to Higher Luminosity

<sup>1303</sup> In this section we apply a fully blinded fit to the ASIMOV dataset for integrated luminosities larger than the  $139\text{fb}^{-1}$  currently available from the ATLAS Full Run 2 dataset. This study gives us insight into the sensitivity of  $tWZ$

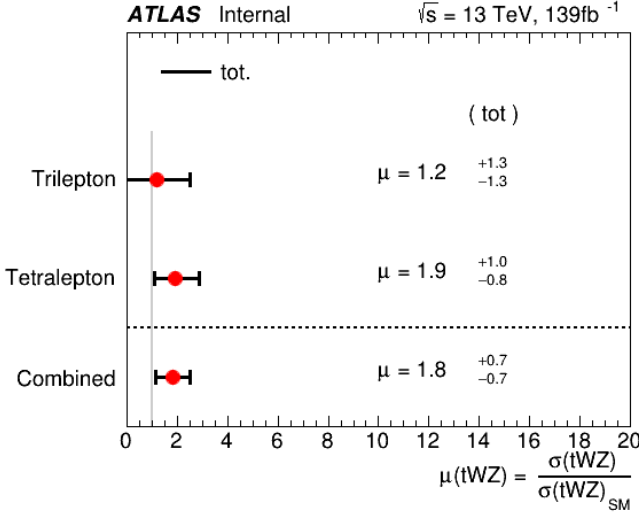


Figure 4.53: The best-fit values of  $\mu(tWZ)$  from the fit for the trilepton channel, tetralepton channel and both channels combined are shown. The y-axis shows the channels in which the fitting procedure was performed. The signal strength  $\mu(tWZ)$  is shown on the x-axis. The nominal signal strengths are represented by the red dots. The total uncertainty associated with the best-fit  $\mu(tWZ)$  value is shown by the black error bars.

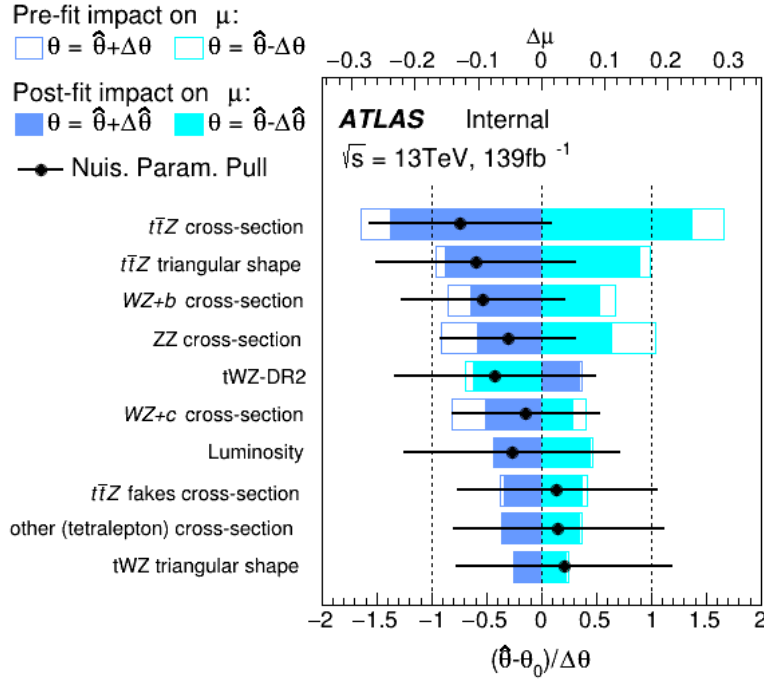


Figure 4.54: A ranking plot showing the impact of the systematic uncertainties (top 10) on the POI,  $\mu(tWZ)$ , in the combined fit across both the tri- and tetralepton channels is shown.  $\hat{\theta}$  is the best-fit value of the nuisance parameter.  $\Delta\hat{\theta}$  and  $\Delta\theta$  are the post-fit and pre-fit uncertainties respectively. The post-fit and pre-fit impact of each nuisance parameter on  $\mu(tWZ)$  are shown with the solid and lined rectangles respectively. The empty and solid blue rectangles correspond to the pre-fit and post-fit impacts on  $\mu(tWZ)$  respectively. These impacts are shown on the upper axis ( $\Delta\mu$ ). On the lower axis, the nuisance parameter pull,  $\frac{\hat{\theta} - \theta_0}{\Delta\theta}$ , is shown ( $\theta_0$  is the nominal pre-fit value of the nuisance parameter). The nuisance parameter pull is indicated by the black points, with their relative post-fit errors ( $\frac{\Delta\hat{\theta}}{\Delta\theta}$ ) shown by the black horizontal error bars.

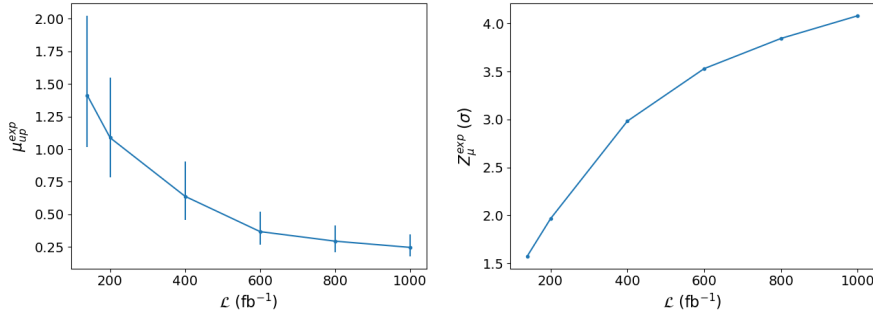


Figure 4.55: The expected upper limit (left) and significance (right) for combined fully blinded fits to the ASIMOV dataset across both the tri- and tetralepton channels for a range integrated luminosities are shown. **Left:** The integrated luminosity,  $\mathcal{L}$ , is shown on the x-axis. The expected upper limit,  $\mu_{up}^{exp}$ , is shown on the y-axis. The vertical lines represent the total uncertainty ( $\pm 1\sigma$ ) on the expected upper limit. **Right:** The integrated luminosity,  $\mathcal{L}$ , is shown on the x-axis. The expected significance,  $Z_\mu^{exp}$ , is shown on the y-axis. The vertical lines represent the total uncertainty ( $\pm 1\sigma$ ) on the expected significance.

1305 which we could expect if we were to replicate the current analysis, given more data. Given the upgrades planned  
 1306 for the LHC and the ATLAS detector, we will soon expect an large increase in available  $pp$  collision data (reaching  
 1307  $\mathcal{L} = 3000 \text{fb}^{-1}$  [32]). This study therefore gives us an idea of the sensitivity of  $tWZ$  which we can expect in the future.

1308 In Figure 4.55, the expected upper limit and significance for combined fully blinded fits to the ASIMOV dataset  
 1309 across both the tri- and tetralepton channels for a range integrated luminosities are shown.

1310 As we increase the total integrated luminosity, the sensitivity of  $tWZ$  increases. The increase in sensitivity is shown  
 1311 by the decrease of the expected upper limit and the increase of the expected significance with increasing integrated  
 1312 luminosity. It can be noted that a  $3\sigma$  expected significance is achieved at  $\mathcal{L} \sim 400 \text{ fb}^{-1}$ , indicating evidence for  
 1313 observation of  $tWZ$ . The  $5\sigma$  significance 'discovery' standard is above our  $1000 \text{fb}^{-1}$  luminosity range of study.  
 1314 Furthermore, these plots show that the sensitivity of  $tWZ$  is hindered by the low amount of events we observe,  
 1315 rather than the systematic effects. This is evident since increasing the luminosity, therefore increasing the number  
 1316 of events we see in the detector, directly causes a steady in increase in sensitivity.

1318

# Chapter 5

1319

## Conclusion

1320 The search for  $tWZ$  production using  $139 \text{ fb}^{-1}$  of  $pp$  collision data at a centre-of-mass energy of  $\sqrt{s} = 13 \text{ TeV}$ ,  
 1321 recorded by the ATLAS experiment at CERN, has been presented. This thesis targeted the tetralepton final state  
 1322 channel. To further increase the sensitivity of  $tWZ$ , a combined analysis was done across the tetralepton and  
 1323 trilepton (studied in an independent analysis by Benjamin Warren (UCT) [81]) channels.

1324 Two SRs and Three CRs were defined. Two SRs, instead of one, were defined in order to suppress and constrain  
 1325 the  $ZZ$  background. The definition of the  $tWZ$  OF SR and the  $tWZ$  SF SR take advantage of the OSSF lepton  
 1326 pairs which originate from the decay of a  $Z$  boson, by requiring that non- $Z$  leptons in the event have the opposite  
 1327 and same flavours, for the  $tWZ$  OF SR and  $tWZ$  SF SR respectively. The resulting SRs successfully separate the  
 1328  $ZZ$  background, with the  $tWZ$  OF SR containing around 6% of the total  $ZZ$  background yield across both regions  
 1329 (implying that the remaining  $\sim 94\%$  is contained in the  $tWZ$  SF SR). The dominant background processes,  $t\bar{t}Z$   
 1330 and  $ZZ$  were constrained by the definition of  $t\bar{t}Z$  and  $ZZ$  CRs, respectively. The dominant source of fake leptons,  
 1331 originating from the  $t\bar{t}Z$  background, was constrained by the  $(tWZ)_{fake}$  CR, using the MC template method.

1333 Two BDTs were implemented: an object-level BDT which aims to classify between  $\ell b$  systems coming from top  
 1334 quarks and an event-level BDT which aims to discriminate between  $tWZ$  and our major backgrounds,  $t\bar{t}Z$  and  
 1335  $ZZ$ . The output from the object-level BDT was converted to an event-level variable to be used as input to  
 1336 the event-level BDT. A kinematic reconstruction algorithm,  $2\nu\text{SM}$ , was used to reconstruct top quarks in order  
 1337 to discriminate between  $tWZ$  and  $t\bar{t}Z$ . The output from this algorithm was used as an input variable to the  
 1338 event-level BDT. The trained BDT was shown to discriminate well between signal and background events.

1340 Using a modified ASIMOV dataset in the SRs and real data in the CRs, a blinded maximum-likelihood fit was  
 1341 performed across all regions in the tetralepton channel. The best-fit value of the signal strength in the tetralepton  
 1342 channel was,

$$\mu(tWZ) = 1.91^{+0.95}_{-0.82} \quad (5.1)$$

1344 with an expected significance of  $1.44\sigma$ . The expected upper limit on the signal strength of  $tWZ$  in the tetralepton  
 1345 channel was,

$$\mu_{up}^{exp} = 1.61^{+2.35}_{-1.16} \quad (5.2)$$

1346 Furthermore, a blinded maximum-likelihood fit was performed across all regions across the trilepton and tetralepton  
 1347 channels. The best-fit value of the signal strength across both the trilepton and tetralepton channels were,

$$\mu(tWZ) = 1.80^{+0.70}_{-0.65} \quad (5.3)$$

1348 with an expected significance of  $1.61\sigma$ . The expected upper limit on the signal strength of  $tWZ$  across both the  
 1349 trilepton and tetralepton channels were,

$$\mu_{up}^{exp} = 1.43^{+2.04}_{-1.03} \quad (5.4)$$

1350 Although this result does not satisfy the  $3\sigma$  evidence nor the  $5\sigma$  discovery standards, this is the tightest ever  
 1351 constraint on the  $tWZ$  process. The results in this analysis are heavily statistically limited, it is therefore expected  
 1352 that future analyses of this process, using larger datasets (such as that from the HL-LHC), would significantly  
 1353 improve the results.

1354

# Bibliography

- [1] M. Aaboud et al. “Electron reconstruction and identification in the ATLAS experiment using the 2015 and 2016 LHC proton–proton collision data at  $\sqrt{s} = 13$  TeV”. In: *The European Physical Journal C* 79.8 (Aug. 2019). ISSN: 1434-6052. DOI: 10.1140/epjc/s10052-019-7140-6. URL: <http://dx.doi.org/10.1140/epjc/s10052-019-7140-6>.
- [2] M. Aaboud et al. “Measurement of the  $t\bar{t}Z$  and  $t\bar{t}W$  cross sections in proton-proton collisions at  $\sqrt{s} = 13$  TeV with the ATLAS detector”. In: *Phys. Rev. D* 99 (7 Apr. 2019), p. 072009. DOI: 10.1103/PhysRevD.99.072009. URL: <https://link.aps.org/doi/10.1103/PhysRevD.99.072009>.
- [3] Aaboud, M. and Aad, G. and Abbott, B. and Abbott, D. C. and Abdinov, O. and Abed Abud, A. and Abhayasinghe, D. K. and Abidi, S. H. and AbouZeid, O. S. and et al. “Measurement of ZZ production in the  $\ell\ell\nu\nu$  final state with the ATLAS detector in pp collisions at  $s \sqrt{s} = 13$  TeV”. In: *Journal of High Energy Physics* 2019.10 (Oct. 2019). ISSN: 1029-8479. DOI: {10.1007/jhep10(2019)127}. URL: %7B[http://dx.doi.org/10.1007/JHEP10\(2019\)127%7D](http://dx.doi.org/10.1007/JHEP10(2019)127%7D).
- [4] G. Aad et al. “Measurement of the  $t\bar{t}$  production cross-section in the lepton+jets channel at  $s=13$  TeV with the ATLAS experiment”. In: *Physics Letters B* 810 (2020), p. 135797. ISSN: 0370-2693. DOI: <https://doi.org/10.1016/j.physletb.2020.135797>. URL: <https://www.sciencedirect.com/science/article/pii/S0370269320306006>.
- [5] G. Aad et al. “Muon reconstruction performance of the ATLAS detector in proton–proton collision data at  $\sqrt{s} = 13$  TeV”. In: *The European Physical Journal C* 76.5 (May 2016). ISSN: 1434-6052. DOI: 10.1140/epjc/s10052-016-4120-y. URL: <http://dx.doi.org/10.1140/epjc/s10052-016-4120-y>.
- [6] Georges Aad et al. “Topological cell clustering in the ATLAS calorimeters and its performance in LHC Run 1. Topological cell clustering in the ATLAS calorimeters and its performance in LHC Run 1”. In: *Eur. Phys. J. C* 77 (Mar. 2016), 490. 87 p. DOI: 10.1140/epjc/s10052-017-5004-5. arXiv: 1603.02934. URL: <https://cds.cern.ch/record/2138166>.
- [7] Shunichi Akatsuka and Shion Chen. *Isolation WPs summary: PLV + LowPtPLV*. Oct. 2019. URL: <https://indico.cern.ch/event/854783/contributions/3595486/attachments/1929380/3195230/PLV-Summary.pdf>.
- [8] Guido Altarelli. *The Higgs and the Excessive Success of the Standard Model*. 2014. arXiv: 1407.2122 [hep-ph].
- [9] Aaron Armbruster. *Asymptotic Formulae*. Feb. 2013. URL: [https://indico.cern.ch/event/233551/contributions/493678/attachments/389871/542293/asymptotics\\_armbruster.pdf](https://indico.cern.ch/event/233551/contributions/493678/attachments/389871/542293/asymptotics_armbruster.pdf).
- [10] Pierre Astier et al. “Kalman filter track fits and track breakpoint analysis”. In: *Nuclear Instruments and Methods in Physics Research Section A: Accelerators, Spectrometers, Detectors and Associated Equipment* 450.1 (2000), pp. 138–154. ISSN: 0168-9002. DOI: [https://doi.org/10.1016/S0168-9002\(00\)00154-6](https://doi.org/10.1016/S0168-9002(00)00154-6). URL: <https://www.sciencedirect.com/science/article/pii/S0168900200001546>.
- [11] ATLAS Collaboration. “ATLAS  $b$ -jet identification performance and efficiency measurement with  $t\bar{t}$  events in  $pp$  collisions at  $\sqrt{s} = 13$  TeV”. In: *Eur. Phys. J. C* 79 (2019), p. 970. DOI: 10.1140/epjc/s10052-019-7450-8. arXiv: 1907.05120 [hep-ex].
- [12] ATLAS Collaboration. *Calibration of light-flavour  $b$ -jet mistagging rates using ATLAS proton–proton collision data at  $\sqrt{s} = 13$  TeV*. ATLAS-CONF-2018-006. 2018. URL: <https://cds.cern.ch/record/2314418>.
- [13] ATLAS Collaboration. “Electron and photon performance measurements with the ATLAS detector using the 2015–2017 LHC proton–proton collision data”. In: *JINST* 14 (2019), P12006. DOI: 10.1088/1748-0221/14/12/P12006. arXiv: 1908.00005 [hep-ex].

- [14] ATLAS Collaboration. “Identification and rejection of pile-up jets at high pseudorapidity with the ATLAS detector”. In: *Eur. Phys. J. C* 77 (2017), p. 580. DOI: 10.1140/epjc/s10052-017-5081-5. arXiv: 1705.02211 [hep-ex].
- [15] ATLAS Collaboration. *Measurement of b-tagging efficiency of c-jets in  $t\bar{t}$  events using a likelihood approach with the ATLAS detector*. ATLAS-CONF-2018-001. 2018. URL: <https://cds.cern.ch/record/2306649>.
- [16] ATLAS Collaboration. “Measurements of b-jet tagging efficiency with the ATLAS detector using  $t\bar{t}$  events at  $\sqrt{s} = 13\text{TeV}$ ”. In: *JHEP* 08 (2018), p. 089. DOI: 10.1007/JHEP08(2018)089. arXiv: 1805.01845 [hep-ex].
- [17] ATLAS Collaboration. “Muon reconstruction and identification efficiency in ATLAS using the full Run 2  $pp$  collision data set at  $\sqrt{s} = 13\text{TeV}$ ”. In: (2020). arXiv: 2012.00578 [hep-ex].
- [18] Manuel Guth on behalf of the ATLAS collaboration. *Deep-Neural-Network-based b-Tagging as Basis for Improvements in Top Analyses*. URL: <https://cds.cern.ch/record/2693088/files/ATL-PHYS-SLIDE-2019-751.pdf>.
- [19] ATLAS Internal. *Electron Efficiencies for Analyses*. 2021. URL: <https://twiki.cern.ch/twiki/bin/viewauth/AtlasProtected/ElectronEfficienciesForAnalysis>.
- [20] ATLAS Internal. *Electron Efficiency Correlation Model*. 2021. URL: <https://twiki.cern.ch/twiki/bin/view/AtlasProtected/ElectronEfficiencyCorrelationModel>.
- [21] ATLAS Internal. *Jet Vertex Tagger for Run 2 in reco and analysis*. 2021. URL: <https://twiki.cern.ch/twiki/bin/view/AtlasProtected/JetVertexTaggerTool>.
- [22] ATLAS Internal. *Muon Efficiencies for Analyses*. 2021. URL: <https://twiki.cern.ch/twiki/bin/view/AtlasProtected/MuonEfficienciesForAnalysis>.
- [23] G. Avoni et al. “The new LUCID-2 detector for luminosity measurement and monitoring in ATLAS”. In: *JINST* 13.07 (2018), P07017. DOI: 10.1088/1748-0221/13/07/P07017.
- [24] Richard D. Ball et al. “Parton distributions for the LHC run II”. In: *Journal of High Energy Physics* 2015.4 (Apr. 2015). ISSN: 1029-8479. DOI: 10.1007/jhep04(2015)040. URL: [http://dx.doi.org/10.1007/JHEP04\(2015\)040](http://dx.doi.org/10.1007/JHEP04(2015)040).
- [25] Olga Bessidskaia Bylund. *Measurement of ttZ and ttW production at ATLAS in 13 TeV data, using trilepton and same charge dimuon final states*. Tech. rep. Geneva: CERN, Aug. 2016. DOI: 10.22323/1.276.0237. URL: <http://cds.cern.ch/record/2211022>.
- [26] Ilaria Brivio and Michael Trott. “The standard model as an effective field theory”. In: *Physics Reports* 793 (Feb. 2019), pp. 1–98. ISSN: 0370-1573. DOI: 10.1016/j.physrep.2018.11.002. URL: <http://dx.doi.org/10.1016/j.physrep.2018.11.002>.
- [27] Oliver Sim Brüning et al. *LHC Design Report*. CERN Yellow Reports: Monographs. Geneva: CERN, 2004. DOI: 10.5170/CERN-2004-003-V-1. URL: <https://cds.cern.ch/record/782076>.
- [28] Matteo Cacciari, Gavin P. Salam, and Gregory Soyez. “The anti- $k_t$  jet clustering algorithm”. In: *JHEP* 04 (2008), p. 063. DOI: 10.1088/1126-6708/2008/04/063. arXiv: 0802.1189 [hep-ph].
- [29] Thomas Calvet. *Automatic binning implementation in TTHTfitter - Htop(bb)*. URL: [https://indico.cern.ch/event/455289/contributions/1953694/attachments/1209081/1762963/Calvet\\_binning\\_Htop-160108.pdf](https://indico.cern.ch/event/455289/contributions/1953694/attachments/1209081/1762963/Calvet_binning_Htop-160108.pdf).
- [30] Anadi Canepa. “Searches for supersymmetry at the Large Hadron Collider”. In: *Reviews in Physics* 4 (2019), p. 100033. ISSN: 2405-4283. DOI: <https://doi.org/10.1016/j.revip.2019.100033>. URL: <https://www.sciencedirect.com/science/article/pii/S2405428318300091>.
- [31] CERN Twiki - TOP WG Summary Plots. URL: <https://twiki.cern.ch/twiki/bin/view/LHCPhysics/LHCTopWGSummaryPlots>.
- [32] CERN Yellow Reports: Monographs. *CERN Yellow Reports: Monographs, Vol. 10 (2020): High-Luminosity Large Hadron Collider (HL-LHC): Technical design report*. en. 2020. DOI: 10.23731/CYRM-2020-0010. URL: <https://e-publishing.cern.ch/index.php/CYRM/issue/view/127>.
- [33] Masud Chaichian, Ricardo Gonzalez Felipe, and Katri Huitu. “On quadratic divergences and the Higgs mass”. In: *Physics Letters B* 363.1-2 (Nov. 1995), pp. 101–105. ISSN: 0370-2693. DOI: 10.1016/0370-2693(95)01191-r. URL: [http://dx.doi.org/10.1016/0370-2693\(95\)01191-R](http://dx.doi.org/10.1016/0370-2693(95)01191-R).

- [34] Shion Chen. *Track isolation variable for the PFlow WPs*. Oct. 2019. URL: [https://indico.cern.ch/event/854783/contributions/3595529/attachments/1926980/3190772/IFF\\_20191003\\_PflowWPs.pdf](https://indico.cern.ch/event/854783/contributions/3595529/attachments/1926980/3190772/IFF_20191003_PflowWPs.pdf).
- [35] KyungEon Choi. “Tracking and Vertexing with the ATLAS Inner Detector in the LHC Run-2”. In: *Springer Proc. Phys.* 213 (2018). Ed. by Zhen-An Liu, pp. 400–403. DOI: 10.1007/978-981-13-1316-5\_75.
- [36] CMS Collaboration. *Measurements of  $pp \rightarrow ZZ$  production cross sections and constraints on anomalous triple gauge couplings at  $\sqrt{s} = 13$  TeV*. 2020. arXiv: {2009.01186} (hep-ex).
- [37] The ATLAS Collaboration et al. “The ATLAS Experiment at the CERN Large Hadron Collider”. In: *Journal of Instrumentation* 3.08 (Aug. 2008), S08003–S08003. DOI: 10.1088/1748-0221/3/08/s08003. URL: <https://doi.org/10.1088/1748-0221/3/08/s08003>.
- [38] I. Connolly. “Performance and calibration of b-tagging with the ATLAS experiment at LHC Run-2”. In: 2017.
- [39] Glen Cowan et al. “Asymptotic formulae for likelihood-based tests of new physics”. In: *The European Physical Journal C* 71.2 (Feb. 2011). ISSN: 1434-6052. DOI: 10.1140/epjc/s10052-011-1554-0. URL: <http://dx.doi.org/10.1140/epjc/s10052-011-1554-0>.
- [40] Federico Demartin et al. “tWH associated production at the LHC”. In: *Eur. Phys. J. C* 77.1 (2017), p. 34. DOI: 10.1140/epjc/s10052-017-4601-7. arXiv: 1607.05862 [hep-ph].
- [41] *Electron identification efficiency in data for electrons with  $E_T > 30\text{GeV}$* . URL: [https://atlas.web.cern.ch/Atlas/GROUPS/PHYSICS/PAPERS/EGAM-2018-01/fig\\_16.png](https://atlas.web.cern.ch/Atlas/GROUPS/PHYSICS/PAPERS/EGAM-2018-01/fig_16.png).
- [42] F. Englert and R. Brout. “Broken Symmetry and the Mass of Gauge Vector Mesons”. In: *Phys. Rev. Lett.* 13 (9 Aug. 1964), pp. 321–323. DOI: 10.1103/PhysRevLett.13.321. URL: <https://link.aps.org/doi/10.1103/PhysRevLett.13.321>.
- [43] *Errors in weighted histograms*. URL: <https://www.zeuthen.desy.de/~wischnew/amanda/discussion/wgterror/working.html>.
- [44] Lyndon Evans and Philip Bryant. “LHC Machine”. In: *Journal of Instrumentation* 3.08 (Aug. 2008), S08001–S08001. DOI: 10.1088/1748-0221/3/08/s08001. URL: <https://doi.org/10.1088/1748-0221/3/08/s08001>.
- [45] Guido Fantini et al. *The formalism of neutrino oscillations: an introduction*. 2020. arXiv: 1802.05781 [hep-ph].
- [46] Steve Farrell. *Overlap Removal Tools, FTAG/Hbb Workshop*. URL: [https://indico.cern.ch/event/631313/contributions/2683959/attachments/1518878/2373377/Farrell\\_ORTools\\_ftaghbb.pdf](https://indico.cern.ch/event/631313/contributions/2683959/attachments/1518878/2373377/Farrell_ORTools_ftaghbb.pdf).
- [47] *GoodRunListsForAnalysisRun2*. URL: <https://twiki.cern.ch/twiki/bin/viewauth/AtlasProtected/GoodRunListsForAnalysisRun2>.
- [48] Particle Data Group et al. “Review of Particle Physics”. In: *Progress of Theoretical and Experimental Physics* 2020.8 (Aug. 2020). 083C01. ISSN: 2050-3911. DOI: 10.1093/ptep/ptaa104. eprint: <https://academic.oup.com/ptep/article-pdf/2020/8/083C01/33653179/ptaa104.pdf>. URL: <https://doi.org/10.1093/ptep/ptaa104>.
- [49] Peter W. Higgs. “Broken Symmetries and the Masses of Gauge Bosons”. In: *Phys. Rev. Lett.* 13 (1964). Ed. by J. C. Taylor, pp. 508–509. DOI: 10.1103/PhysRevLett.13.508.
- [50] Peter W. Higgs. “Spontaneous Symmetry Breakdown without Massless Bosons”. In: *Phys. Rev.* 145 (1966), pp. 1156–1163. DOI: 10.1103/PhysRev.145.1156.
- [51] *IFFTruthClassifier GitLab Repository*. URL: <https://gitlab.cern.ch/ATLAS-IFF/IFFTruthClassifier/-/tree/master>.
- [52] *IFFTruthClassifier Lepton Categories*. URL: <https://gitlab.cern.ch/ATLAS-IFF/IFFTruthClassifier/-/tree/master#3-details-about-the-lepton-categories>.
- [53] N. Jarosik et al. “SEVEN-YEAR WILKINSON MICROWAVE ANISOTROPY PROBE (WMAP) OBSERVATIONS: SKY MAPS, SYSTEMATIC ERRORS, AND BASIC RESULTS”. In: *The Astrophysical Journal Supplement Series* 192.2 (Jan. 2011), p. 14. ISSN: 1538-4365. DOI: 10.1088/0067-0049/192/2/14. URL: <http://dx.doi.org/10.1088/0067-0049/192/2/14>.
- [54] F. Jegerlehner. “The hierarchy problem of the electroweak Standard Model revisited”. In: (May 2013).

- [55] V. Khachatryan et al. “Measurement of the ZZ production cross section and  $Z \rightarrow \ell^+\ell^-\ell^+\ell^-$  branching fraction in pp collisions at  $\sqrt{s} = 13\text{TeV}$ ”. In: *Physics Letters B* 763 (2016), pp. 280–303. ISSN: 0370-2693. DOI: <https://doi.org/10.1016/j.physletb.2016.10.054>. URL: <https://www.sciencedirect.com/science/article/pii/S0370269316306256>.
- [56] H. J. W. Kirsten. *Introduction to supersymmetry*. Singapore Hackensack, NJ: World Scientific, 2010. ISBN: 978-9814293426.
- [57] Fabio Maltoni, Luca Mantani, and Ken Mimasu. “Top-quark electroweak interactions at high energy”. In: *Journal of High Energy Physics* 2019.10 (Oct. 2019). ISSN: 1029-8479. DOI: 10.1007/jhep10(2019)004. URL: [http://dx.doi.org/10.1007/JHEP10\(2019\)004](http://dx.doi.org/10.1007/JHEP10(2019)004).
- [58] Luigi Marchese. *Lepton and photon reconstruction and identification performance in ATLAS and CMS*. Tech. rep. Geneva: CERN, Sept. 2019. DOI: 10.22323/1.350.0237. URL: <https://cds.cern.ch/record/2688452>.
- [59] Thomas McCarthy. *Macro developed to compare t/W/Z reconstruction performance (2ℓ, 3ℓ, 4ℓ)*. URL: [https://indico.cern.ch/event/986357/contributions/4172907/attachments/2169451/3666801/reco-performance\\_macro\\_20210112.pdf](https://indico.cern.ch/event/986357/contributions/4172907/attachments/2169451/3666801/reco-performance_macro_20210112.pdf).
- [60] Thomas McCarthy and Florian Fischer. *Exploiting full/partial  $t\bar{t}$  reconstruction for background suppression in 2ℓ*. URL: [https://indico.cern.ch/event/955360/contributions/4016465/attachments/2102418/3534816/top\\_reco\\_bkgd\\_suppression\\_2L\\_20200915.pdf](https://indico.cern.ch/event/955360/contributions/4016465/attachments/2102418/3534816/top_reco_bkgd_suppression_2L_20200915.pdf).
- [61] *MCTruthClassifier - ATLAS Twiki*. URL: <https://twiki.cern.ch/twiki/bin/view/AtlasProtected/MCTruthClassifier>.
- [62] F. Meloni. “Primary vertex reconstruction with the ATLAS detector”. In: *Journal of Instrumentation* 11.12 (Dec. 2016), pp. C12060–C12060. DOI: 10.1088/1748-0221/11/12/c12060. URL: <https://doi.org/10.1088/1748-0221/11/12/c12060>.
- [63] Ken Mimasu. *Top quark electroweak interactions*. 2021. arXiv: 2105.10261 [hep-ph].
- [64] Users MissMJ and Cush. *Standard model of elementary particles - Wikimedia Commons*. URL: [https://en.wikipedia.org/wiki/File:Standard\\_Model\\_of\\_Elementary\\_Particles.svg](https://en.wikipedia.org/wiki/File:Standard_Model_of_Elementary_Particles.svg).
- [65] *Monte Carlo to Monte Carlo scale factors for flavour tagging efficiency calibration*. Tech. rep. ATL-PHYS-PUB-2020-009. Geneva: CERN, May 2020. URL: <https://cds.cern.ch/record/2718610>.
- [66] *MuonSelectionTool, ATLAS TWiki*. URL: <https://twiki.cern.ch/twiki/bin/view/Atlas/MuonSelectionTool>.
- [67] O Oncel. *Search for Single Top Quark Production in Association with a W and a Z Boson in the 3 Lepton Final State with the ATLAS Experiment at 13 TeV*. URL: <https://cds.cern.ch/record/2625170>.
- [68] *Option to force a shape withing an error band by hand - TRF documentation*. URL: [https://trexfitter-docs.web.cern.ch/trexfitter-docs/model\\_building/shape/](https://trexfitter-docs.web.cern.ch/trexfitter-docs/model_building/shape/).
- [69] *Pileup jet recommendations*. URL: <https://twiki.cern.ch/twiki/bin/view/AtlasProtected/PileupJetRecommendations>.
- [70] *Recommended isolation working points*. URL: <https://twiki.cern.ch/twiki/bin/view/AtlasProtected/RecommendedIsolationWPs>.
- [71] *scikit-learn Documentation - Gradient Boosting Classifier*. URL: <https://scikit-learn.org/stable/modules/generated/sklearn.ensemble.GradientBoostingClassifier.html>.
- [72] *Scikit-Learn GradientBoostingClassifier Documentation*. URL: <https://scikit-learn.org/stable/modules/generated/sklearn.ensemble.GradientBoostingClassifier.html>.
- [73] Pedro Ferreira da Silva. *Top quark production at the LHC*. 2016. arXiv: 1605.05343 [hep-ex].
- [74] Jory Sonneveld. *Searches for physics beyond the standard model at the LHC*. 2019. arXiv: 1905.06239 [hep-ex].
- [75] Mark Thomson. *Modern particle physics*. Cambridge, United Kingdom New York: Cambridge University Press, 2013. ISBN: 9781107034266.
- [76] *TopRecoObjTwikiModel*. URL: <https://twiki.cern.ch/twiki/bin/view/AtlasProtected/TopRecoObjTwikiModel>.
- [77] *Total Integrated Luminosity and Data Quality in 2015-2018 - LuminosityPublicResultsRun2*. URL: <https://twiki.cern.ch/twiki/bin/view/AtlasPublic/LuminosityPublicResultsRun2>.

- 1544 [78] Daniel R. Tovey. “Transformation properties of the transverse mass under transverse Lorentz boosts at hadron  
1545 colliders”. In: *The European Physical Journal C* 79.4 (Apr. 2019). ISSN: 1434-6052. DOI: 10.1140/epjc/s10052-019-6813-5. URL: <http://dx.doi.org/10.1140/epjc/s10052-019-6813-5>.
- 1547 [79] *TRExFitter*. URL: <https://twiki.cern.ch/twiki/bin/viewauth/AtlasProtected/TtHFitter>.
- 1548 [80] *TRExFitter: Mixed data and MC fit*. URL: <https://trexfitter-docs.web.cern.ch/trexfitter-docs/AdvancedTutorial2020/Mixed/>.
- 1550 [81] Benjamin Warren. “A search for tWZ production in the trilepton channel using Run 2 data from the ATLAS  
1551 experiment.” In: (2021).
- 1552 [82] Kenneth G. Wilson. “Confinement of quarks”. In: *Phys. Rev. D* 10 (8 Oct. 1974), pp. 2445–2459. DOI: 10.  
1553 1103/PhysRevD.10.2445. URL: <https://link.aps.org/doi/10.1103/PhysRevD.10.2445>.